

# Durham E-Theses

---

## *Esr and relaxation studies in doped calcium tungstate and magnesium oxide*

Ammar, El.Sayed A. E.

### How to cite:

---

Ammar, El.Sayed A. E. (1976) *Esr and relaxation studies in doped calcium tungstate and magnesium oxide*, Durham theses, Durham University. Available at Durham E-Theses Online:  
<http://etheses.dur.ac.uk/8163/>

### Use policy

---

The full-text may be used and/or reproduced, and given to third parties in any format or medium, without prior permission or charge, for personal research or study, educational, or not-for-profit purposes provided that:

- a full bibliographic reference is made to the original source
- a [link](#) is made to the metadata record in Durham E-Theses
- the full-text is not changed in any way

The full-text must not be sold in any format or medium without the formal permission of the copyright holders.

Please consult the [full Durham E-Theses policy](#) for further details.

ESR AND RELAXATION STUDIES  
IN DOPED CALCIUM TUNGSTATE  
AND MAGNESIUM OXIDE

by

EL.SAYED A. E. AMMAR  
(B.Sc., M.Sc., Alexandria)

Graduate Society

The copyright of this thesis rests with the author.  
No quotation from it should be published without  
his prior written consent and information derived  
from it should be acknowledged.

A thesis submitted to the University of Durham

in candidature for the degree of

Doctor of Philosophy

September 1976



*To*

*My Father*

*and*

*My Wife*

# ABSTRACT

As a precursor to the ESR and relaxation studies, measurements of the dielectric constants and loss for pure single crystals of calcium tungstate have been made at 1 MHz and room temperature giving values of  $\epsilon'_a = 11.3 \pm 0.4$ ,  $\epsilon'_c = 9.1 \pm 0.4$  and  $\tan\delta \approx 5 \times 10^{-3}$  which agree closely with Brower and Fang's. Our measurements were extended to frequencies up to 80 MHz and to samples doped with neodymium and gadolinium.

A detailed investigation has been made of the splitting of the ESR transitions in low concentration  $\text{Gd}^{3+}/\text{CaWO}_4$ , reported first by Buckley in 1973; this has led to the proposition of an ordered oxygen vacancy model giving rise to two slightly different Gd environments in both of which Gd substitutes for Ca at calcium sites. Sources for anomalies in the ESR spectra of rare earth ions in scheelite are briefly discussed.

Spin-lattice relaxation measurements for  $\text{Gd}^{3+}/\text{CaWO}_4$  were carried out at 37.5 GHz and in the temperature range from 4.2 K to 30 K. The relaxation in the 'direct' region agrees with preliminary measurements reported by Thorp et al, 1974, i.e.  $T_1 = 5.8$  msec at 4.2 K. The change from direct to Raman behaviour occurs near 8 K, and between 8 K and 30 K  $T_1$  follows a  $T_1 \propto T^{-3}$  law. This behaviour in the higher temperature range is explained by the assumption of crystal imperfections.

Measurements of spin-lattice relaxation were also made for  $\text{Fe}^{3+}/\text{MgO}$  in the same temperature range; here a  $T^{-4.6}$  variation was found in the Raman region and the transition temperature

between the direct and Raman processes was about 20 K. The data provided another example of an S-state ion behaving in the manner predicted by the present theories of relaxation.

In the last chapter an account is given of the combined use of ESR and TEM (Transmission Electron Microscopy) techniques, in an investigation of the role of impurities (mainly iron) in the growth of cavities in neutron-irradiated magnesium oxide crystals.

ACKNOWLEDGEMENTS

I wish to express my thanks to many people to whom I owe a debt of gratitude. Special mention must be made of the following:

The University of Alexandria, Egypt, for the award of a research scholarship to study for the degree of Ph.D. in the United Kingdom.

My supervisor, Dr. J. S. Thorp, for his unfailing guidance, suggestions and helpful discussions.

Professor D. A. Wright for the use of the research facilities in the Department, and to the technical staff, headed by Mr. Frank Spence, for their assistance. In particular I would like to thank Mr. Ron Waite, Mr. Colin Savage and Mr. Trevor Harcourt for their help.

Dr. G. Brown and Dr. G. J. Russell for their fruitful collaboration and helpful discussions.

My colleagues in the Department, especially Mr. William Hutton and Miss Linda Grange for their useful discussions and co-operation.

Mrs. J. Henderson for typing this thesis and  
Mrs. E. Johnston for the tracing of the drawings.

E. A. E. *Ammar*

# CONTENTS

	Page
Abstract	i
Acknowledgements	iii
Contents	iv
 CHAPTER 1: INTRODUCTION	
1.1 The aim of the work	1
1.2 Paramagnetic relaxation	5
1.3 The measurement of relaxation time	7
1.3.1 The pulse saturation method	8
1.3.2 Relaxation rate equations	9
1.4 Experimental techniques	11
1.4.1 Measurement of spin-lattice relaxation time $T_1$ .	14
 CHAPTER 2: THE DIELECTRIC CONSTANTS OF $\text{CaWO}_4$ , $\text{Nd/CaWO}_4$ AND $\text{Gd/CaWO}_4$	
2.1 Introduction	16
2.2 Experimental	16
2.3 Derivation of $\epsilon'$ and $\tan \delta$	18
2.4 Results	20
2.5 Discussion	21
 CHAPTER 3: SITE OCCUPATION BY GADOLINIUM IN CALCIUM TUNGSTATE	
3.1 The crystal structure	23
3.2 Crystal growth	24
3.3 The energy levels of $\text{Gd}^{3+}$ in $\text{CaWO}_4$	24
3.4 The spin-Hamiltonian	26
3.5 Experimental observations of ESR spectra of gadolinium in calcium tungstate	28
3.6 Comparison with the previous ESR data	30
3.6.1 Anomalous transitions of trivalent rare earth ions in scheelites	30
3.7 Interpretation of present results	33
3.7.1 Heat treatments of $\text{Gd/CaWO}_4$ samples in an oxygen ambient and their interpretation	34

CHAPTER 4:	SPIN-LATTICE RELAXATION IN GADOLINIUM-DOPED CALCIUM TUNGSTATE	
4.1	Theories of spin-lattice relaxation	37
4.2	Relaxation processes and their temperature dependence	40
4.2.1	The direct (or one phonon) process	40
4.2.2	The two-phonon Raman process	42
4.2.3	The resonant two-phonon relaxation, or Orbach process	42
4.2.4	Multiple ground state process	43
4.2.5	Modifications due to lattice imperfections	44
4.3	Experimental Results	48
4.3.1	$T_1$ -temperature dependence measurements	50
4.3.2	$T_1$ -angular dependence measurements	51
4.4	Discussion	51
4.4.1	The temperature dependence of $T_1$	51
4.4.2	The angular variation of $T_1$	56
CHAPTER 5:	SPIN-LATTICE RELAXATION OF $\text{Fe}^{3+}$ IN IRON-DOPED MAGNESIUM OXIDE	58
5.1	Crystal structure, doping and charge compensation	58
5.2	Experimental results and discussion	59
5.2.1	Observation of two decay rates	60
5.2.2	Temperature dependence of $T_1$	61
5.2.3	Concentration dependence of $T_1$	64
5.2.4	The angular variation of $T_1$	65
5.2.5	Frequency dependence of $T_1$	66
5.3	Conclusion	66



CHAPTER 6: CAVITY GROWTH IN NEUTRON IRRADIATED  
MAGNESIUM OXIDE

6.1	Introduction	68
6.2	Experimental	69
6.3	Results	70
6.3.1	Transmission Electron Microscopy	70
6.3.2	Electron Spin Resonance	72
6.4	Discussion	73

REFERENCES	78
------------	----

APPENDIX	Publications	88
----------	--------------	----

## CHAPTER 1

### INTRODUCTION

#### 1.1 The aim of the work

Paramagnetic resonance measurements for gadolinium trivalent ions ( $\text{Gd}^{3+}$ ) in single crystals of calcium tungstate ( $\text{CaWO}_4$ ) were reported first by Hempstead and Bowers, 1959 (1). These authors stated some principal advantages for using  $\text{CaWO}_4$  as a host lattice. These were mainly that the paramagnetic ion in a  $\text{CaWO}_4$  lattice substitutes for a calcium ion leading to an identified single spectrum; its small linewidth, since the width contribution from the nuclear magnetic moments of the neighbouring ions is practically negligible, and the suitability of the material because of its hardness and stability. They concluded that  $\text{Gd}^{3+}$  makes a potentially useful material for three-level masers. Previously, Scovil, Feher and Seidel, 1957 (2) showed that gadolinium ethyl sulphate operates as a solid state maser and the ion  $\text{Gd}^{3+}$  seems suitable since its eight energy levels give the choice of several modes of maser operation.

Calcium tungstate assumed technological importance in the 1960's with the discovery that single crystals could be grown doped with neodymium ( $\text{Nd}^{3+}$ ) in concentrations suitable for laser action, Johnson et al, 1962 (3). More recently there have been interests in scheelite structure tungstates and molybdates for acousto-optic device applications.

These applications of scheelite structure crystals have stimulated studies of crystal growth, doping, defects, thermal and optical vibrational properties, elastic properties (Farley, 1973 (4)) and electron spin resonance measurements (Buckley, 1973 (5)). Investigation



of the ESR linewidths for  $\text{Nd}^{3+}/\text{CaWO}_4$  at 35 GHz and 4.2 K was undertaken by G Brown et al, 1974 (6), both experimentally and theoretically for a range of neodymium concentrations. They concluded that the homogeneous broadening was found to be due almost exclusively to the Nd-Nd dipolar interaction indicating that the  $\text{Nd}^{3+}$  ions replace the calcium ions substitutionally in the  $\text{CaWO}_4$  host lattice. A similar study for  $\text{Gd}^{3+}/\text{CaWO}_4$  was reported by J S Thorp et al, 1974 (7) and their results could be regarded as additional evidence for the validity of the Gd-Gd dipolar interaction in determining the angular variation of the linewidths. This, also, implied that the  $\text{Gd}^{3+}$  ions enter the host lattice of  $\text{CaWO}_4$  substitutionally at the calcium sites.

Furthermore, a study on  $\text{Gd}^{3+}/\text{CaWO}_4$  was initiated by Thorp, Buckley and Brown, 1974 (8) to investigate the spin-lattice relaxation behaviour of this material at 37.5 GHz. They indicated that, over the temperature range from 1.5 to 8 K, the recovery was dominated by the direct process.

The main aim of our present studies is to investigate some problems encountered in the preceding studies on pure and gadolinium-doped calcium tungstate. These remaining problems, regarding  $\text{CaWO}_4$  are presented as follows.

1. The previous published data about the dielectric constants of pure  $\text{CaWO}_4$ , by Komandin et al, 1960 (9) and Brower and Fang, 1969 (10), revealed an apparent discrepancy in the results. So we found it appropriate to make new measurements, provided in Chapter 2, as a contribution to solving this problem. Moreover, we extended these dielectric measurements to samples of  $\text{CaWO}_4$  single crystals doped with gadolinium and neodymium for which, to our knowledge, no previous

data were published. Although measurements of dielectric constants are not of a direct concern in the ESR and relaxation studies, knowledge of the dielectric behaviour of these materials is needed for the matching conditions for the ESR spectrometers.

2. The splitting of the gadolinium transitions observed in the studies of  $\text{Gd}^{3+}/\text{CaWO}_4$  reported by H P Buckley, 1973 (5) was a rather interesting phenomenon. In Chapter 3, we are going to investigate the cause and nature of this splitting. We suggest that this may be due to ordered oxygen vacancies in the calcium tungstate lattice.

3. The study of the spin-lattice relaxation behaviour of  $\text{Gd}^{3+}/\text{CaWO}_4$  with temperature reported by Thorp, Buckley and Brown, 1974 (8) revealed that the relaxation displayed a direct process in as far as 8 K. Subsequently, our aim was to extend the range of temperature and to investigate the spin-lattice relaxation at high temperatures. This is discussed in Chapter 4.

As regards magnesium oxide ( $\text{MgO}$ ), the interest in its study began initially with some industrial problems. Magnesium oxide, because of its insulating properties, is used very often as an insulator in heating elements. It has been found that at rather high temperatures ( $\sim 800^\circ\text{C}$ ) the insulating behaviour of the  $\text{MgO}$  collapses and, consequently, the material conducts leading to the failure of the heating element. It has been suggested that the diffusion of impurities from the sheath of the element, mainly iron, into the magnesium oxide could be a possible explanation for the occurrence of such breakdown; nonetheless, this argument has not been proved yet and is still under study in this Department. Besides the current measurements of electrical conductivity and dielectric

losses in pure and doped magnesium oxide, ESR studies on iron doped magnesium oxide were carried out in this group (Vasquez, 1975 (11) and Thorp et al, 1976 (12)).

Moreover, we were able to extend our studies on magnesium oxide to a rather different field of interest. That is, the study of the damage caused by neutron-irradiated MgO samples and the consequent nucleation and growth of cavities when annealing these samples in an ambient of argon. The role of iron impurities in MgO is investigated in our studies. Thus, our aim in studying magnesium oxide is presented in the following.

1. With the forementioned interests in studying MgO in this Department, we found it appropriate to extend our knowledge about  $\text{Fe}^{3+}/\text{MgO}$  by studying its relaxation behaviour at 37.5 GHz. This was intended as another example of an S-state ion in a cubic lattice to be compared with  $\text{Gd}^{3+}$  in the scheelite structure (tetragonal system) which is presented in Chapters 3 and 4. This study of the iron-doped magnesium oxide crystals is dealt with in Chapter 5.

2. The knowledge acquired from the ESR studies of iron-doped magnesium oxide was helpful in the interpretation of the ESR spectra of the annealed neutron-irradiated MgO crystals. This was achieved by collaboration with G J Russell (13) who provided the samples and made transmission electron microscope (TEM) studies on them. Transmission electron microscopy on its own was inadequate to identify impurities so the need for the ESR study as a complementary technique was necessary. ESR and TEM studies on the cavity growth in neutron irradiated magnesium oxide are presented in Chapter 6.

## 1.2 Paramagnetic relaxation

Spin-lattice relaxation is, in fact, one way of achieving thermal equilibrium for the spin system with the surrounding lattice. It is interesting to note that the phrase 'spin-lattice relaxation' is sometimes used even in other situations, such as noncrystalline or even liquid paramagnetic materials, where the term 'lattice' is not entirely appropriate and the relaxation process is rather different. In order to describe the mechanism whereby a spin system achieves thermal equilibrium within itself and with its surroundings three processes must be considered. These are spin-spin relaxation, cross relaxation and spin-lattice relaxation. The spin-spin relaxation is the process by means of which the spin system achieves thermal equilibrium within itself, cross relaxation is the attainment of equilibrium between spins of different species, while spin-lattice relaxation describes the way in which the spin system transfers energy to the lattice.

The first calculation of the spin-spin relaxation time  $T_2$  was performed by Waller, 1932 (14) considering a simple  $S = \frac{1}{2}$  system in low magnetic field. For pure paramagnetic salts with typical interatomic spacings of a few angstroms,  $T_2 \simeq 10^{-9}$  sec, and even in magnetically dilute systems,  $T_2$  is very short in comparison with the spin-lattice relaxation time  $T_1$ . An important conclusion is that since  $T_2$  does not involve the lattice energy, it is essentially temperature independent.

In studying the case of  $S > \frac{1}{2}$  or systems containing more than one type of spin centre, cross relaxation must be considered. This was discussed by Bloembergen et al, 1959 (15) and further by Grant, 1964 (16). When the levels of a single multi-level spin system are

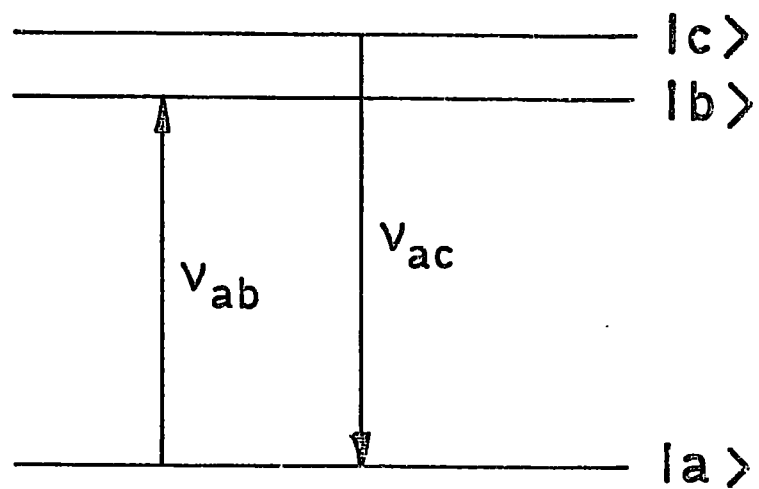


FIG. 1-1 Diagrammatic representation of cross relaxation between levels  $|b\rangle$  and  $|c\rangle$ .

similar, but not identical (as depicted in Figure 1.1 where the levels  $|b\rangle$  and  $|c\rangle$  are close in energy and separated from level  $|a\rangle$ ) the difference in frequencies ( $\nu_{ac} - \nu_{ab}$ ) is very much less than  $\nu_{ab}$  or  $\nu_{ac}$ . The spin energy may then be transferred by the transition of one, or more, excited ions (in level  $|c\rangle$ ) to their ground state (level  $|a\rangle$ ) with the simultaneous transition of a non-excited ion (level  $|a\rangle$ ) to an excited state (level  $|b\rangle$ ); this conserves the Zeeman energy, the small unbalance of energy being taken up by the dipolar or internal energy of the spin system.

Other energy-level situations are considered by Bloembergen et al, wherein pairs of levels occurred with similar but not identical separations as illustrated in Figure 1.2. Cross relaxation can also be effective even when the levels  $|b\rangle$  and  $|c\rangle$  are quite widely separated (Figure 1.2b). It was mentioned by Standley and Vaughan, 1969 (17) that Figure 1.2a is appropriate to  $\text{Ni}^{2+}$  in an axial crystal field and a moderate magnetic field and Figure 1.2b is an example of the  $\text{Cr}^{3+}$  ion in an axial field. In general, cross relaxation can occur within the spin system A and B with a finite transition probability with  $(m+n)$  spins taking part, when  $m$  spins of type A flip up say while  $n$  spins of type B flip down so that

$$m (h \nu_{ab}) = n (h \nu_{ac}) \quad (1.1)$$

The probability of this process occurring is very likely to be small unless  $m$  and  $n$  are integers close to unity. This process has become known as 'harmonic cross-relaxation'. Measurements of cross-relaxation times  $T_{12}$  (Pershan, 1960 (18), Mims and McGee, 1960 (19)), and harmonic cross-relaxation (Kopvillem, 1961 (20)) are in fairly



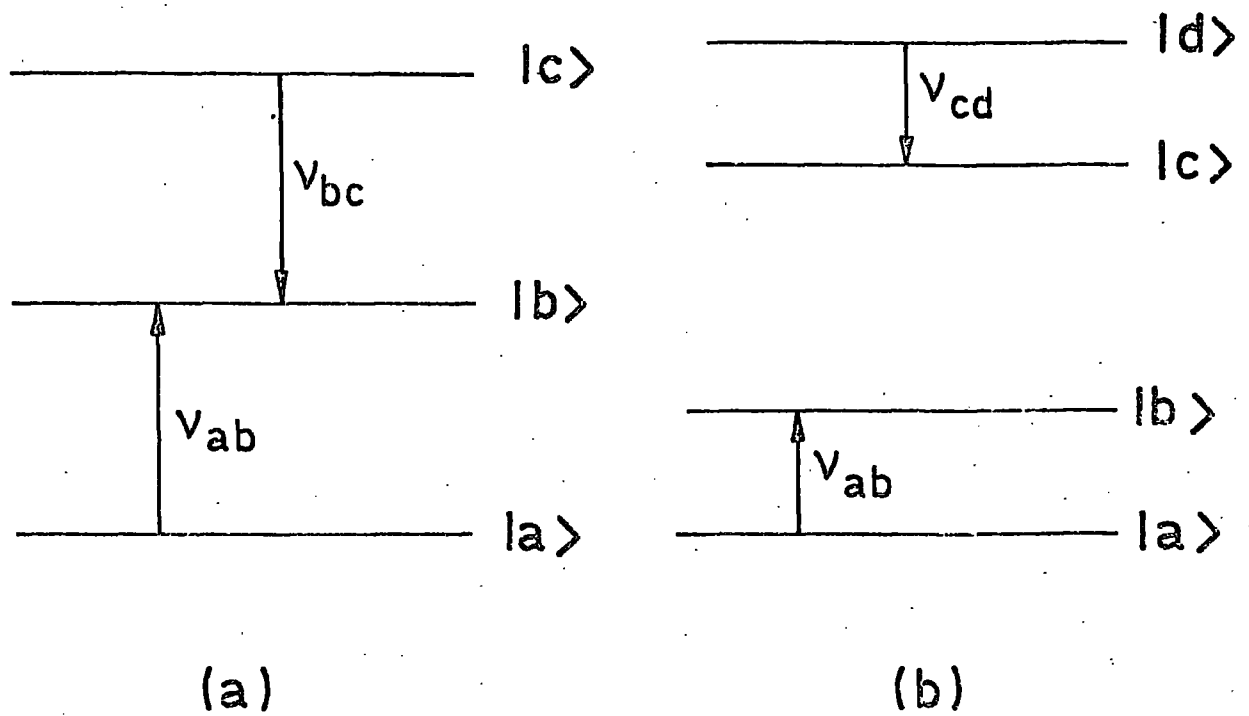


FIG. 1-2 Another energy-level system wherein cross relaxation is highly probable to occur.

good agreement with the theories of Bloembergen and Grant. In the context of our studies it is concluded that the minima observed in the angular plot of the spin-lattice relaxation times of  $\text{Fe}^{3+}/\text{MgO}$  are probably due to such effects of cross-relaxation as mentioned in Chapter 5.

### 1.3 The measurement of relaxation time

Several authors have described the methods which have been widely used for the determination of spin-lattice relaxation. These methods could be classified as :-

#### (a) Resonant methods

1. CW saturation (Eschfeld and Weidner, 1953 (21))
2. DC magnetization (Feng and Bloembergen, 1963 (22))
3. Pulse saturation (Davis, Strandberg and Kyhl, 1958 (23))
4. Inversion recovery (Castle, Chester and Wagner, 1960 (24))
5. Pulse response (Brown and Thorp, 1967 (25))
6. AC saturation (Herve and Pescia, 1960 (26))
7. Ultrasonic method (Dobrov and Browne, 1963 (27))

#### (b) Non-resonant methods

1. Absorption methods
2. Dispersion measurements
3. Measurements at liquid helium temperature.

The experimental results of the latter methods have been summarized and discussed by Gorter, 1947 (28) and Cooke, 1950 (29). The concentrated magnetic salts usually employed in the non-resonant experiments do not conform at all to the models used in the theoretical approaches

to spin-lattice relaxation, nor are the parameters determined generally directly comparable with those found by the resonance techniques (17).

In our measurements we adopted the pulse saturation method both for being a widely accepted technique for measuring spin-lattice relaxation times and also for the sake of comparison with previous results (8) that were already made with this technique.

#### 1.3.1 The pulse saturation method

This technique has been used many times, principally by Davis, Strandberg and Kyhl, 1958 (23), Bowers and Mims, 1959 (30), Pace, Sampson and Thorp, 1960 (31). Recently it was used by H P Buckley, 1973 (5) for preliminary studies of  $T_1$  for  $Gd^{3+}/CaWO_4$ . The method employs two klystrons; one for monitoring the resonance (low power klystron) and the other for providing a saturating pulse (high power klystron) at the same frequency. The saturating pulse equalizes the populations of the two spin levels being investigated and hence absorption of power from the monitor klystron ceases to occur. After the end of the pulse the populations of the levels begin to revert to their thermal equilibrium values, and as this occurs an increasing amount of power is absorbed from the monitor klystron. The receiver picks up this increasing absorption signal and it is recorded as a function of time on a cathode-ray oscilloscope. By definition, the spin levels revert to their undisturbed state in an exponential manner, the time constant of which is the spin lattice relaxation time  $T_1$ , and it is this exponential which is recorded on the display. Figure 1.3 shows a block diagram of the circuitry of the Q-band spectrometer used for these measurements with the

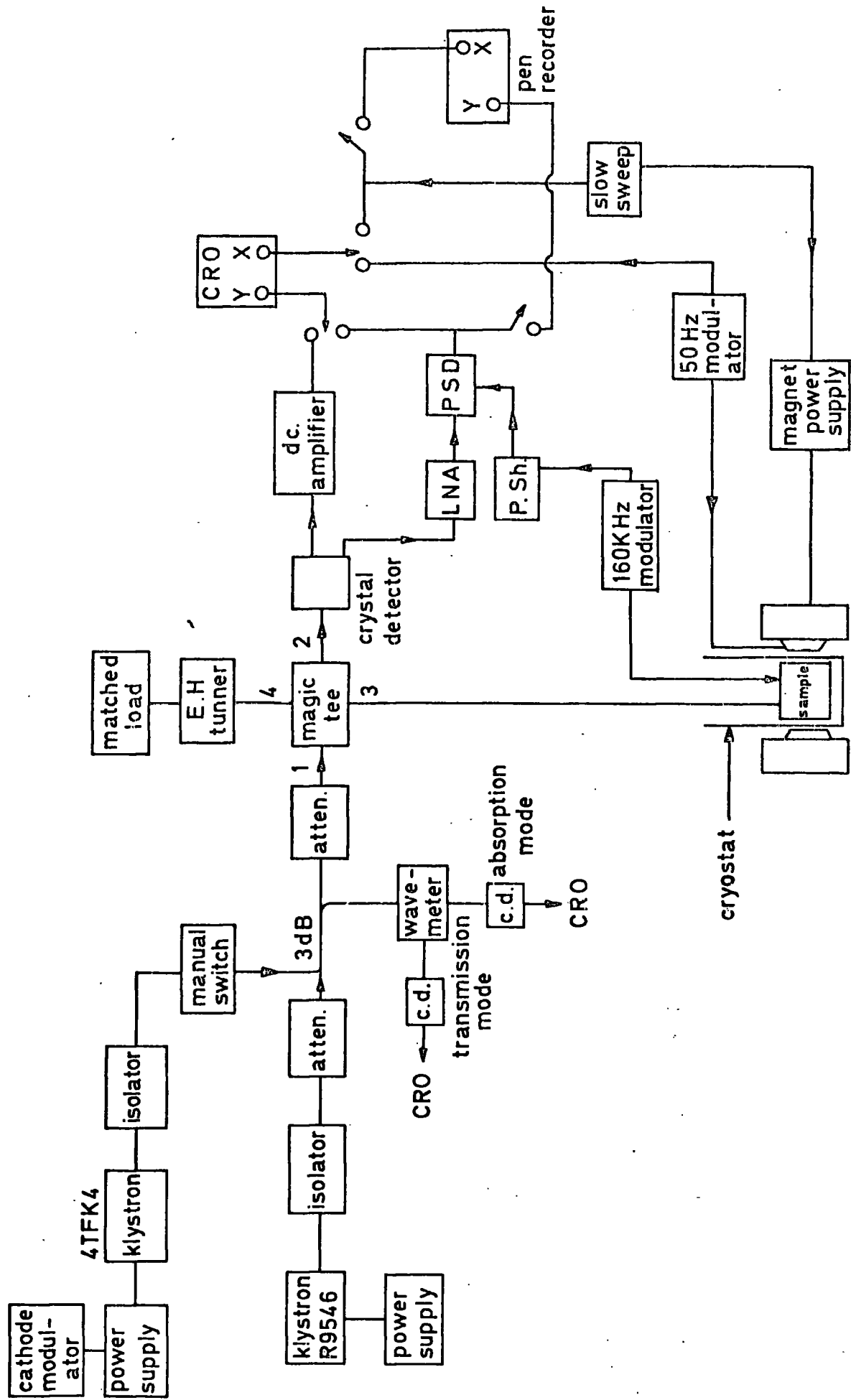


FIG.1-3 Block diagram of Q-band spectrometer , with pulse saturation facilities.

facilities required for the pulse saturation method. This has become the standard technique for measuring relaxation times; it is theoretically possible for this method to resolve any number of relaxation times which may be present. This is demonstrated in our measurements of  $T_1$  for  $\text{Fe}^{3+}/\text{MgO}$  where two components in the recovery traces were observed (Chapter 5).

### 1.3.2 Relaxation rate equations

When a spin makes a relaxation transition in one direction or the other, it simultaneously exchanges a quantum of energy with the lattice thermal vibrations and, hence, it is termed 'spin-lattice relaxation'. A treatment to derive the relaxation rate equations was reported by Siegman, 1964 (32) which led to the form

$$\Delta n(t) = \Delta N + (\Delta n_0 - \Delta N) e^{-(\omega_{12} + \omega_{21})t} \quad (1.2)$$

This says that if the population difference  $\Delta n$  is initially somehow perturbed away from the thermal-equilibrium value  $\Delta N$ , then the relaxation process will act to return the system to thermal equilibrium with a relaxation time constant which can be written as

$T_1 = (\omega_{12} + \omega_{21})^{-1}$ ; the spin-lattice relaxation time. (It is sometimes also termed the longitudinal relaxation time  $\tau$ ). The terms  $\omega_{12}$  and  $\omega_{21}$  are the upward and downward relaxation transition probabilities per spin per unit time, respectively. In the case which usually applies at microwave frequencies, the condition

$$(E_2 - E_1) / kT \ll 1 \quad (1.3)$$

is obeyed, where  $(E_2 - E_1)$  is the energy difference between levels 2 and 1, then the approximation  $\omega_{12} = \omega_{21}$  may be made in which case

$$T_1 = 1/2\omega_{12} \quad (1.4)$$

This was evaluated for a two-level spin system. Generally, in the case of a multilevel spin system containing  $p$  levels, relaxation will be a complex process involving all the levels, and the general rate equation for the  $i^{\text{th}}$  level will be

$$\frac{d n_i}{dt} = \sum_{\substack{j=1 \\ j \neq i}}^p (\omega_{ji} n_j - \omega_{ij} n_i) \quad (1.5)$$

where  $n_i$  is the spin population of the  $i^{\text{th}}$  level, and the transition probabilities between any two levels will be in the Boltzmann ratio of the populations of those two levels

$$\omega_{ij}/\omega_{ji} = \exp \left[ (E_j - E_i)/kT \right] \quad (1.6)$$

The relaxation behaviour of the system will be controlled by  $(p-1)$  relaxation times  $T_1^{(ij)}$ , where

$$T_1^{(ij)} = (\omega_{ij} + \omega_{ji})^{-1} \quad (1.7)$$

Using this relation, the rate equation for the  $i^{\text{th}}$  level can be written in the form

$$\frac{d n_i}{dt} = - \sum_{\substack{j=1 \\ j \neq i}}^p \frac{\Delta n_{ij} - [(n_i + n_j)/(N_i + N_j)] \Delta N_{ij}}{2 T_1^{ij}} + \omega_{ij} \Delta n_{ij} \quad (1.8)$$

where  $N_i$ ,  $n_i$  are the thermal-equilibrium population and the instantaneous population of level  $i$  also,

$$\left. \begin{aligned} \Delta n_{ij} &= n_i - n_j, \text{ and} \\ \Delta N_{ij} &= N_i - N_j \end{aligned} \right\} \quad (1.9)$$

The solution of equation (1.8) for the time varying population of level  $i$  will be the sum of exponential terms of the form

$$n_i(t) = n_{i0} + \sum_{\substack{j=1 \\ j \neq i}}^p C_{ij} \exp - (t/T_1^{ij}) \quad (1.10)$$

which must be evaluated numerically. In experiments, the relaxation behaviour of a particular level will frequently be dominated by one of the  $T_1^{(ij)}$ 's, having a large amplitude constant  $C_{ij}$ , and this will be the time constant of the observed relaxation recovery, although more than one exponential may be observed.

#### 1.4 Experimental Techniques

Regarding the ESR measurements we have used a conventional Q-band spectrometer with a low power reflex klystron working over a frequency range 33.0 - 37.75 GHz, with facilities for broad-line ESR display and pulse saturation relaxation time measurements. The experimental arrangement of the spectrometer is shown in block diagram form in Figure 1.3. This spectrometer was running previously with a superhet detection system, e.g. as reported by Kirkby, 1967 (33). Buckley in 1973 (5) found that, without using the superhet detection system, the phase-sensitive detector was sufficient to produce relatively noise free signals. In our present work we are adopting Buckley's technique since it has proved its reliability. We are not going to discuss the function of the spectrometer in detail since a thorough study of spectroscopic techniques at millimetric wavelengths had been reported by G Brown, 1967 (34) in this group.

However, there is a specific feature for our Q-band spectrometer that makes it slightly different from other conventional ones. This is that we are not using a proper cavity to contain the paramagnetic sample. Instead, we have short-circuited the waveguide by a brass plunger which was fitted inside the end of the waveguide where the outside d.c. magnetic field could be applied to the sample. The only disadvantage in using this technique is the reduction of the Q-factor of the system; which was estimated by Kirkby (using a technique described by Montgomery, 1948 (35)) as an unloaded value of around 400. On the other hand, the absence of a cavity made it easier for the setting of the two klystrons used during measurements of spin-lattice relaxation time. Besides, we were able to use simpler cryogenic facilities than would have been possible with a larger cavity in the restricted pole-piece gap.

The low power signal source was an E.M.I. reflex klystron type R9546, mounted in an oil-bath for good frequency stability. Measurement of frequency was made by means of a combined transmission-absorption wavemeter, which was also used in relaxation measurements for bringing the high power klystron frequency into coincidence with the signal klystron. The high power saturating pulses were obtained from an Elliott water-cooled klystron, type 4TFK4 working around 37.5 GHz and fed into the system by means of a manual switch. The bridge element was a magic tee by which the microwave power entering from arm 1 was split equally between the sample arm 3 and the matching arm 4 that composed of an E.H. tuner and a matched load. The two reflected waves were detected in arm 2 with a crystal detector. In the off-resonance condition the E.H. tuner was adjusted until the reflected power at the crystal detector was zero. This meant that the reflected power from the sample was balanced out by the reflected



power from the adjustable E.H. tuner arm. Then, the bridge was taken slightly off balance in amplitude only in order to observe pure absorption signal. When resonance occurred an off-balance signal was detected. Detection and display of the absorption spectrum was carried out in several ways depending on the type of measurements to be made. For video display the signal was fed through a d.c. amplifier to an oscilloscope, using a large amplitude 50 Hz modulation of the magnetic field to sweep completely through each line. This 50 Hz modulation was achieved by placing an auxiliary modulation coil designed to be a push fit into the magnet bore and its magnetic field being coaxial with that of the magnet. In the case of displaying relaxation recovery traces, the 50 Hz modulation was switched off. In plotting derivatives of the absorption spectrum a higher sensitivity was found necessary and for this purpose a modulation of high frequency and small amplitude was used, together with phase-sensitive detection. The system was then connected to a pen-recorder, the x-axis of which was driven from the slow sweep of the magnetic field. The high frequency modulation was achieved by using an oscillator at 160 kHz and coils attached to the plunger which terminated the waveguide such that the samples were nearly concentric with the coils. The magnetic fields necessary for ESR at Q-band were found to be of the order of 1.5 tesla, with a homogeneity of better than 1 part in  $10^5$  over a volume of  $1 \text{ cm}^3$ . The calibration of the field was carried out using a combined proton-lithium magnetometer. The magnet used with this spectrometer was a Newport type D electromagnet provided with a current stabilizing unit and a slow sweep unit. Cryogenic facilities were used to enable measurements at liquid helium, liquid nitrogen temperatures and temperatures inter-between.

#### 1.4.1 Measurement of spin-lattice relaxation time $T_1$

Applying the pulse saturation method (Davis et al, 1958 (23)) we were able to measure the spin-lattice relaxation times for both  $\text{Gd}^{3+}/\text{CaWO}_4$  (Chapter 4) and  $\text{Fe}^{3+}/\text{MgO}$  (Chapter 5). With this technique the behaviour of the spin system was observed following the removal of a saturation pulse of the high power klystron (20 W); changes were monitored by observing the absorption of power from the low power klystron (20 mW). As the spins relaxed after the pulse, and the population difference was restored towards thermal equilibrium, the recovery traces could be represented by the variation in spin populations with time which obeyed either equation (1.2) or equation (1.10), depending upon whether we are observing one or more relaxation constants.

Experimentally, the samples were oriented and the frequencies of the high power and monitor klystrons were brought into coincidence using the transmission-absorption wavemeter. The spectrometer was then adjusted for balance and the magnetic field was set at the centre of the absorption transition. Next, saturation pulses with time duration of 30 m sec and rate of repetition within 1-10 cycle/sec were applied to the sample. The pulse train displayed on the oscilloscope was of constant height, except for a slight 50 Hz ripple which was due to the A.C. heaters. This was greatly improved by using a separate D.C. supply for the klystron heaters. The relaxation to equilibrium, as monitored by the low power source, was displayed on the C.R.O., using the d.c. amplifier. We used a Polaroid camera to record the recovery curves photographically, using a slow pulse repetition rate. A typical photograph is shown in Figure 1.4. The relaxation times were derived from the photographs by replotting the ordinates (which are proportional to  $\Delta n(t)$ ) in semilogarithmic form,

## Recovery trace photograph

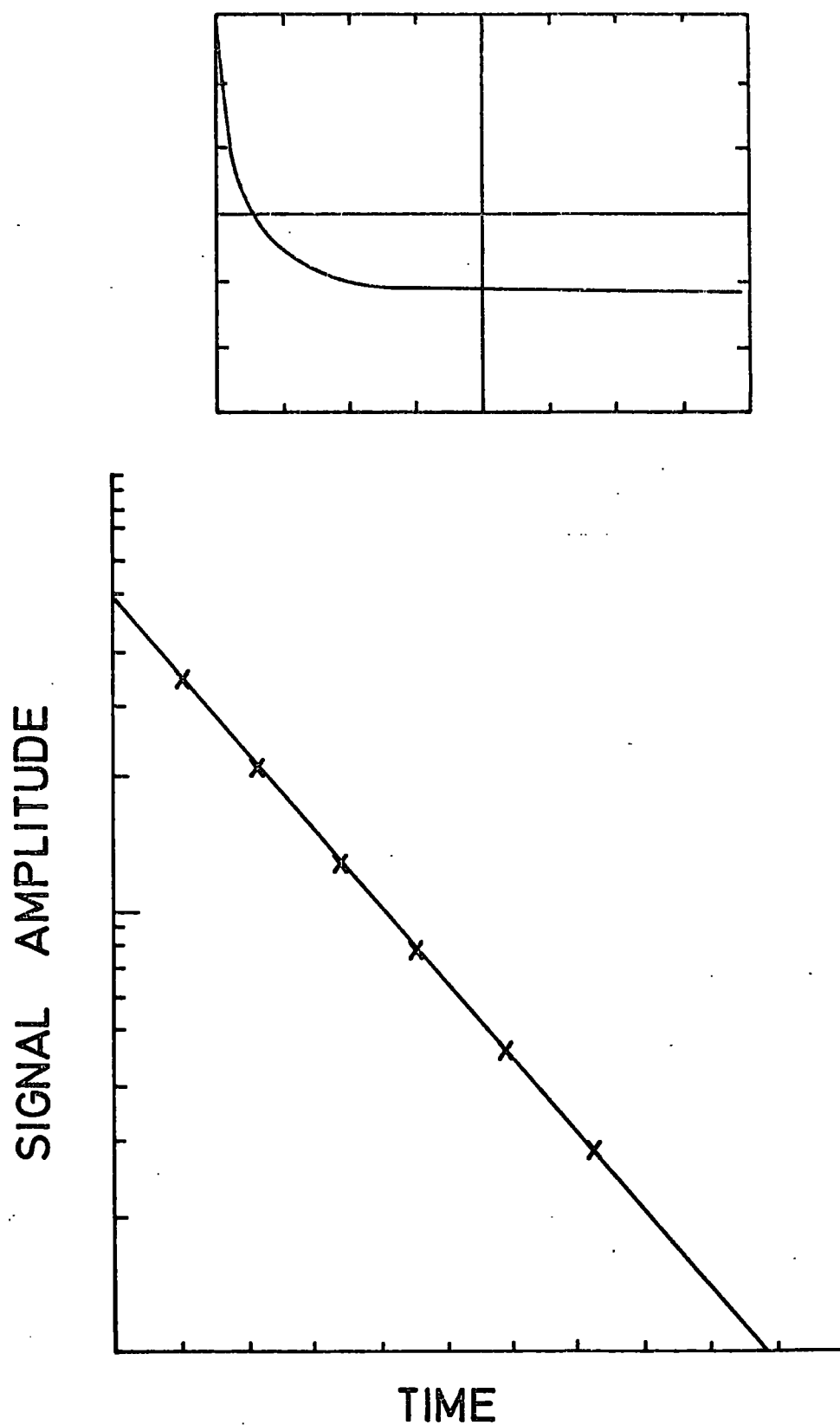


FIG. 1.4 Typical behaviour for relaxation of a simple spin system.

against time on a linear scale. This produced a single straight line in the case of  $\text{Gd}^{3+}/\text{CaWO}_4$  (Chapter 4, Figure 4.4) and more than one slope in the case of  $\text{Fe}^{3+}/\text{MgO}$  (Chapter 5, Figure 5.1). However, any deviation from a single straight line indicates a departure from simple spin lattice relaxation which is not unexpected with a multi level spin system.

The lowest detectable time rate with our CRO was  $0.1 \mu \text{ sec/cm}$ . Also, the fall time of the power pulse obtained from the klystron was about  $3 \mu \text{ sec}$ . This restricted the extent to which we could measure  $T_1$  at higher temperatures.

Measurements of  $T_1$  in the case of  $\text{Gd}^{3+}/\text{CaWO}_4$  were carried out for the transition Nc.4 (this nomenclature was given in reference 7), because it appears as a large amplitude signal at higher fields with no apparent overlap with the other transitions. In the case of  $\text{Fe}^{3+}/\text{MgO}$  measurements were made for the central  $\pm \frac{1}{2} \longleftrightarrow \mp \frac{1}{2}$  main transition.

## CHAPTER 2

### THE DIELECTRIC CONSTANTS OF $\text{CaWO}_4$ , $\text{Nd/CaWO}_4$ and $\text{Gd/CaWO}_4$

#### 2.1 Introduction

Although two measurements of the dielectric constants of pure calcium tungstate have been reported (1,2), the values quoted show a considerable divergence. In the earlier paper (1), Komandin et al, who used an immersion method, stated that the dielectric constant was  $\epsilon' = 21.4$  at  $25^\circ\text{C}$  and 1.72 MHz for solid material, apparently in powder form. Calcium tungstate, however, crystallizes in the scheelite structure; it belongs to the tetragonal system having  $a = b = 5.243 \text{ \AA}$  and  $c = 11.376 \text{ \AA}$  (3); more details of the structure are given in the next chapter, section 3.1. Consequently, two components are necessary to describe the dielectric tensor. In the later paper, Brower and Fang (2) gave results for measurements on oriented pure single crystal slices. They found that the dielectric constant was anisotropic, that the dielectric constants parallel to the a-axis and c-axis were 11.7 and 9.5, respectively, at  $24.5^\circ\text{C}$ , and that these values were the same for frequencies of 1.59 KHz and 1 MHz. The measurements reported here were made primarily to clarify the situation in pure calcium tungstate and also to obtain data on some neodymium- and gadolinium-doped calcium tungstate single crystals in order to assist optimization of the matching conditions during electron spin resonance and relaxation studies in them; to our knowledge no previous measurements on doped calcium tungstate have been published.

#### 2.2 Experimental

The single crystals used, (obtained from I.R.D. Co. Ltd., Newcastle), were grown by the Czochralski method (4). In the pure and

gadolinium-doped crystals, charge compensation was achieved by vacancy incorporation, and in the neodymium-doped crystals by sodium addition. The single crystal boules, whose dimensions were typically 6 cm long and 1.5 cm diameter, were first oriented by Laue back-reflection X-ray methods which gave orientation accuracies of  $\pm 15'$  of arc. Specimens of known orientation were then prepared by making appropriate slices with a diamond wheel cutting machine and precision polishing their faces with diamond paste to a 0.25  $\mu\text{m}$  finish. The larger faces of the specimens were limited by the boule dimensions to about 1 cm x 1 cm in area and were cut in the plane of either the a- or c-axis (see Figure 2.1). The specimen thickness, usually 0.3 mm, represented the minimum which could readily be achieved without fracturing the slice during fabrication. Circular gold electrodes were deposited by evaporation on the larger polished faces to ensure good electrical contact over a defined area between the crystal and the electrodes of the dielectric testing jig.

The measurements were made in air at room temperature over the frequency range 1 to 40 MHz using a standard Q-meter (Marconi TF 1245) and the oscillator (Marconi TF 1246). Measurements were then extended to 80 MHz using an oscillator (Marconi TF 1247) whose operating range extended from 20 to 300 MHz. The dielectric testing jig (Marconi TJ 155C/1) was modified to allow the use of 10 or 6 mm diameter circular jig electrodes as specimen dimensions were limited by the size of the single crystals available. In this technique, measurements were made firstly with the specimen mounted in the jig and secondly, at the same jig electrode spacing, without the specimen. The difference in capacity enabled the real part of the dielectric constant,  $\epsilon'$ , to be derived; in a similar manner the difference in Q-value with and without the specimen allowed the dielectric loss,  $\tan \delta$ , to be evaluated.

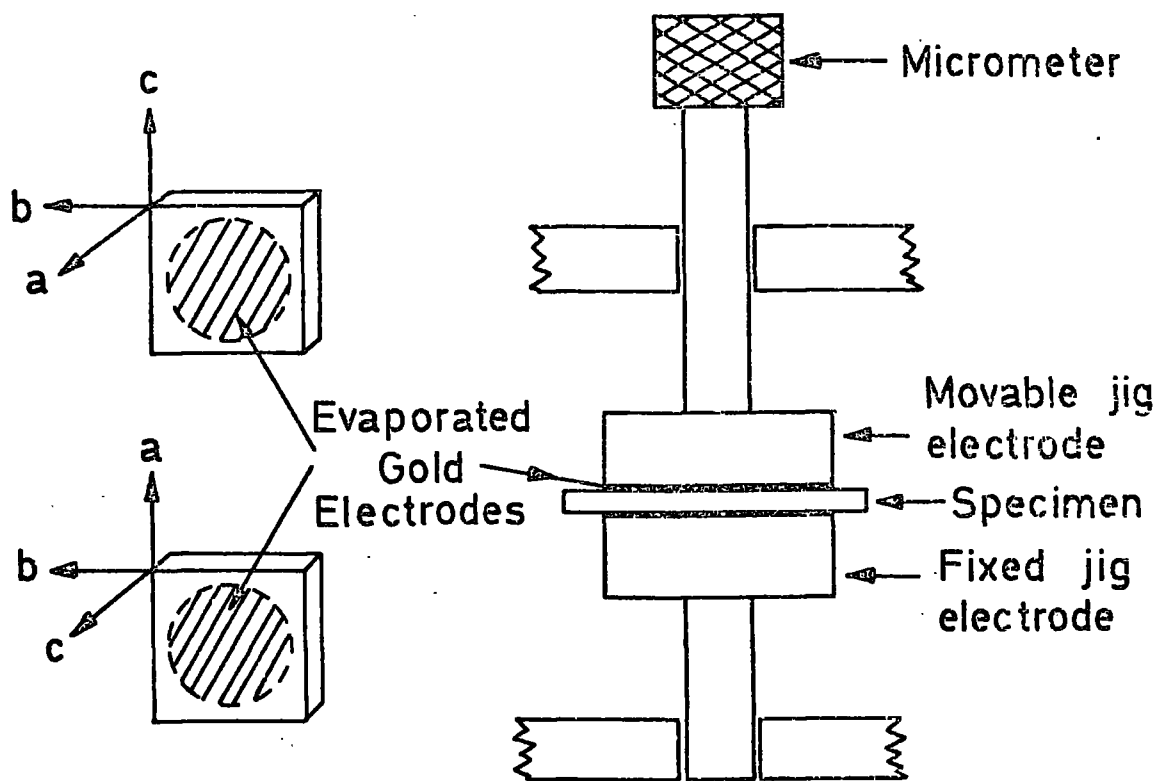


FIG. 2-1 General form of specimens and dielectric testing jig.

### 2.3 Derivation of $\epsilon'$ and $\tan \delta$

When using the Q-meter with or without the specimen we actually observe the resonance condition,

$$\omega = \sqrt{\frac{1}{LC}} \quad (2.1)$$

where  $\omega$  is the operating frequency, L and C are the total inductance and total capacitance of the circuit, respectively. So, maintaining  $\omega$  and L constant whether the sample is in or out of the testing jig, we can equate C in both cases to a value which we will denote as  $C_T$ . The total capacitance  $C_T$  is the sum of the air gap capacitance  $C_O$  when the sample is out, with the spacing of the jig electrodes exactly as the thickness of the sample, the Q-meter capacitance in this case,  $C_1$ , the holder capacitance  $C_H$ , the leads capacitance  $C_L$  and the internal capacitance of the equipment  $C_i$ . Thus at resonance, without the sample,

$$C_T = C_1 + C_O + C_H + C_L + C_i \quad (2.2)$$

In the case when the sample is in the testing jig, we refer to the sample capacitance by  $C_X$ . Thus, at resonance with the sample in ,

$$C_T = C_2 + C_X + C_H + C_L + C_i \quad (2.3)$$

From (2.1), (2.2) and (2.3) we find that

$$C_1 - C_2 = C_X - C_O \quad (2.4)$$

Neglecting the edge effects, it can be shown that the capacitance  $C_X$  of a parallel plate capacitor with a relative permittivity (dielectric constant)  $\epsilon'$  is expressed as



$$C_X = \epsilon' C_O \quad (2.5)$$

$$C_O = \epsilon_O \frac{A}{d}$$

where A is the area of the electrodes in square metres, d the thickness of the sample in metres and  $\epsilon_O$  is called the permittivity of free space having a value of  $8.854 \text{ pF m}^{-1}$ ; this yields the value of the capacitance in pico Farad.

Therefore, from (2.4) and (2.5) we get

$$\begin{aligned} C_1 - C_2 &= \epsilon' C_O - C_O \\ &= C_O (\epsilon' - 1) \end{aligned}$$

or

$$\epsilon' = \frac{C_1 - C_2}{C_O} + 1 \quad (2.6)$$

Also, the numerical value of the loss,  $\tan \delta$ , can be evaluated from the expression (5)

$$\tan \delta = \frac{Q_1 - Q_2}{Q_1 \cdot Q_2} \cdot \frac{C_1}{C_1 - C_2} \quad (2.7)$$

in which  $C_1$  and  $C_2$  are the capacitances indicated by the Q-meter at resonance with the specimen out of and in the testing jig, respectively, and  $Q_1$  and  $Q_2$  are the corresponding Q-values.

In the present experiments, however, the specimens were, for convenience, cut in the form of squares and so some crystal protruded beyond the circular jig electrodes. Consequently, a correction for edge effects was necessary. Various formulae have been given previously (6), and following similar methods, equation (2.6) can be modified to

$$\epsilon' = \frac{C_1 - C_2}{C_o + C_e} + 1 \quad (2.8)$$

where  $C_e$  is the edge correction for the capacitance given by

$$C_e = \frac{1.113D}{8\pi} \left[ \ln \frac{8\pi D}{d} - 3 \right] \quad (2.9)$$

for the experimental conditions used in which, for any electrode diameter  $D$  employed, the thickness of each evaporated gold electrode was very small compared with  $d$ , the specimen thickness. These equations were used in deriving the numerical data presented; it was found that the correction term amounted to about 8%. The edge effect correction for  $\tan \delta$  was negligible.

## 2.4 Results

The dielectric constant data obtained at 1 MHz are summarized in Table 2.1 in which the values given under 'present work' represent averages for several measurements on each individual specimen. For the pure material at 1 MHz we find that parallel to the a-axis,  $\epsilon'_a = 11.3 \pm 0.4$  and that parallel to the c-axis,  $\epsilon'_c = 9.1 \pm 0.4$ . In the doped crystals, the values of  $\epsilon'_a$  and  $\epsilon'_c$  at 1 MHz were the same within experimental error, as those for pure calcium tungstate.

The variation of the dielectric constants at frequencies above 1 MHz is shown in Figure 2.2. A very slight increase in both  $\epsilon'_a$  and  $\epsilon'_c$  was observed above about 20 MHz to 40 MHz, but the anisotropy of the dielectric constant, as measured by the ratio  $\epsilon'_a/\epsilon'_c$  remained unaltered. There was no significant difference between the behaviour of the pure calcium tungstate crystals and the neodymium- or gadolinium-doped specimens.

With regard to the dielectric loss,  $\tan \delta$ , for pure calcium tungstate increased slowly from 0.005 at 1 MHz to about 0.01 at 40 MHz.

Reference	Pure $\text{CaWO}_4$		Nd / $\text{CaWO}_4$		Gd / $\text{CaWO}_4$	
	$\epsilon'$	$\epsilon'_a$	$\epsilon'_c$	Doping level (nominal)	$\epsilon'_a$	$\epsilon'_c$
Komandin et al	21.4					
Brower and Fang		$11.7 \pm 0.1$	$9.5 \pm 0.2$			
Present work		$11.3 \pm 0.4$	$9.1 \pm 0.4$	1%	$11.5 \pm 0.4$	$9.5 \pm 0.4$
				0.1%	$11.1 \pm 0.4$	$9.3 \pm 0.4$
				0.05%	$11.5 \pm 0.4$	$9.4 \pm 0.4$
				0.05%	$11.8 \pm 0.4$	$9.1 \pm 0.4$
				0.01%	$11.1 \pm 0.4$	$8.9 \pm 0.4$

Table 2.1: Dielectric constants for  $\text{CaWO}_4$ , Nd/ $\text{CaWO}_4$  and Gd/ $\text{CaWO}_4$

at 1 MHz in air (doping levels given in at.%).

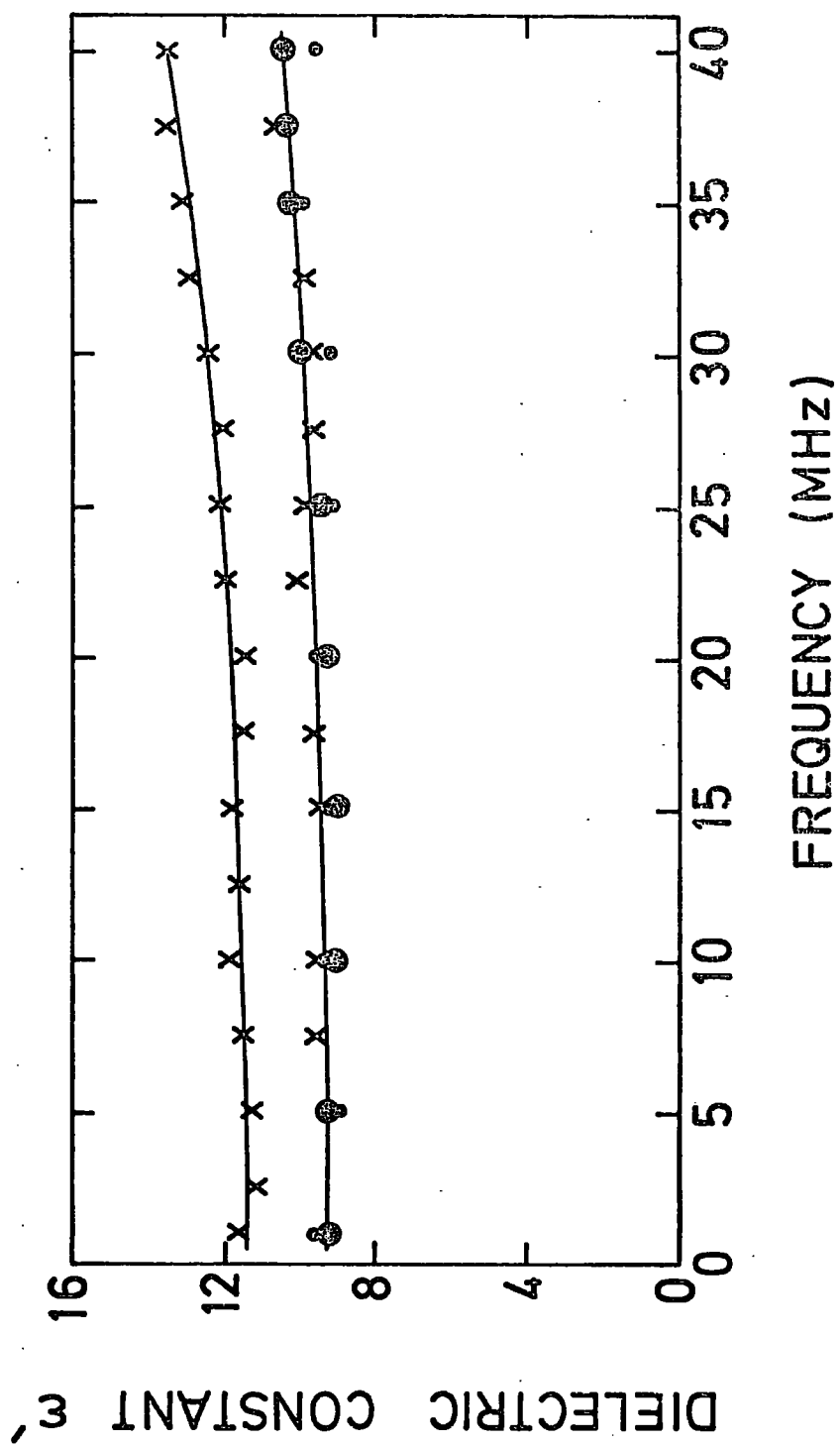


FIG.2.2 Variation of dielectric constant  $\epsilon'$  with frequency  
 x : 0.05 % Nd, • : 0.05 % Gd, ⊙ : pure CaWO<sub>4</sub>.

In contrast to the anisotropy of the dielectric constant, the losses measured parallel to the a- and c-axes were the same. With both neodymium- and gadolinium-doped crystals, similar increases in loss at the higher frequencies were observed (Figures 2.3 and 2.4). The measurements on the doped crystals also showed that, above about 20 MHz, the dielectric loss was larger the higher the dopant concentration. With neodymium doping the effect was quite marked; the true neodymium concentrations in these specimens were determined by optical spectrographic analysis (The Chemical Inspectorate) and, as Figure 2.3 shows, the loss at 40 MHz increased from  $4.5 \times 10^{-3}$  to  $7.2 \times 10^{-3}$  as the concentration rose from 0.05% Nd to 0.1% Nd. In the gadolinium-doped specimens, the effect was not so marked, probably because the true gadolinium concentrations were all very low,  $\sim 50$  p.p.m., and the differences between the specimens were not so pronounced. (The analyses were made by emission spectro-chemistry by the Analytical Services Laboratory, Imperial College). It was also found, as with the pure material, that in all the doped specimens examined, the dielectric loss parallel to the a-axis was the same as that measured parallel to the c-axis.

Measurements of the dielectric loss,  $\tan \delta$ , were extended to 80 MHz for the neodymium-doped samples with concentrations of 0.05% and 0.1% Nd, Figure 2.5. The increase of  $\tan \delta$  with frequency continued showing that  $\tan \delta$  at 80 MHz had increased about five times that at 40 MHz.

## 2.5 Discussion

Considering first the pure calcium tungstate single crystals, the measured values of  $\epsilon'_a$  and  $\epsilon'_c$  at 1 MHz ( $11.3 \pm 0.4$  and  $9.1 \pm 0.4$  respectively) agree very closely with those given by Brower and Fang both as regards the numerical values and in that  $\epsilon'_a > \epsilon'_c$ . The measurements

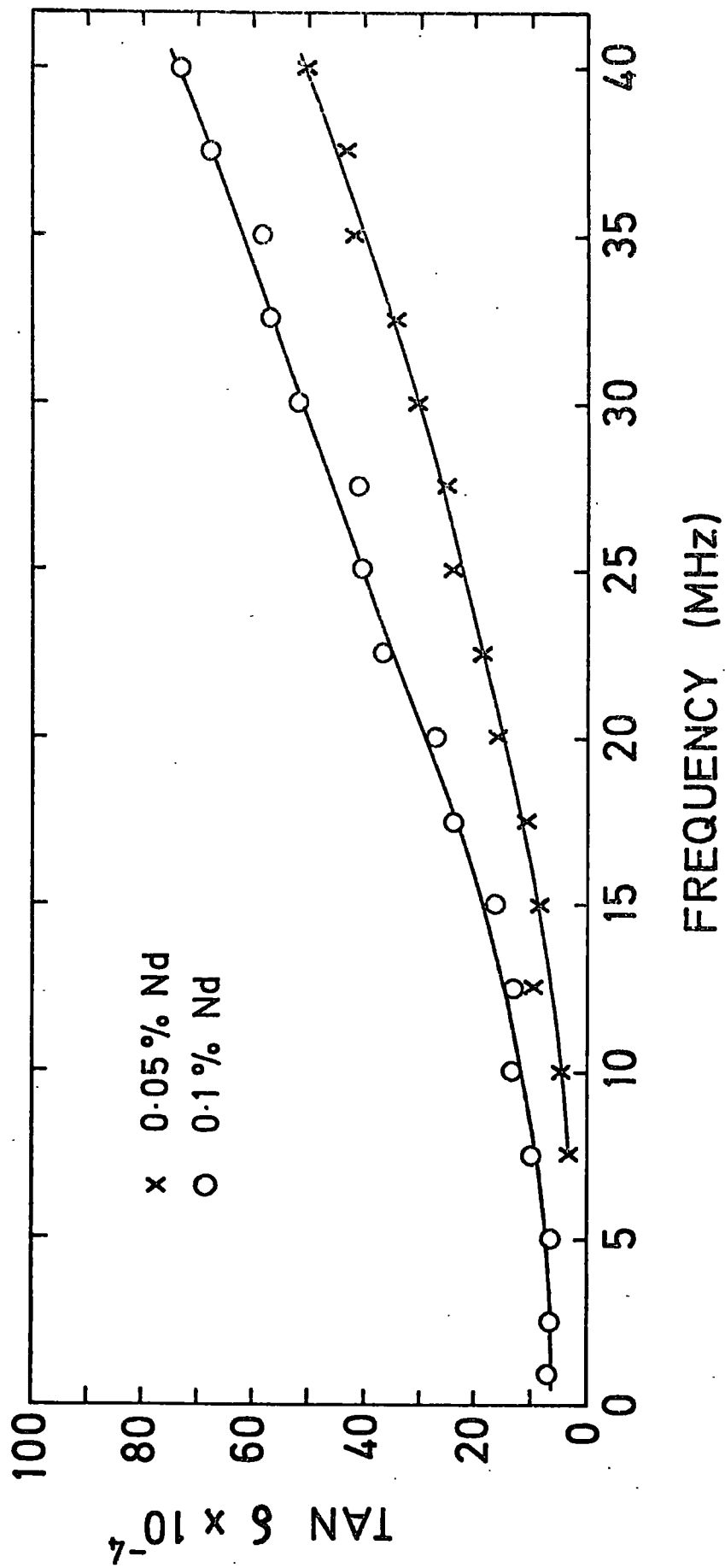


FIG. 2.3 Variation of dielectric loss,  $\tan \delta$ , with frequency for Nd/CaWO<sub>4</sub>.

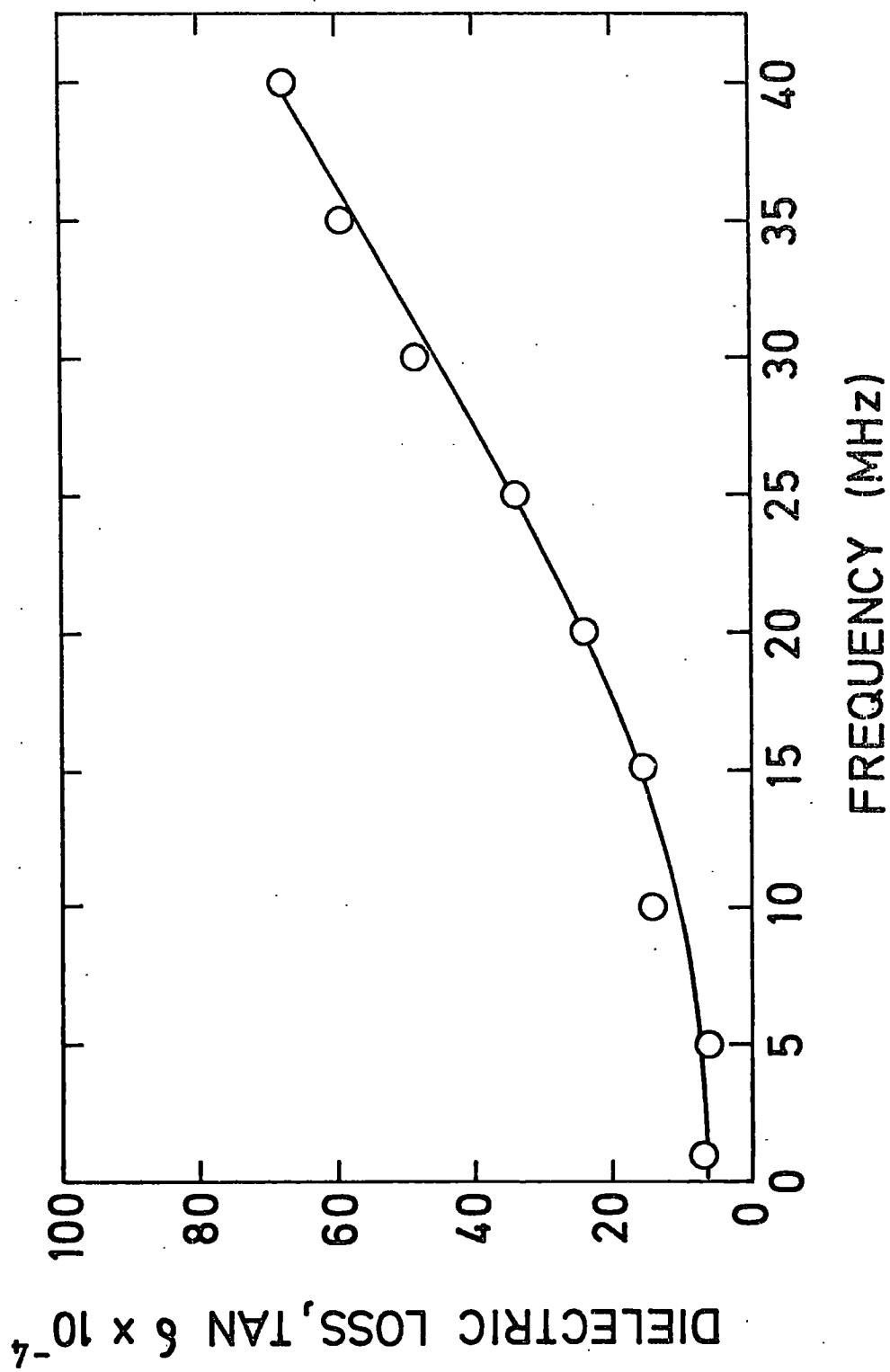


FIG. 2.4 Variation of dielectric loss,  $\tan \delta$ , with frequency for  $\text{Gd/CaWO}_4$ .

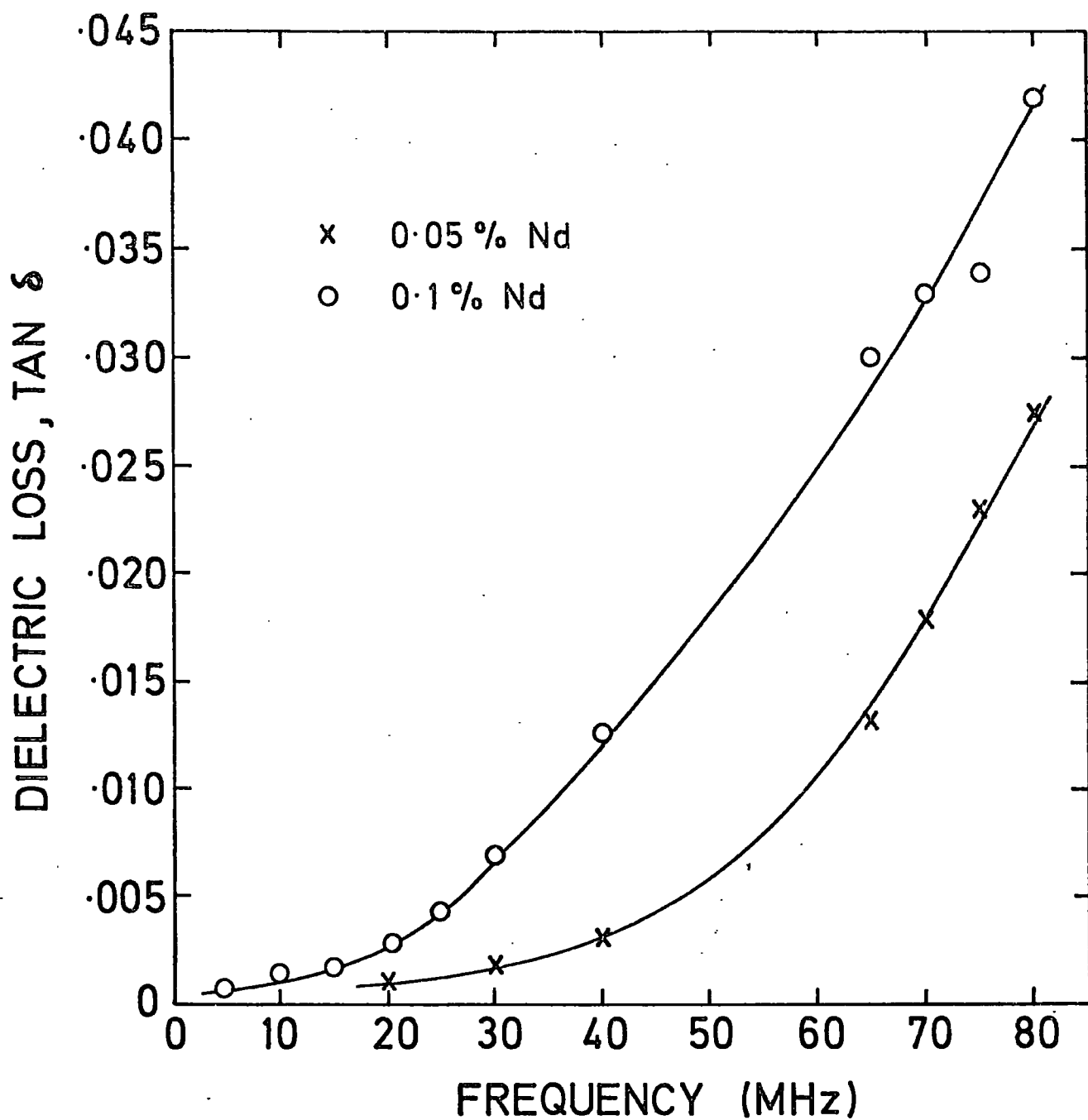


FIG.2.5 Variation of dielectric loss,  $\tan \delta$ , with frequency for  $\text{Nd/CaWO}_4$ .



reported here were made on vacancy compensated crystals, whereas those of Brower and Fang were made on sodium compensated crystals, so it appears that the dielectric constants are not very sensitive to differences in growth methods. The present work shows further that there is little increase in either  $\epsilon'_a$  or  $\epsilon'_c$  over the frequency range 1 to 40 MHz.

With regard to the dielectric constants of the doped single crystals, the results showed that doping with neodymium or gadolinium did not produce a measureable change in either  $\epsilon'_a$  or  $\epsilon'_c$ ; this conclusion was not unexpected as both the neodymium and gadolinium concentrations were low and electron spin resonance data reported by Brown et al, 1974 (7) and by Thorp et al, 1974 (8), had previously confirmed that the rare earth ions entered the tungstate lattice substitutionally and occupied calcium sites.

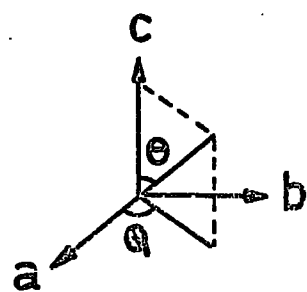
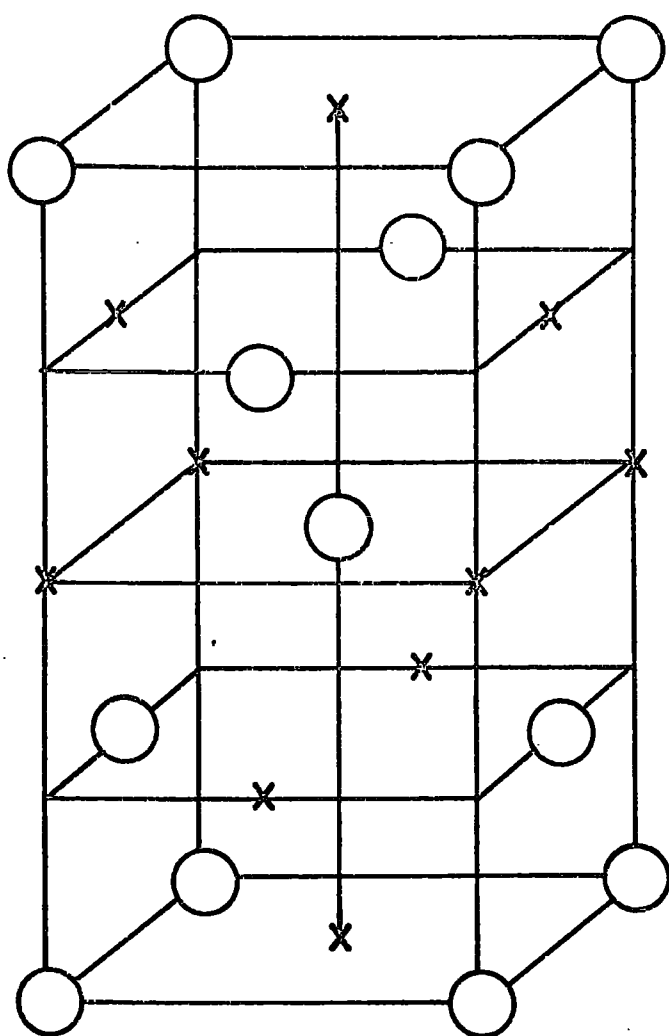
The dielectric loss data, on the other hand, established that in the neodymium calcium tungstate, the high frequency values of  $\tan \delta$  were concentration dependent. This effect may be associated with Debye relaxation of the neodymium ion, although this has not yet been proved. Experimentally, the loss measurement is a more sensitive detector of small composition changes than the dielectric constant measurement; this might be useful in an analytical context where the application of conventional methods, particularly for gadolinium, is difficult.

## CHAPTER 3

### SITE OCCUPATION BY GADOLINIUM IN CALCIUM TUNGSTATE

#### 3.1 The Crystal Structure

Calcium tungstate, 'scheelite', crystallizes in the tetragonal system (1) and has a space group  $C_{4h}^6$  ( $I4_1/a$ ) with four molecules to the unit cell (2). The lattice parameters are  $a = b = 5.243 \text{ \AA}$  and  $c = 11.376 \text{ \AA}$ . Figure 3.1 shows the unit cell with the oxygen atoms omitted for clarity. The unit cell may be divided into four horizontal (001) layers of equal stacking density. Arbel and Stokes (3) reported that cleavage and slip occur parallel to these layers in  $\text{CaWO}_4$ . Each calcium atom is surrounded by eight oxygen atoms at an average distance of  $2.46 \text{ \AA}$  in the shape of a distorted cube. The four calcium sites are equivalent in pairs, one pair being derived from the other by body centering about a calcium site as reflected in the (001) plane. This is shown in the projection of the eight oxygen atoms on the (001) plane through the calcium atom for the two sites, Figure 3.2. The tungsten atom is surrounded by four oxygen atoms in the same  $\text{WO}_4$  group as nearly ~~regular~~ <sup>perfect</sup> tetrahedral (4) with bonding distance  $1.784 \text{ \AA}$ . The site symmetry of both the Ca and W atoms in  $\text{CaWO}_4$  is  $S_4$ . The distorted cube of oxygen atoms surrounding the  $\text{Ca}^{2+}$  site is twisted at an angle of about  $9^\circ \pm 2^\circ$  from the unit cell a-axes in the (001) plane. These surrounding oxygens provide the framework of the crystal field symmetry at the  $\text{Ca}^{2+}$  site, the direction of which was first determined by Hempstead and Bowers (2) and was confirmed recently by Buckley (5). This property was used to identify the sense of the + z axis in  $\text{Gd/CaWO}_4$  crystals for alignment in ultrasonic experiments made by Farley (6).



$$a = b = 5.243 \text{ \AA}$$

$$c = 11.376 \text{ \AA}$$

FIG. 3.1 The unit cell of  $\text{CaWO}_4$  (Scheelite) with the oxygen atoms omitted for clarity.

- Calcium atom  
x Tungsten atom

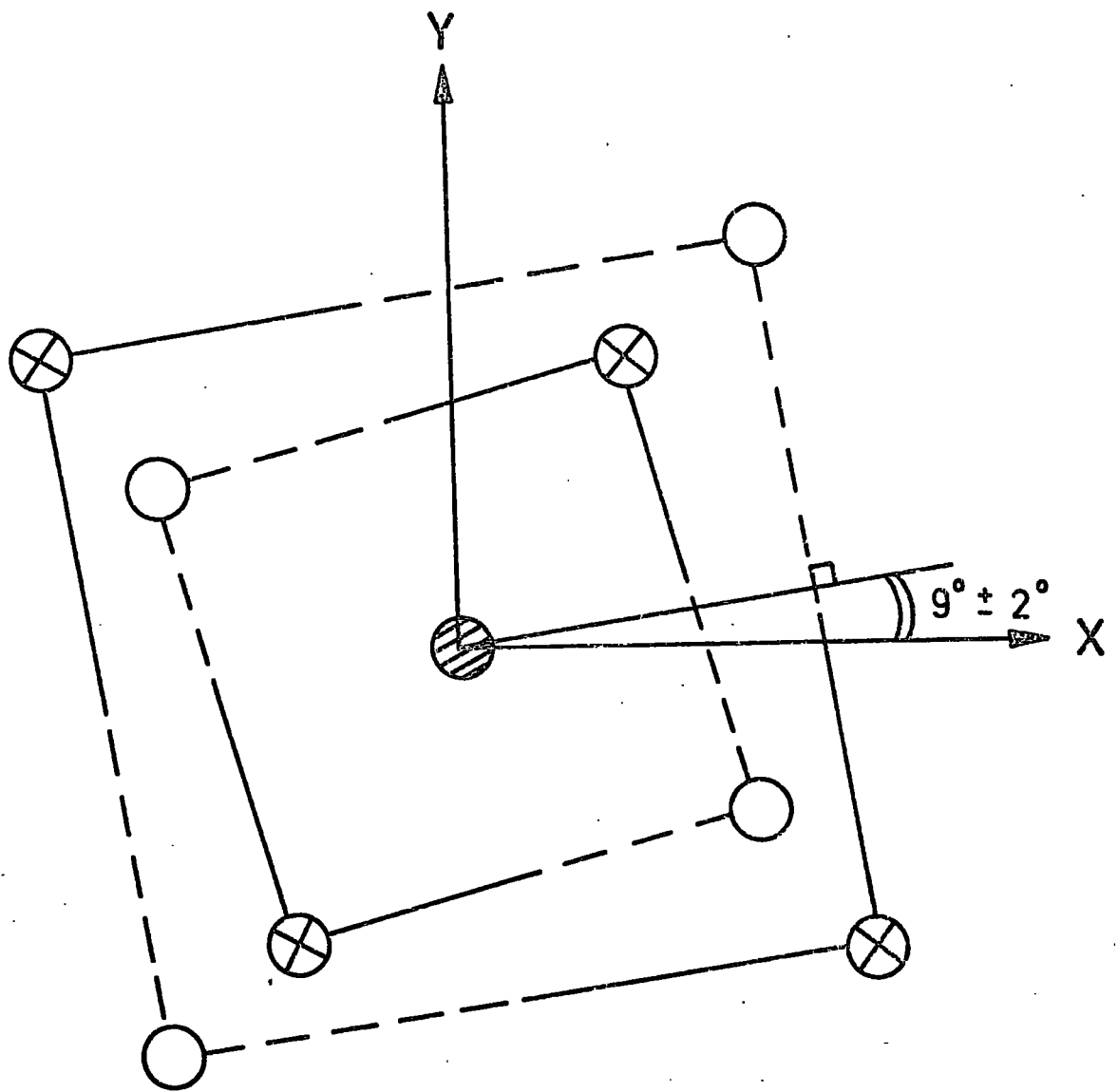





FIG. 3.2 A projection of the eight neighbouring oxygen atoms on the (001) plane through the calcium atom for the two sites which are related to each other by reflection in the plane of the paper.

-  Calcium atom
-  Oxygen atom above the plane of the paper
-  Oxygen atom below the plane of the paper

### 3.2 Crystal Growth

Single crystal boules of  $\text{CaWO}_4$  doped with Gd were grown by the Czochralski technique (7) by I.R.D. Ltd., Newcastle upon Tyne, with the c-direction along the growth axis. It had been reported by Nassau and Broyer (8) that the melting point was about  $1600^\circ\text{C}$  and this temperature was used for growth. Gadolinium was added in the form of the oxide  $\text{Gd}_2\text{O}_3$  to the powdered calcium tungstate. In pulling from the melt, trivalent rare earths can be incorporated without the presence of a univalent ion by vacancy compensation. As a rare earth ion, gadolinium substitutes at the calcium sites (8) giving rise to one calcium vacancy for each pair of gadolinium ions to maintain local charge neutrality. Alternatively  $\text{Na}^+$  or  $\text{Y}^{3+}$  might have been used for charge compensation, as well as other monovalent and trivalent ions; these two ions are especially convenient since they are not paramagnetic, are very close to the right size ( $\text{Ca}^{2+}$  radius is  $0.99 \text{ \AA}$ ,  $\text{Na}^+$  is  $0.94 \text{ \AA}$  and  $\text{Y}^{3+}$  is  $0.92 \text{ \AA}$ ), and have suitably low volatilities. However, all the specimens used here were vacancy compensated. The nominal doping levels used were 0.005, 0.01 and 0.05 atomic per cent, although independent analysis (by the Analytical Services Laboratory, Imperial College) showed that the actual levels were all less than about 100 p.p.m. This concentration level is well below that at which substitution at W sites has been reported by Kedzie and Kestigian (9). The very compact nature of the structure of  $\text{CaWO}_4$  makes the interstitial sites very unlikely. Thus, in the material examined the strongest probability is that the gadolinium would have entered the lattice substitutionally at calcium sites.

### 3.3 The Energy Levels of $\text{Gd}^{3+}$ in $\text{CaWO}_4$

The trivalent gadolinium ion has seven unpaired electrons in

the 4f unfilled shell which make it half-filled and give rise to a ground state  $(4f^7)^8 S_{7/2}$ . In a host lattice the gadolinium ions will be subjected to a crystal field whose symmetry and order of magnitude depends largely on the surrounding environment. As an S-state ion gadolinium should exhibit no first order crystal field splitting, a feature discussed by Bleaney and Stevens (10). However, the ESR experiments have shown that small splittings do exist. The magnitudes of the initial splittings of  $Gd^{3+}$  ions in crystals of the scheelite series were reported by Vinokurov et al (11). They gave crystal field splitting constants  $b_2^0$  for  $Gd/CaWO_4$  at 77 K and 290 K as  $916.7 \times 10^{-4} \text{ cm}^{-1}$  and  $892.4 \times 10^{-4} \text{ cm}^{-1}$  respectively. This is in exact agreement with the value of  $b_2^0$  at 77 K given by Hempstead and Bowers. It was also shown that all the  $b_n^0$  values decrease on passing from  $CaWO_4$  to  $BaMoO_4$  in the scheelite series. This is because of the regular increase in the unit cell constants (a and c) with increase in the ionic radius of the corresponding cation. Consequently, the Gd-O distance in  $GdO_8$  complex will increase in an unchanged local field symmetry which leads to a fall in the strength of the electric field and thus amounts to a decrease in the  $b_n^0$  constants (11,12).

Van Vleck and Penney in 1934 (13) found that for an S-state ion to exhibit splitting of the energy levels, it is necessary to go to a high order perturbation of the crystal field applied to direct spin-orbit interactions. But, Abragam and Pryce in 1951 (14) concluded that these splittings were in fact too big to be explained by the above process. They suggested instead that they are due to a spin-spin interaction which also couples orbits with spins, since it depends on position variables. Their idea was that in the crystal field, even though the ion is in an S-state, there will be some

distortion of the orbits. This is supposing that instead of the charge cloud being a perfect sphere it is slightly ellipsoidal. Then the dipole-dipole energy of the spins varies with their orientation with respect to the axes of the ellipsoid, and thus the eigenvalues depend on the spin orientation. They were able to put forward convincing arguments that this is indeed the correct mechanism. So, in the tetragonal field of calcium tungstate the  $J = 7/2$  state splits into four Kramers' doublets and paramagnetic resonance then occurs between the Zeeman levels of these four doublets. The energy level diagram for  $Gd^{3+}$  in calcium tungstate at Q-band was drawn by Buckley (5) using straight line extrapolation from that predicted by Harvey and Kiefte in 1971 (15) at X-band frequencies. A convincing fit in Buckley's ESR results and several others, especially those of Dernov-Pegarev et al (16) for  $Gd/CaMoO_4$ , was attained. The ESR spectrum of only seven lines for  $M = 1$  transitions, which was observed by Thorp et al (1974) in their study of dipolar broadening mechanism in  $Gd^{3+}/CaWO_4$ , gives a further evidence for  $Gd^{3+}$  substitution at  $Ca^{2+}$  sites in a tetragonal symmetry (17).

### 3.4 The Spin-Hamiltonian

A spin Hamiltonian containing relatively few terms will give a complete description of the experimental data when given the right size of the coefficients of these terms together with the directions of the appropriate axes relative to the crystal axes where anisotropy is present. The most general form of the spin Hamiltonian contains terms representing the Zeeman interaction of the magnetic electrons with an external field, level splittings due to indirect effects of the crystal field; usually referred to as 'fine structure', hyperfine

structure due to the presence of nuclear magnetic dipoles, quadrupole moments in the central ion or in the ligand ions, and the Zeeman interaction of the nuclear moments with the external field. In general, the spin Hamiltonian can be represented by

$$H = g \beta H \cdot S + D \left[ S_z^2 - S(S+1) \right] + E (S_x^2 - S_y^2) . \quad (3.1)$$

The first term gives the interaction with the applied magnetic field and the other two terms arise from crystal field effects. Further terms must be added if the ion possesses a resultant nuclear magnetic moment.

Knowing the structure of  $\text{CaWO}_4$  crystal and the symmetries of the  $\text{CaO}_8$ , Hempstead (2), Vinokurov (11) and Kurkin (12) published the spin Hamiltonian for  $\text{Gd/CaWO}_4$  as

$$H = g_{\parallel} \beta H_z S_z + g_{\perp} \beta (H_x S_x + H_y S_y) + \frac{1}{3} b_2^0 O_2^0 + \frac{1}{60} (b_4^0 O_4^0 + b_4^4 O_4^4) + \frac{1}{1260} (b_6^0 O_6^0 + b_6^4 O_6^4) , \quad (3.2)$$

where  $z$  is in the  $c$ -axis of the crystal and  $S = 7/2$ . To simplify this expression the constants were re-written as

$$\begin{aligned} b_2^0 / B_2^0 &= 3 \\ b_4^0 / B_4^0 &= b_4^4 / B_4^4 = b_6^4 / B_6^4 = 60 \\ b_6^0 / B_6^0 &= 1260 \end{aligned} \quad (3.3)$$

and then, the spin Hamiltonian reduced to



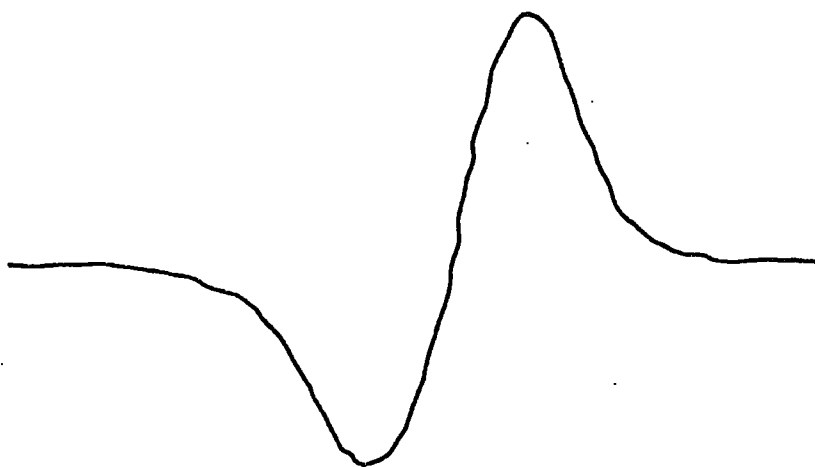
$$H = g_{\parallel} \beta H_z S_z + g_{\perp} \beta (H_x S_x + H_y S_y) + B_2^0 O_2^0 + B_4^0 O_4^0 + B_4^4 O_4^4 + B_6^0 O_6^0 + B_6^4 O_6^4 \quad (3.4)$$

where each  $O_n^m$  is an operator function having the same transformation properties as the corresponding spherical harmonic  $Y_n^m$ , and the coefficients  $B_n^m$  are parameters to be determined by the experiment. The parameters  $g_{\parallel}$ ,  $g_{\perp}$ ,  $b_2^0$ ,  $b_4^0$ ,  $b_4^4$ ,  $b_6^0$ , and  $b_6^4$  can effectively be determined from the measurements of the gadolinium transitions with the magnetic field  $H$  parallel to the  $c$ -axis of the crystal (i.e.  $\theta = 0^\circ$ ) and with  $H$  perpendicular to the  $c$ -axis (i.e.  $\theta = 90^\circ$ ). It is noticed that for  $Gd^{3+}$ , as well as for  $Mn^{2+}$  (2) the arrangement of the eight oxygen atoms surrounding the dopant ion, (or the  $Ca^{2+}$  sites), gives  $b_4^4 \approx 10 b_4^0$  which differs from that of a cubic environment where normally  $b_4^4 = 5 b_4^0$ . This conclusion is in agreement with Wyckoff's discussion of the crystal structure referred to in Section 3.1.

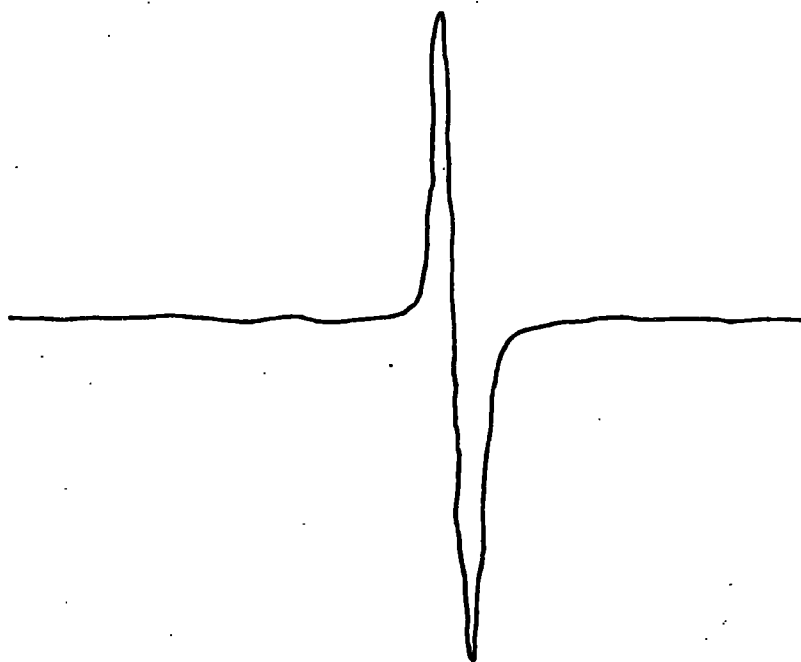
### 3.5 Experimental observations of ESR spectra of gadolinium in calcium tungstate

When discussing the crystal structure of  $CaWO_4$  in Section 3.1, it was shown that all four possible positions of the  $Ca^{2+}$  in the unit cell possess a local crystal field symmetry of  $S_4$  and are magnetically equivalent. This leads to the same single spectrum for each paramagnetic ion introduced into the host lattice. The ESR spectrum of  $^{87}Gd_{7/2}$  in  $CaWO_4$  single crystals was reported by Hempstead and Bowers (2) as consisting of seven widely spaced strong lines due to  $\Delta M = \pm 1$  and a number of weaker transitions corresponding to  $\Delta M = \pm 2$ , (such

transitions are to be expected as  $b_2^0$  is so large as to be comparable with  $g\beta H$ ). They also observed that other weak lines flanked the strong ones which represent the hfs due to the odd Gd isotopes ( $Gd^{155}$  14.7% abundance;  $Gd^{157}$  15.7%). Both isotopes have nuclear spin  $I = 3/2$  and each hfs component has only about 5% of the intensity of the main line. Here, we will regard the  $\Delta M = \pm 1$  transitions due to the even isotopes as "clean" lines. A clean line is defined as one characteristic of tetragonal symmetry, appearing as a symmetrical, well-balanced signal on a derivative output. Such a spectrum is obtained with the 0.005% Gd sample, and one of the transitions, observed with the magnetic field  $H$  parallel to the crystallographic  $a$ -axis in the (001) plane (i.e. with  $\theta = 90^\circ$  and  $\phi = 0^\circ$ ), is reproduced in Figure 3.3. The line is "clean" and the transition remains single at room temperature, 77 K and 4.2 K. This form of lineshape is also observed for all the Gd transitions over a wide range of angles  $\phi$  except near  $\phi = 55^\circ$ . Near this angle some distortion in line shape is observed. This distortion becomes more pronounced as we lower the temperature of the sample where the distortion seems to be "splitting" in each transition. These effects are illustrated by the spectra shown in Figures 3.4, 3.5 and 3.6. The splitting effect was first observed in the first quadrant (i.e. in the  $\phi$ -plane with  $0 < \phi < 90^\circ$ , and  $+z$  axis is upwards perpendicular to the plane of observation); measurements were extended to the other quadrants and it was found that the splittings are very much more pronounced in the first and third quadrants than in the second and fourth. With the higher concentration sample (0.05% Gd) the splitting was observed over a much wider range of angles  $\phi$ , as was reported by Buckley (5). This is shown in Figure 3.7.



(a)  $\phi = 0^\circ$ , TEMP = 77K



(b)  $\phi = 0^\circ$ , TEMP = 4.2K

FIG.3-3 A "clean" single transition.

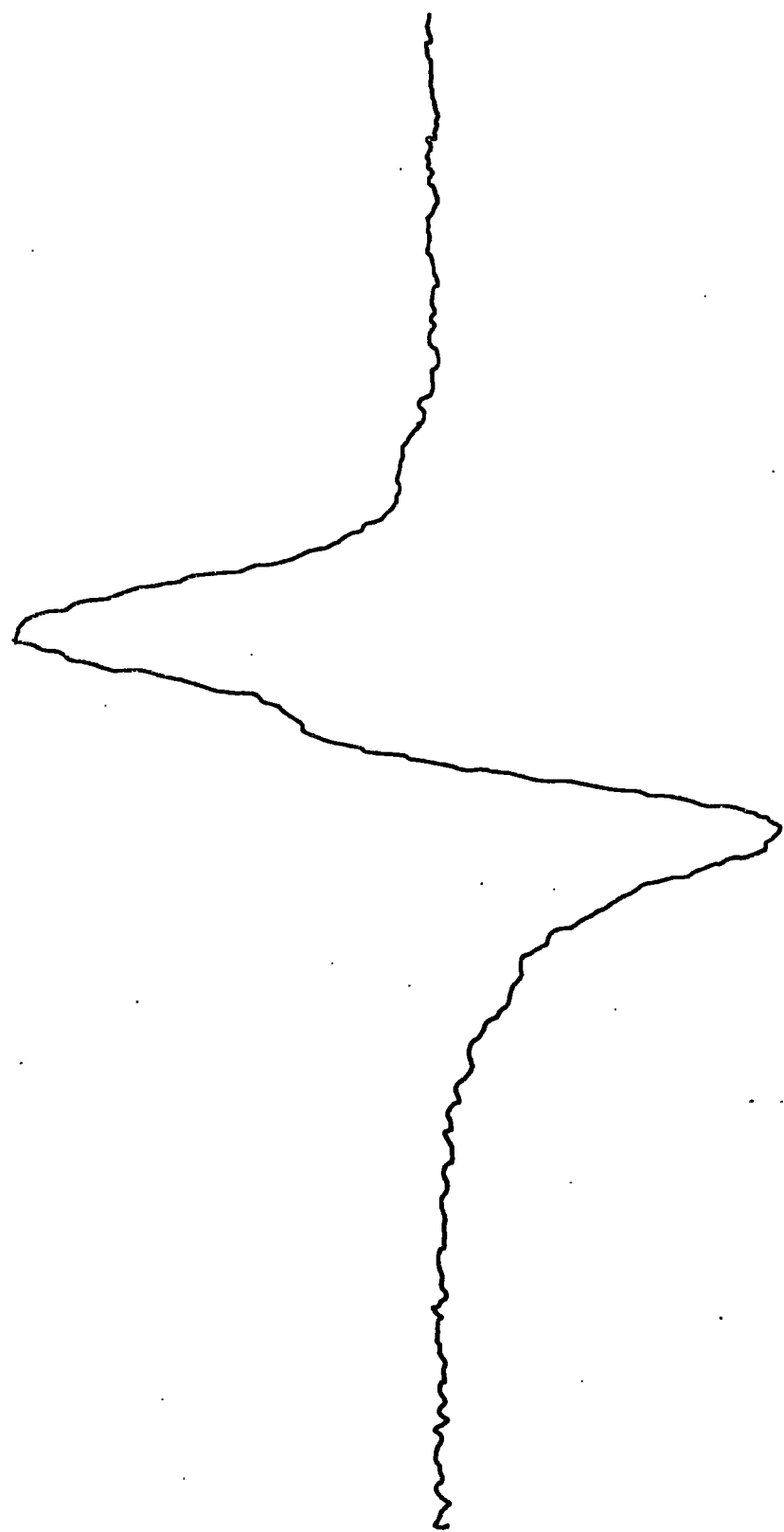


FIG.3.4 A transition at  $\varphi = 55^\circ$  and 293K (0.005% Gd)

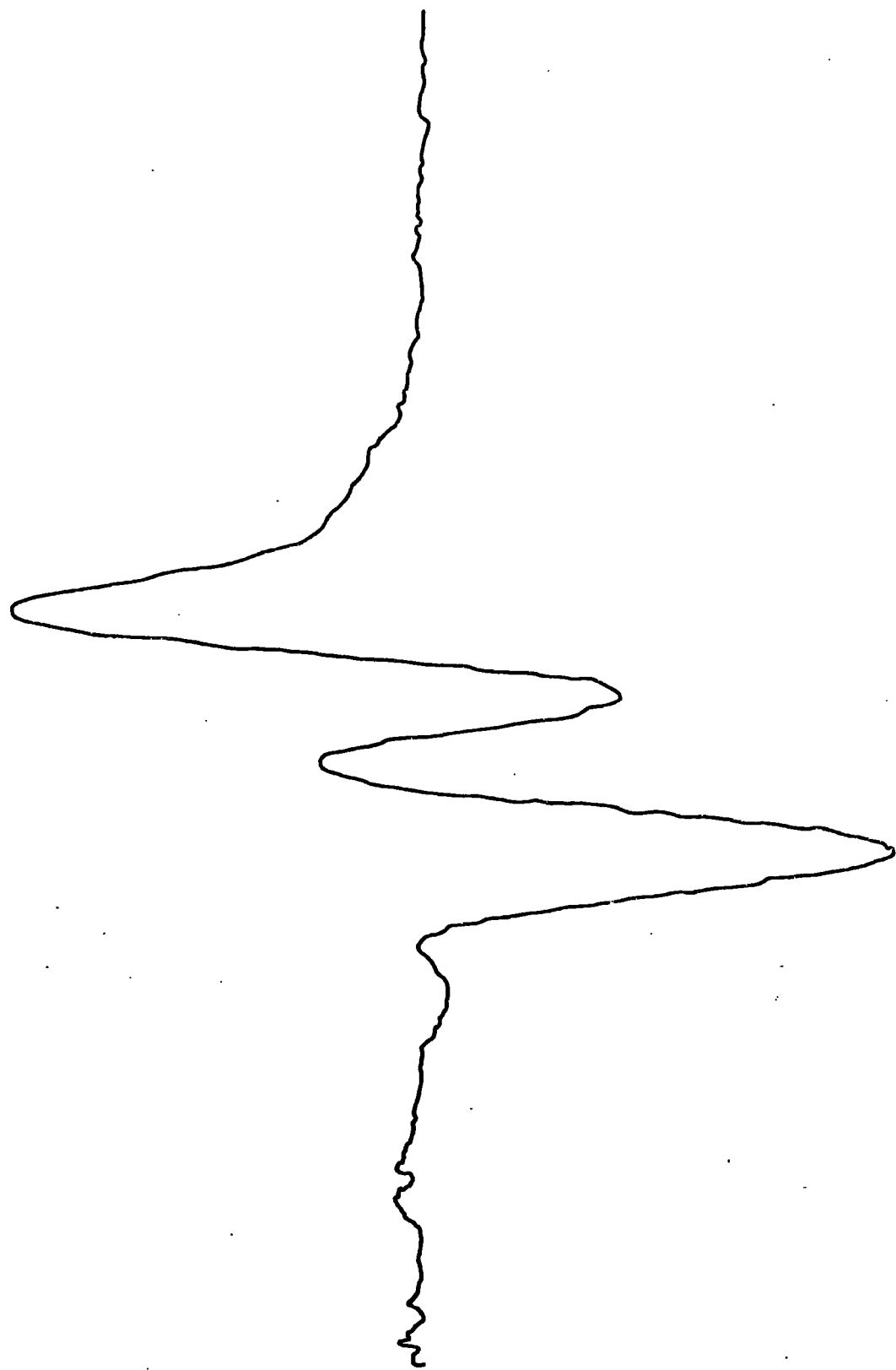


FIG.3.5 The same transition at  $\varphi = 55^\circ$  and 77K (0.005 % Gd)

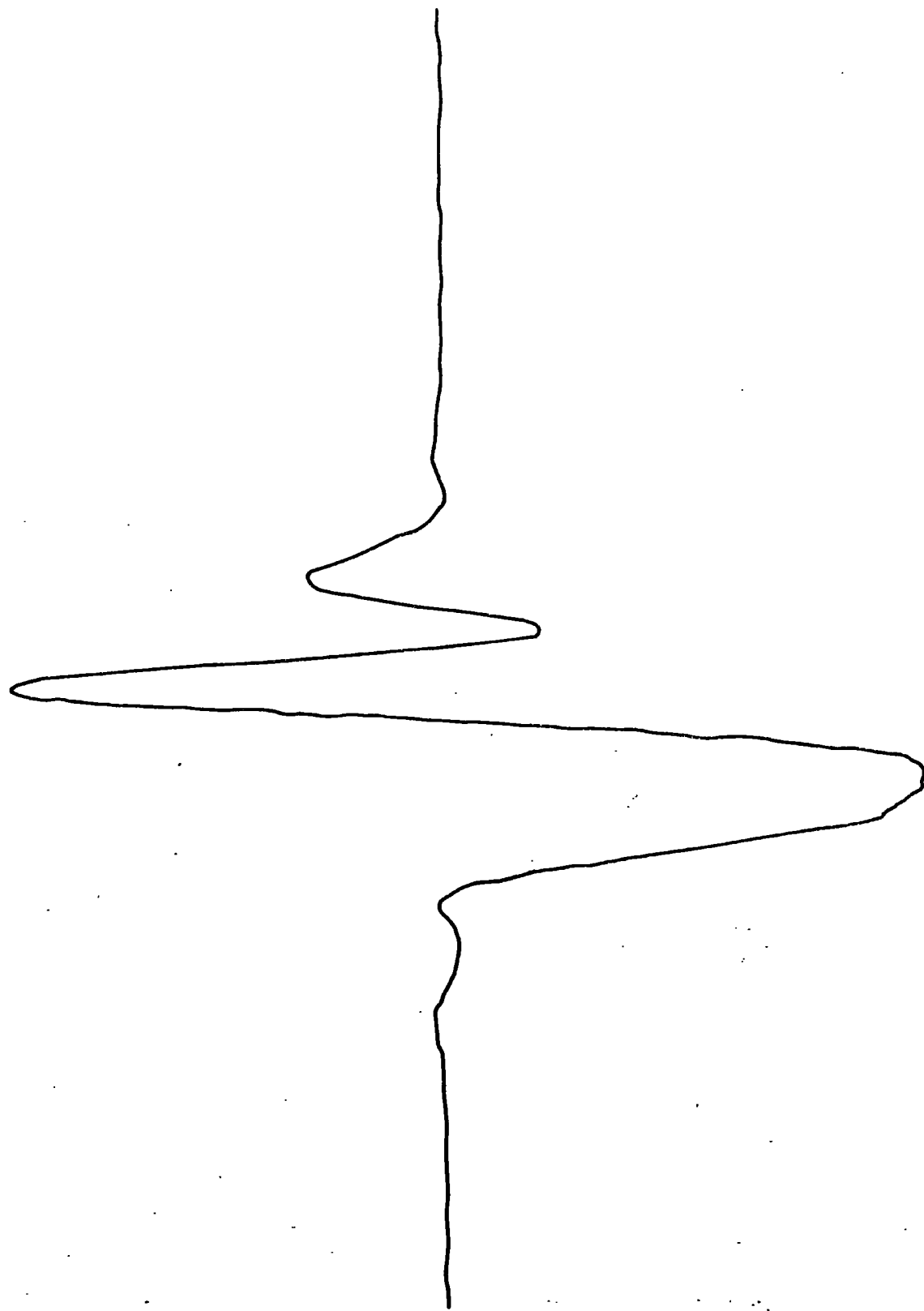


FIG.3.6 The same transition at  $\varphi=55^\circ$  and 4.2K (0.005% Gd)

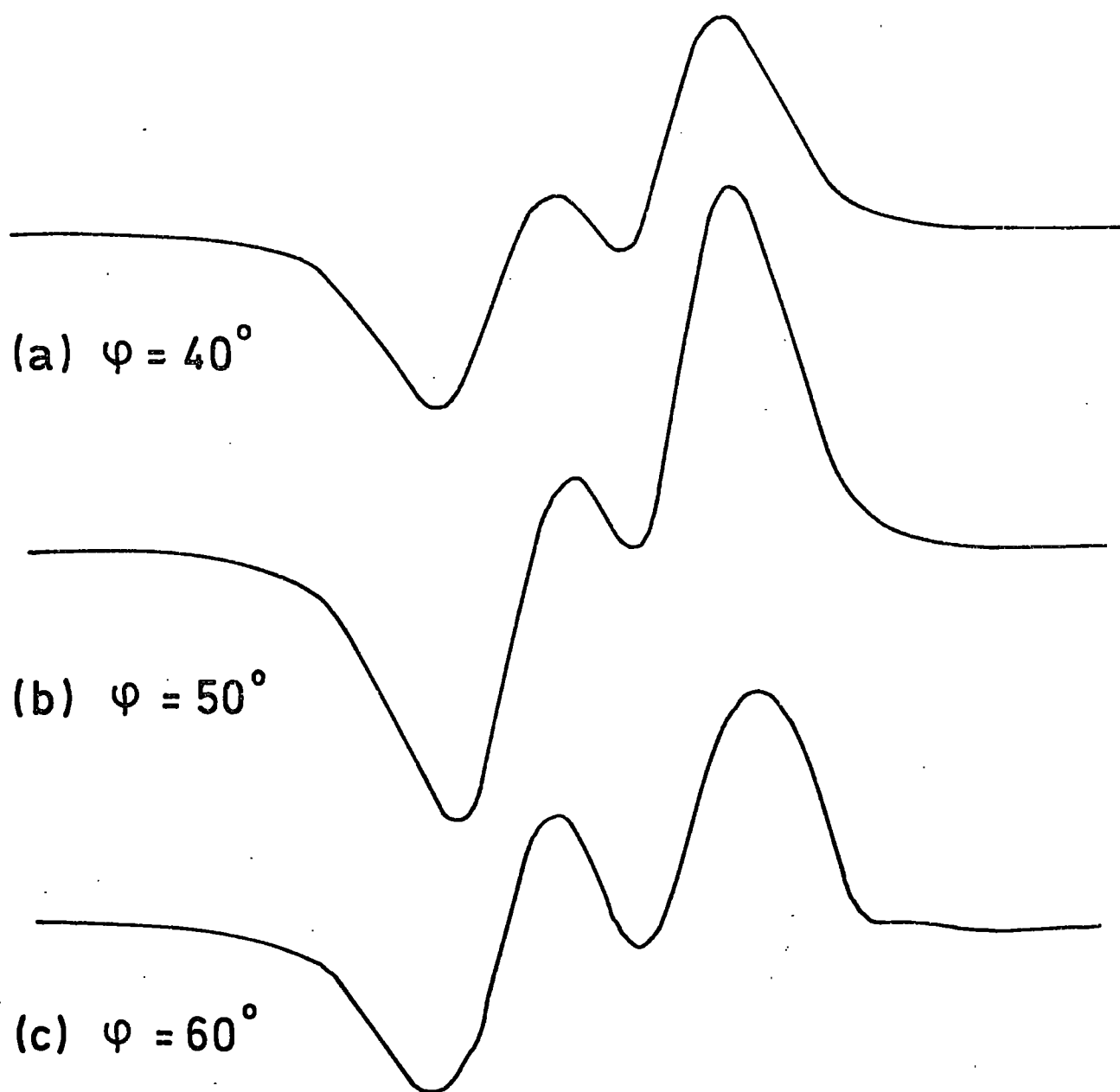


FIG. 3.7 Splitting observed with 0.05% Gd sample over a wider range of angles  $\psi$ .

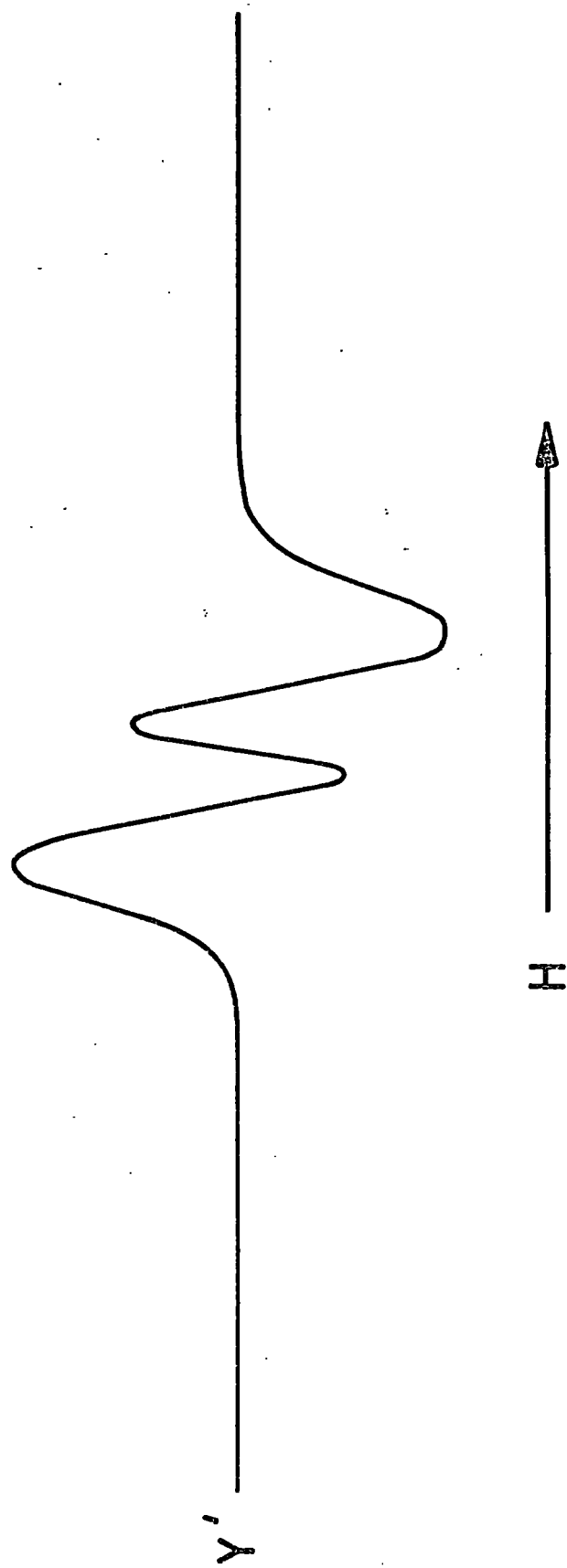


FIG. 3-8 The derivative of an ESR transition for  $\chi$ -irradiated glycylglycine, reported by Randolph (18)



### 3.6 Comparison with the previous ESR data

The aim of this chapter, as was mentioned earlier in Chapter 1, is to investigate the cause and nature of the splitting in the Gd main transitions observed by Buckley (5) and confirmed by our results. That is one of the reasons why we used the same samples of reference (5) in our studies. It is interesting to show that the shapes of the derivatives presented here as Figures 4 - 7 are due to genuine effects and they are not, for example, due to lack in balancing the spectrometer. This could be shown by comparison with Figure 3.8 which shows the derivative of the ESR curve of about  $10^{18}$  resonant centres produced by  $\text{Co}^{60}$  gamma irradiation of glycylglycine reported by Randolph in 1960 (18). However, it could not be a matter of unbalance in the signal for Figure 3.3 shows that a quite good balance could be attained in any case. Several workers have studied the ESR spectra of the rare earth ions in the Scheelite series and we could find the following features in their investigations as described in the next section.

#### 3.6.1 'Anomalous' transitions of trivalent rare earth ions in scheelites

By 'anomalous' transitions we mean any transition other than the normal electronic transitions for which  $\Delta M = \pm 1$  in the ESR spectra of rare earth ions in scheelites having an undistorted tetragonal symmetry. Four kinds of anomalies could be established from the previous published work.

(a) Transitions due to the various compensation mechanisms for the excess charge, which arises from doping the host scheelites with trivalent rare earth ions, to achieve charge neutrality. The published

ESR data indicated the presence of centres of lower symmetry in addition to tetragonal centres. Three nontetragonal centres in the  $\text{Er}^{3+}$  doped samples and two such centres in the  $\text{Th}^{3+}$  doped crystals were reported by Abdulsabirov et al in 1972 (19). These authors concluded that all the published information on the nontetragonal  $\text{Ce}^{3+}$  by Mims-Gillen (20), Volterra-Bronstein-Rockni (21),  $\text{Nd}^{3+}$  by Garrett-Merritt (22), (21), and  $\text{Yb}^{3+}$  by Ranon-Volterra (23) and their data on the nontetragonal  $\text{Th}^{3+}$  centres in  $\text{CaWO}_4$  can all be interpreted on the assumption that the compensating defects are located in one of three positions denoted by I, II, III in the crystal, Figure 3.9. The 'strongest' nontetragonal centres are formed when a compensating defect, an  $\text{Na}^+$  ion or a  $\text{Ca}^{2+}$  vacancy for crystals grown with and without sodium compensation respectively is located at the  $\text{Ca}^{2+}$  site nearest to the trivalent ion (position I in Figure 3.9). We also notice that these additional nontetragonal centres have different parameters and g-values, in other words, they would appear in the ESR spectra at different field positions from those of the normal tetragonal transitions.

(b) As Kedzie and Kestigian reported (9), substitution would occur at  $\text{W}^{6+}$  sites as well as  $\text{Ca}^{2+}$  sites with and without adding  $\text{Na}^+$  ions for charge compensation. A spectrum of five main lines (plus smaller lines due to hyperfine structure) was observed for  $\text{Nd}^{3+}/\text{CaWO}_4$  crystals. The central line of the five transitions was the most intense and was attributed to  $\text{Nd}^{3+}$  in the Ca site, while the four remaining lines were thought to be due to  $\text{Nd}^{3+}$  ions in a W site. Although Garrett and Merritt (22) and Ranon and Volterra (23) found that the chemical evidence argues strongly for the substitution of  $\text{Nd}^{3+}$  in Ca sites, we still regard substitution of rare earth ions in W sites as a source for anomalous transitions. In fact, substitution in W sites, whenever it occurs, will give

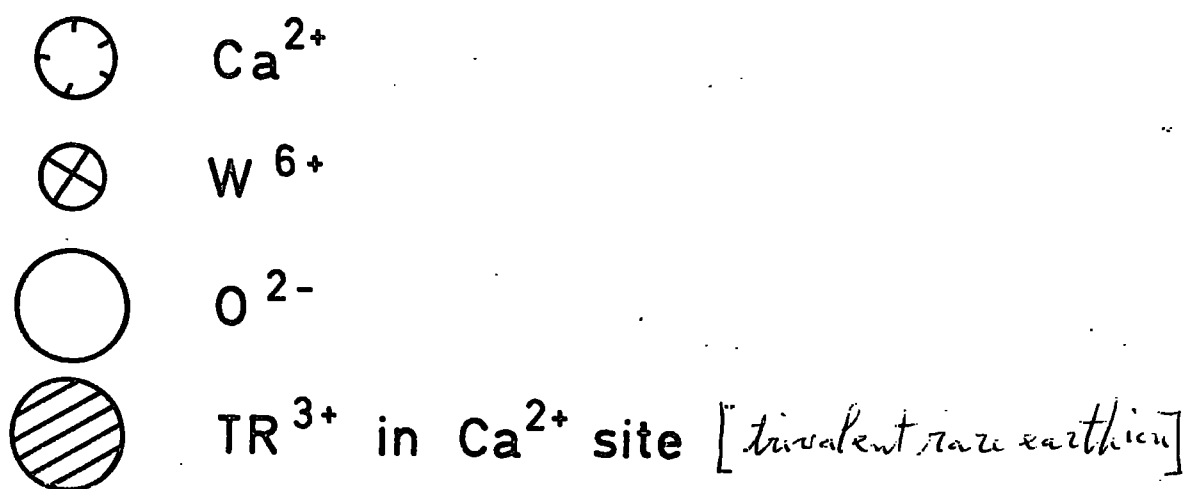
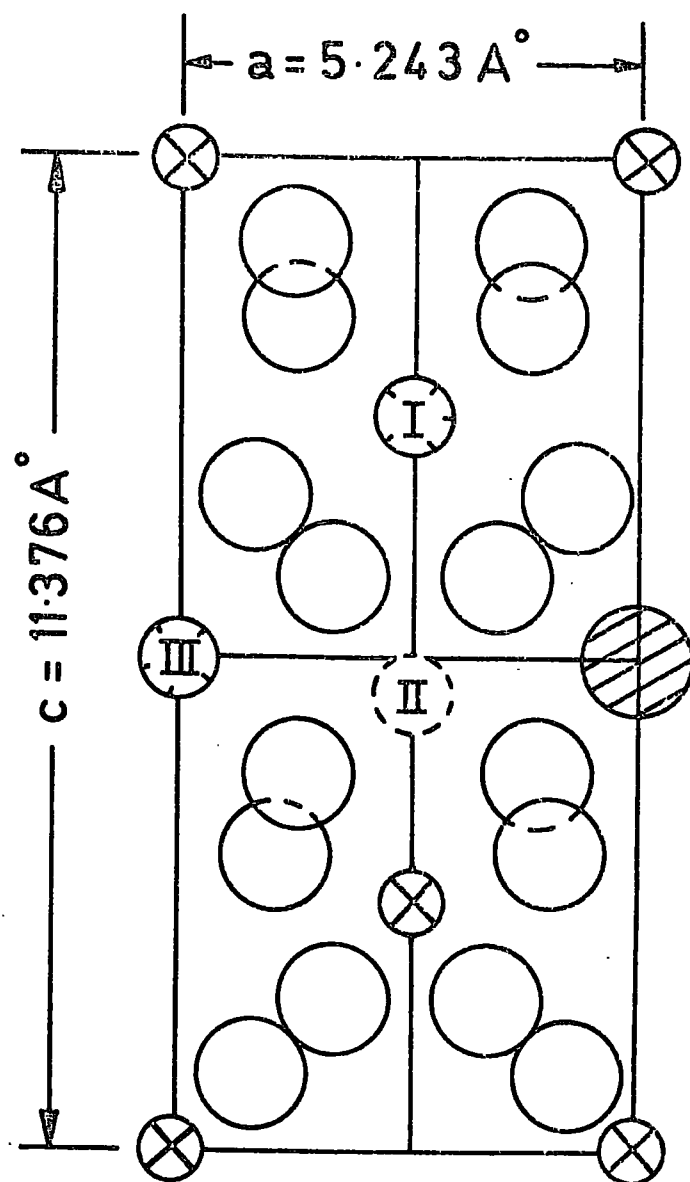


FIG. 3.9 Projection onto the  $a$ - $c$  plane of  $\text{CaWO}_4$  unit cell. I, II and III are positions of the compensating defects in nontetragonal centres.

a distinguishable ESR spectra from that due to ions substituting in Ca sites because of the different environment for each site.

(c) A third kind of transition could be observed as weaker transitions corresponding to  $\Delta M = \pm 2$  (known as forbidden transitions). These lines are to be expected whenever  $b_2^0$  is so large as to be comparable with  $g\beta H$ , as reported by Hempstead and Bowers in 1960 for  $Gd^{3+}$  in  $CaWO_4$  crystals (2).

(d) Hyperfine transitions, due to the odd isotopes, if present, having a net nuclear spin  $I$ , give a hfs of low intensity compared to the main transitions. Examples of these effects could be demonstrated by the spectra of  $Gd^{3+}/CaWO_4$  (2),  $Nd^{3+}/CaWO_4$  (9,22) and  $Yb^{3+}/CaWO_4$  (23).

From the above classification we see that none of the four mentioned causes can be the reason for the splitting reported here in our results; Section 3.5. This, therefore, must be classified as a separate kind of anomaly. The only previous work in which a fairly close similarity of behaviour existed was that of Forrester and Hempstead (24) who observed unresolved doublets in the ESR spectra of  $Tb^{3+}/CaWO_4$  single crystals, and suggested that this might be due to non-equivalence of the  $Ca^{2+}$  sites. Their observations, as far as splitting is concerned, are as follows. As they increased the angle  $\theta$  between the applied magnetic field and the c-axis of the crystal the lines were broadened. At K band (23 GHz) and a temperature of 4.2 K, the linewidth increased from 1.4 gauss when  $\theta = 0^\circ$ , to about 15 gauss when  $\theta = 60^\circ$ . The line shape was distorted as  $\theta$  was further increased, the peaks became somewhat flattened and at angles greater than about  $70^\circ$  the lines became partially resolved into doublets. The highest field transition was better resolved than the lowest field line. And, finally, they interpreted this behaviour as indicating that the two types of Ca site are not completely equivalent.

### 3.7 Interpretation of present results

We attempted to resolve our derivative curves into separate absorption peaks in order to get more information about the 'extra component'. This was done by integrating  $\int y dx$ , where  $y$  is the ordinate of the derivative curve and  $dx$  is a small, arbitrary, increment of magnetic field. The results depicted in Figures 3.10 and 3.11 show the calculated absorption curves for the derivatives in Figures 3.6 and 3.5, respectively. It is unfortunate that we could not get significant information about the separation of the absorption peaks or their intensities for they are, in most cases, unresolved. However, from our experimental data we have two important features which might serve as clues to a correct interpretation.

- (i) The occurrence of splitting at specific angles in the  $\phi$ -plane; this should draw the attention to the unit cell structure to inspect the crystal at these angles.
- (ii) The relative increase in the signal of the 'extra component' compared with the main transition as we reduce the temperature from 290 K to 4.2 K, which indicates that the dependence on temperature for the two components is not exactly similar.

Thus, to solve this problem two possibilities arise:-

- (a) We suggest that some of the  $Gd^{3+}$  ions may have slightly defected sites which would not disturb the crystal field symmetry radically in their vicinity, but cause the transitions to shift slightly on the field axis. If we examine the unit cell of  $CaWO_4$  we see in the (001) plane; ( $\phi$  plane), Figure 3.12 as reported by Farley, Saunders and Chung (25), that the nearest neighbours to a Ca site at an angle  $\phi$  about  $50^\circ$  are

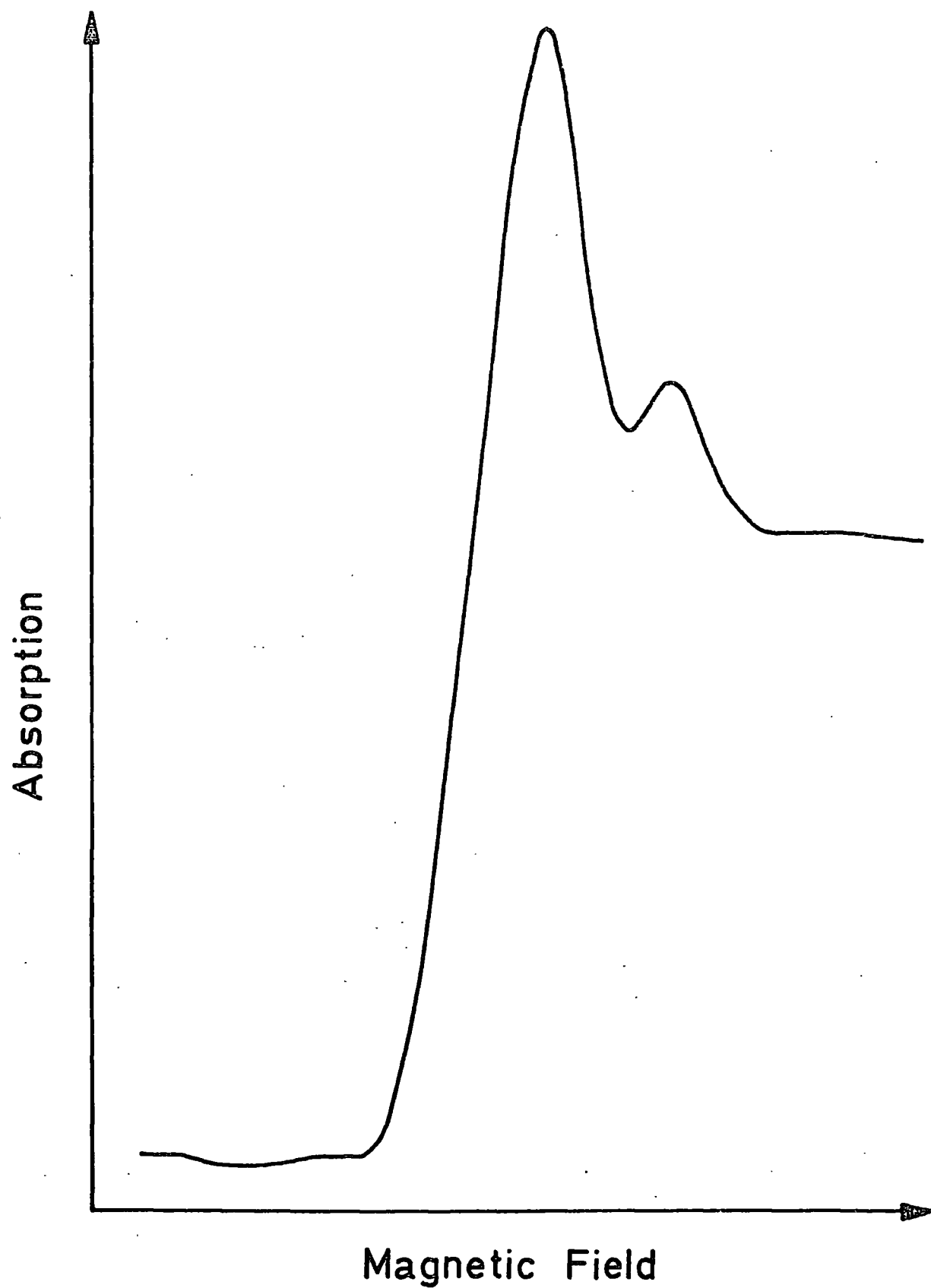


FIG. 3-10 ESR absorption curve calculated from the derivative shape in Fig. 3-6

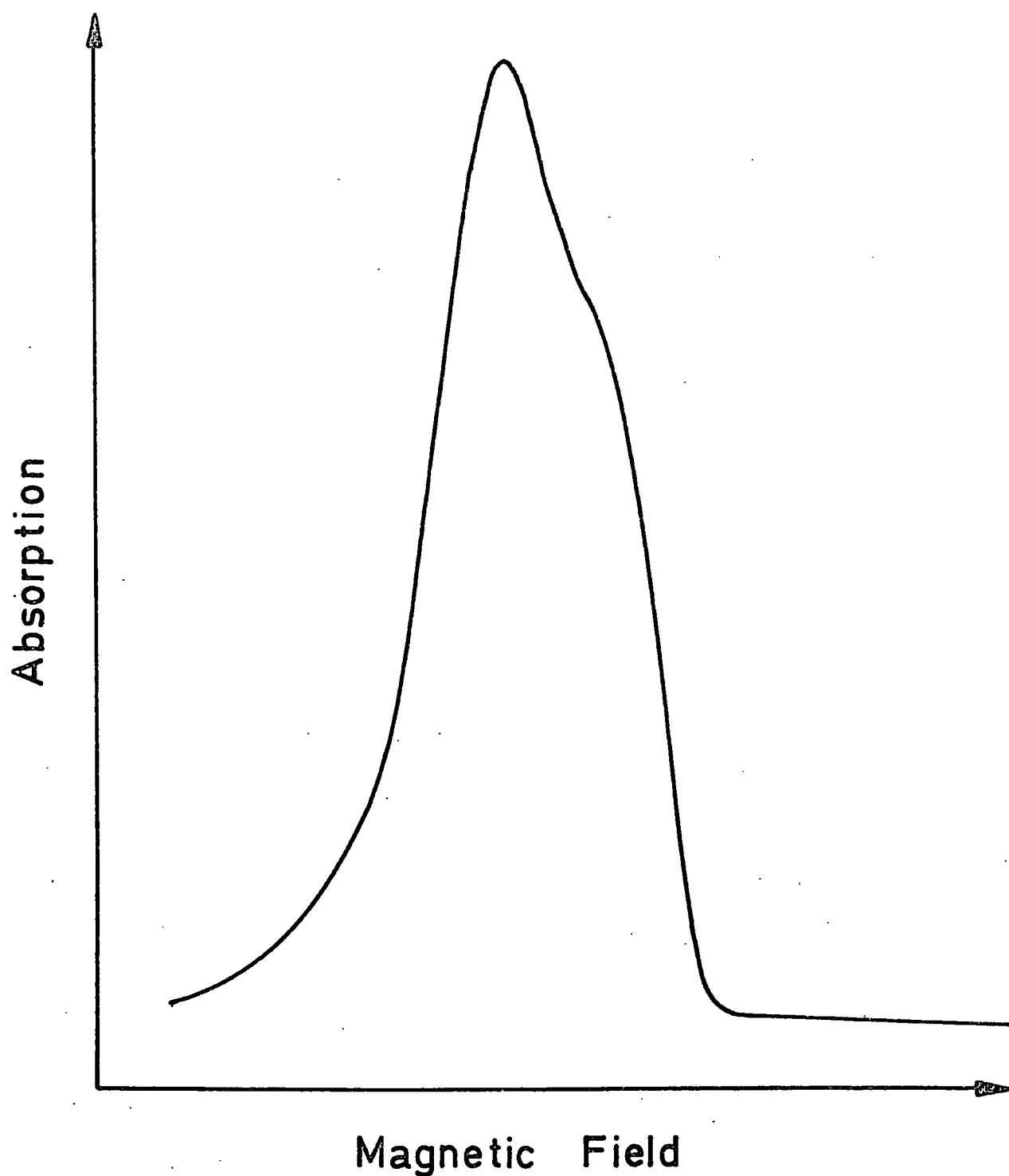
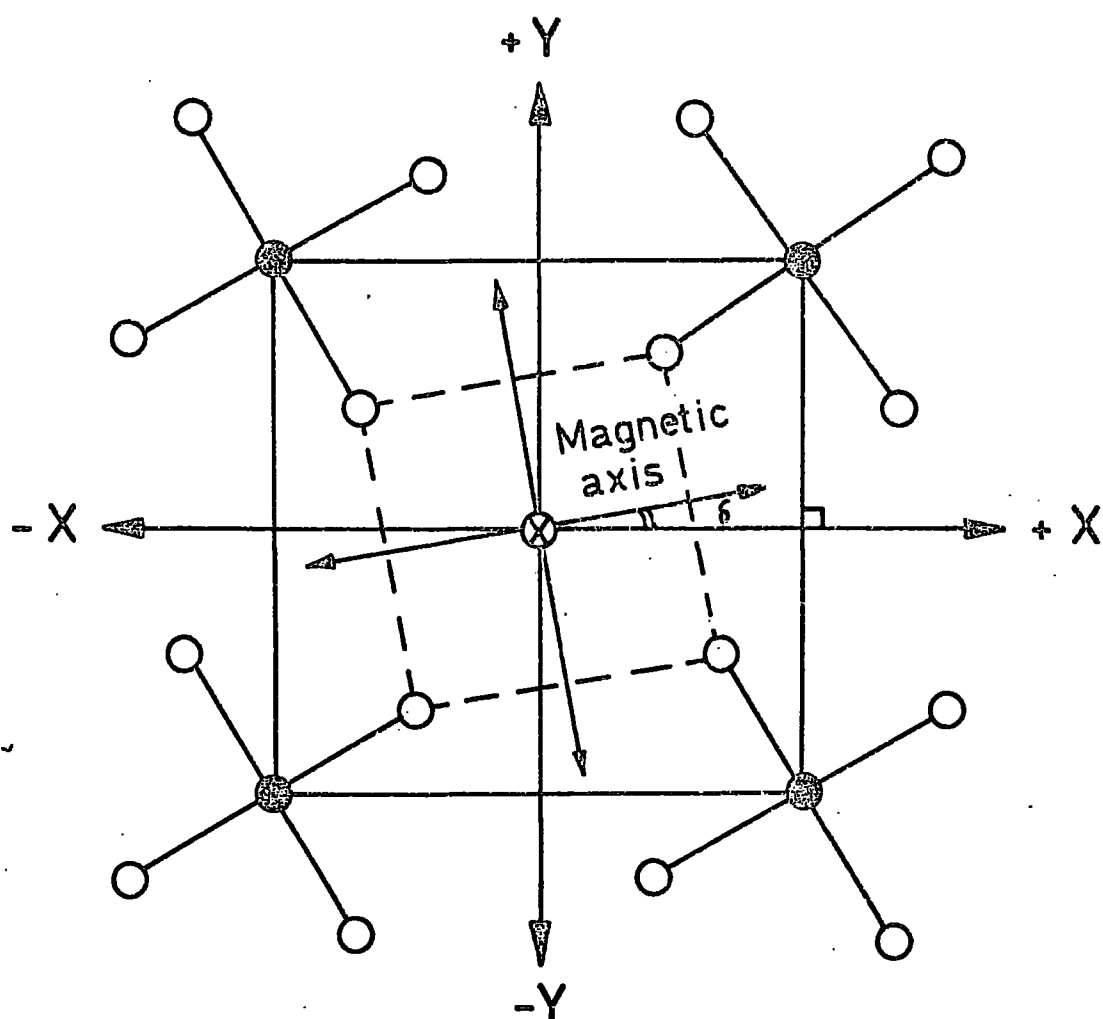


FIG. 3.11 ESR absorption curve calculated from the dervative shape in Fig. 3.5



- Oxygen sites
- Tungsten sites
- ⊗ Calcium site

FIG. 3.12 Projection onto the (001) plane of the scheelite structure unit cell. The conventional +Z axis emerges from the plane of paper,  $\delta$  is the angle between the crystal axis and the magnetic axis.



oxygen ions. Knowing that the oxygen ions provide the framework of the crystal field symmetry at the Ca site we should expect some change in crystal field due to oxygen vacancies. In effect, we propose an ordered oxygen vacancy model. By this model we can also understand the behaviour of the "extra component" with temperature. As we reduce the temperature the possibility for these oxygen vacancies to settle in an ordered form increases and this leads to a corresponding increase in the signal from the  $Gd^{3+}$  ions in defected sites. This may explain the relative increase in the signal of the "extra component" as the temperature decreases.

(b) Another possibility lies in the interpretation of Forrester and Hempstead (24) of their results on  $Tb^{3+}$  in  $CaWO_4$ , which is mentioned above in Section 3.6.1. Consequently, we may conclude that the distortion of the  $Gd^{3+}$  in  $CaWO_4$  which we are reporting is probably an indication that the two types of Ca sites are not completely equivalent.

In fact, we favour very much the first suggestion which needs still more experimental work to test its validity. The second probability, however, could be excluded because it is a very well established fact that the four possible positions of Ca sites in the unit cell of  $CaWO_4$  when substituted by paramagnetic ions, lead to identical paramagnetic resonance as was first indicated by Hempstead and Bowers (2) and confirmed by all other workers in their studies on scheelites.

### 3.7.1 Heat-treatments of $Gd/CaWO_4$ samples in oxygen ambient and their interpretation

We found it necessary to heat treat our samples in oxygen atmosphere in order to establish the ordered-oxygen vacancy model. Our aim was to see whether it is possible to fill the proposed vacancies with oxygen

from outside the crystal, in which case we would expect the observed distortion to vanish, or at least to reduce. The furnace used in these heat treatments was built by W. Hutton and could reach a maximum temperature of about  $1200^{\circ}\text{C}$ . The 0.005% Gd sample was put to this test, firstly for 1 hour at  $1000^{\circ}\text{C}$ , secondly for 40 hours at  $1000^{\circ}\text{C}$ , and thirdly for 40 hours at  $1200^{\circ}\text{C}$ . The results of these heat treatment experiments were as follows. After the first experiment there was no change in the ESR behaviour of the sample. The change came after the second experiment and distortion of the line shape was observed at all angles  $\phi$ , (it was originally limited to angles  $\phi$  near  $55^{\circ}$ ). No further change was observed after the third heat treatment of the sample.

Our interpretation of these results is that the extended heat treatments at  $1000^{\circ}\text{C}$  and  $1200^{\circ}\text{C}$  failed to reduce the number of oxygen vacancies, and that the consequence was simply a more random distribution of these vacancies. This manifested itself in the persistent appearance of splitting, but now at all field orientations. It was decided not to attempt higher heat treatment temperatures, because of the possible changes in the single crystal structure which could have attended such treatments, as reported by Nassau and Broyer (8).

The suggestion of two sites for  $\text{Gd}^{3+}$  in calcium tungstate is, in fact, supported by some other experimental observations. The relevant evidence comes from measurements of spin-lattice relaxation time of the same samples under investigation, and is summarised as follows.

(i) The measurements of spin-lattice relaxation for  $\text{Gd}^{3+}$  in  $\text{CaWO}_4$  reported by Thorp, Buckley and Brown (26) showed the dependence of  $T_1$  on temperature over the range from 1.5 K to 8 K for the 0.01% Gd sample at  $\phi = 10^{\circ}$ . This was illustrated by two lines of slopes 1.0, 0.9

indicative of direct process of relaxation in this region. These two lines were attributed to the two components of Gd transition which was split and their separation was about 2 mT at that angle.

(ii) Our investigation of  $T_1$  in the temperature range 4.2 K to 30 K for  $\text{Gd}^{3+}/\text{CaWO}_4$  reported in Chapter 4 leads to a  $T^{-3}$  Raman-type of relaxation. This suggests the existence of a substantial number of defects which may lead to defected Gd sites, although the exact nature of these defects is not yet fully resolved.

## CHAPTER 4

### SPIN-LATTICE RELAXATION IN GADOLINIUM-DOPED CALCIUM TUNGSTATE

#### 4.1 Theories of spin-lattice relaxation

Before the discovery of magnetic resonance (by E. Zavoisky in 1944), Waller in 1932 (1), by measuring susceptibility at low frequency, suggested that the spin and orbital angular momenta of a paramagnetic ion were completely decoupled, and that the spin was influenced by the lattice vibrations (phonons) only by their modulation of the dipolar coupling. That is to say, the local magnetic field, which exists at one ion because of the magnetic dipole on a neighbouring ion, fluctuates due to fluctuations of the distance between the two ions under the action of the lattice vibrations. The resulting relaxation time was too long to explain the experimental results of the Leiden group; Gorter 1936 (2), or the more recent ESR studies. However, Waller's postulates were the first advances in this field; he distinguished spin-spin from spin-lattice relaxation, recognized the principal types of transition processes concerned in the latter (now known as direct and Raman processes) and set up the quantum mechanical framework for the calculation of their probabilities.

Kronig (3) and Van Vleck (4,5) independently suggested that there is no direct interaction between the phonon vibrations of a crystal lattice and the paramagnetic energy levels of an atomic spin in the lattice. Their mechanism is that when the lattice vibrates the orbital motion undergoes periodic changes due to vibrations in the crystalline electric fields. These changes react on the spins through the spin-orbit interaction, and thereby alter their orientation in the external magnetic field. The spin levels are thus indirectly connected to the lattice vibrations, and quanta of energy can be exchanged between the two. The agreement with the experimental data then in existence, (Gorter and his co-workers), was disappointing,

especially in that the observed dependence on the temperature and on the strength of the applied magnetic field was not as predicted. Also, according to Kronig and Van Vleck, the spin-lattice relaxation time of a spin should be independent of the spin-density, since the process involves only the individual spin and the surrounding lattice, and not any other spins which may be present. Consequently, it is concluded that the Kronig-Van Vleck theory seems to be valid only at very low spin concentrations, much smaller than those generally used in practical maser crystals, Paxman (6) and Zverev (7).

According to the detailed theory worked out by Kronig and Van Vleck there should be two contributions to the relaxation rate. The first is from a "direct process" in which the spin relaxes in either direction, by emitting or absorbing a single phonon at the spin transition frequency. The second contribution is from an "indirect" or "Raman" process in which a much higher frequency lattice-phonon is scattered by a spin and, thus, changing its frequency be enough to absorb the relaxation energy from the spin. The direct process should predominate at liquid helium temperatures, and somewhere above these temperatures the Raman mechanism should become significant. One of the aims of this chapter is to investigate these features in  $\text{Gd}^{3+}/\text{CaWO}_4$ .

Another important theory involving two-phonon process was suggested by Orbach (8) and verified experimentally by Finn, Orbach and Wolf in 1961 (9) and by Manenkov and Prokhorov in 1962 (10). The theoretical treatment is appropriate to rare earth ions and leads to predictions which agree both with the experimentally observed temperature dependence and with the magnitude of the relaxation time. The dominant relaxation process is one in which a phonon of high energy ( $\gg kT$ ) is absorbed by the spin system resulting in a transition from one of the ground state

doublet levels to the nearest excited level. Then, in a separate step, another high energy phonon is emitted and a transition is effected to the other level of the ground state doublet. The net result of this "two-step direct process" is the relaxation of the ground state doublet levels which brings the spin system towards thermal equilibrium. Some reasons for the success in the application of Orbach's theory to the rare-earth ions are given by Huang (11); the situation is unlike that applicable to ions of the iron group where the Kronig-Van Vleck treatment is much more valid. In the rare earths, the spin-orbit coupling is in general strong compared with crystal field effects, an effect which is due to the "screening" of the paramagnetic electrons in the embedded 4f unfilled shell. Thus the states of an ion are primarily of the type  $J = L + S$ , and, therefore, contain non-zero components of orbital angular momentum. Through the orbital angular momentum direct interaction between the magnetic states and the lattice vibrations is possible by means of orbit-lattice interactions. The magnetic spin is thus relatively strongly coupled to the lattice. For this reason spin-lattice relaxation times are generally very short ( $T_1 \sim 10^{-12}$  sec at normal temperatures) and low temperatures ( $\sim 20$  K) are often necessary to eliminate spin-lattice relaxation broadening of paramagnetic resonance absorptions.

The S-state ions such as  $Gd^{3+}$ ,  $Eu^{2+}$ ,  $Fe^{3+}$  and  $Mn^{2+}$  must be excepted from the foregoing discussion since their almost total lack of orbital momentum ensures that they are little affected by crystal fields. The spin-degenerate ground state of the free ion becomes in the crystal a group of closely spaced levels whose splitting rarely exceeds  $1 \text{ cm}^{-1}$  and the levels immediately higher, whose energies are likely to be greater by at least  $10^4 \text{ cm}^{-1}$ , are derived from states different in orbital and

spin degeneracy. In crystals, owing to the combined effects of the crystal field, spin-orbit and spin-spin couplings within the ion, the lowest spin multiplet is admixed with higher states having orbital momentum and different spin multiplicity, and thus becomes sensitive to lattice strain. The resulting relaxation has been considered by Blume and Orbach in 1962 (12,13) and Leushin in 1963 (14). The relaxation, instead of being entirely within the lowest Kramer's doublet, as might have been the case if the splitting were greater, is now dominated by transitions between doublets. A comprehensive survey of the theories of spin-lattice relaxation is now available in some texts by Abragam and Bleaney, 1970 (15), Poole and Farach, 1971 (16), and Standley and Vaughan, 1969 (17).

On applying these theories to the available experimental data they gave, in most cases, besides the qualitative fitting, a reasonable quantitative explanation of the way in which the spin-lattice relaxation time varies, particularly with temperature. A brief review of the relaxation processes and their variation with temperature is given below.

#### 4.2 Relaxation processes and their temperature dependence

As is mentioned in Section 4.1, two relaxation processes were postulated by Kronig and Van Vleck. These processes were distinguished earlier, in 1932, by Waller and became known as direct and Raman processes.

##### 4.2.1 The direct (or one phonon) process

It is the absorption, or emission, of a phonon of the same energy " $\hbar\omega$ " as the splitting energy " $\delta_{ab}$ " between two states

$|a\rangle$  and  $|b\rangle$  required for a resonance transition in the spin system and resulting in an upwards or downwards transition in that system. This is illustrated diagrammatically in Figure 4.1a. Calculation of the transition probability for this process for a Kramer's doublet (one in which the two spin states are time conjugates of each other and have half integral quantum numbers) leads to the dependence of  $T_1$  on temperature and applied magnetic field as

$$T_1 = a H^{-4} T^{-1} \quad (4.1)$$

while for non-Kramer's ions the dependence is

$$T_1 = a' H^{-2} T^{-1} \quad (4.2)$$

where  $a$  and  $a'$  are constants.

The energy density of phonons at frequency  $\omega$  within a certain band width  $d\omega$  is given by

$$\rho d\omega = \frac{\hbar \omega^3}{\pi^2 v^3} \frac{d\omega}{\exp(\hbar\omega/kT_0) - 1} \quad (4.3)$$

where  $v$  is the velocity of sound in the crystal.

The energy distribution of phonons according to a Debye spectrum at any particular lattice temperature could be illustrated as in Figure 4.2. Only these phonons, which have energies equal to the transition energy between the two relaxing levels, in other words, those which are on "speaking terms" with the spins, can take part in the direct process of relaxation. This is only an extremely small fraction of the total number of phonons and it can be shown that the direct process will predominate only at lower temperatures (liquid helium temperatures).



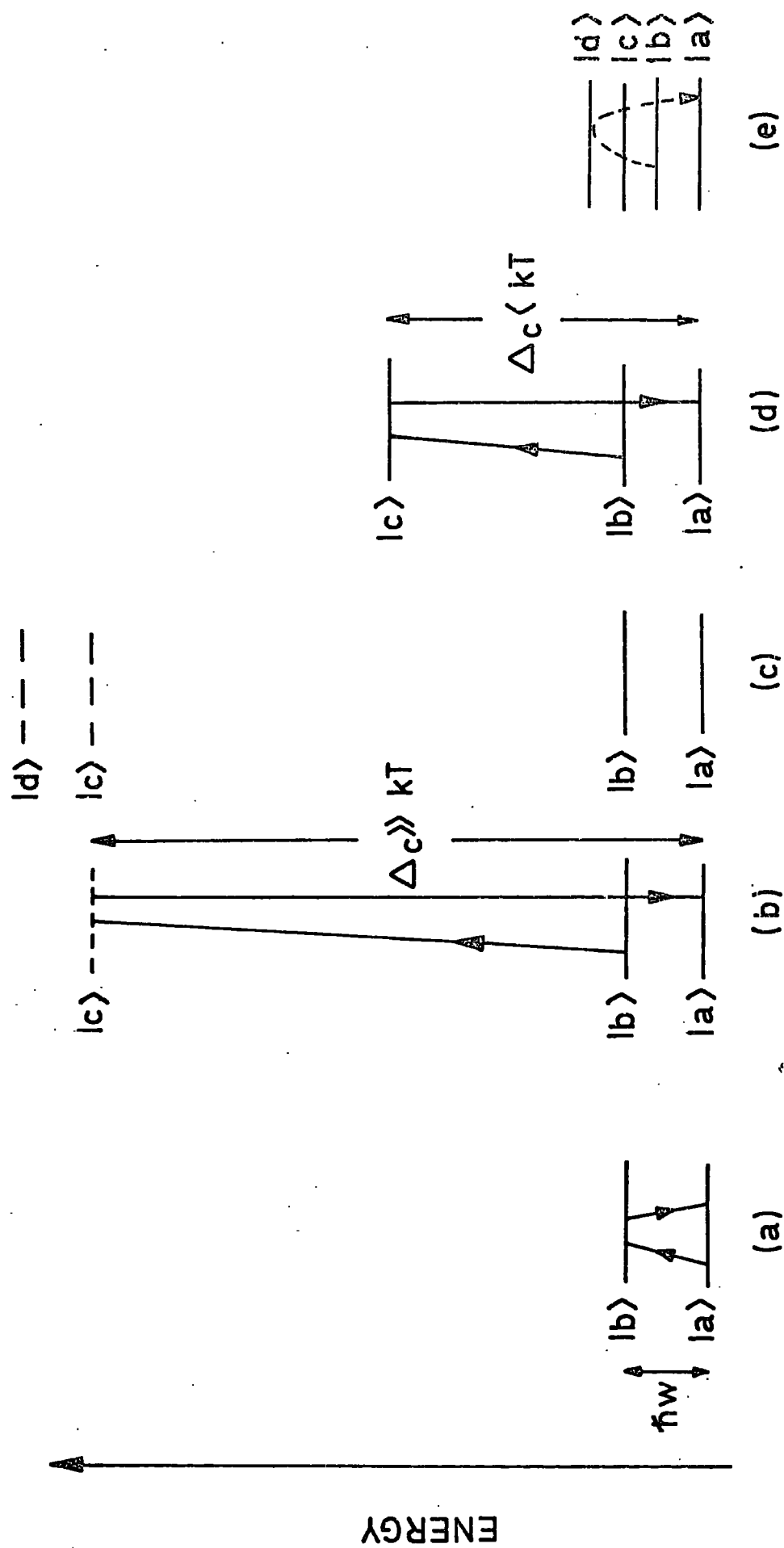


FIG.4.1 Diagrammatic representation of the different processes of spin-lattice relaxation.

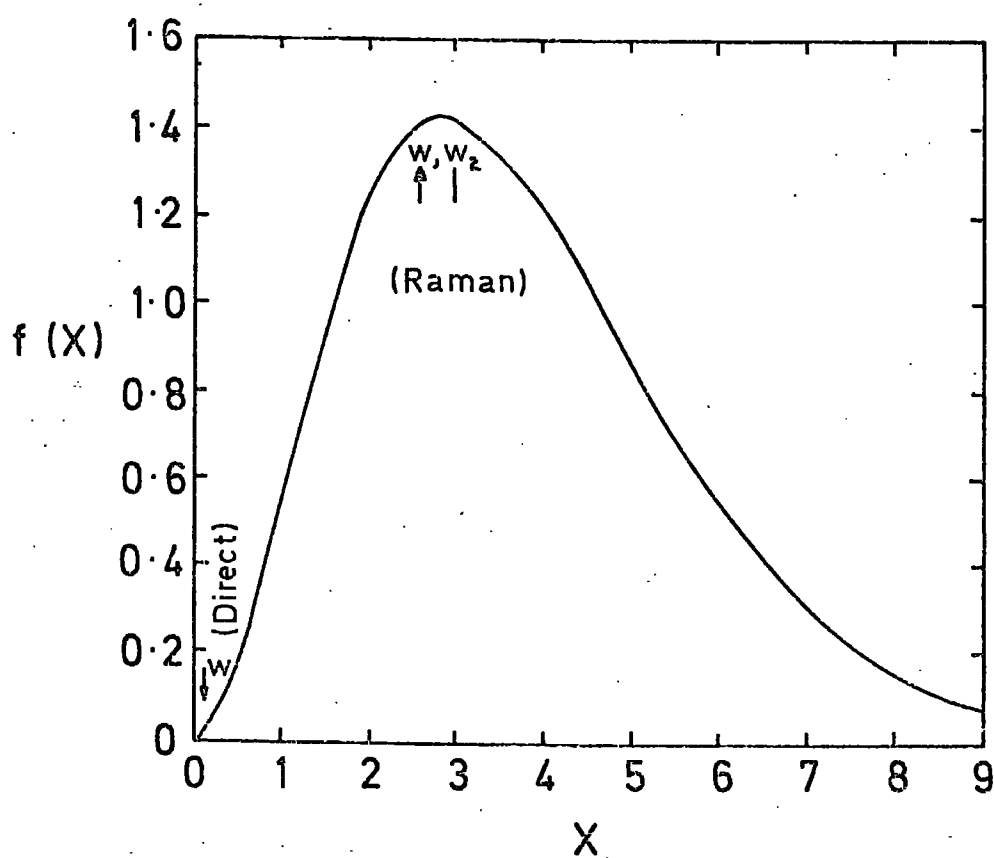


FIG.4.2 The energy distribution of phonons according to a Debye spectrum where  $f(X) = X^3/(e^X - 1)$  and  $X = \hbar w/kT$ .

#### 4.2.2 The two-phonon, Raman process

This process, involving two high frequency phonons, is similar to that introduced by Waller but, here, the interaction mechanism is explained by the ligand field theory rather than by the magnetic spin-spin interaction. In this process the magnetic ion makes a transition from state  $|b\rangle$  to state  $|a\rangle$ , or vice versa, accompanied by the virtual absorption of a phonon of angular frequency  $\omega_1$  and the emission of a phonon of frequency  $\omega_2$ . The energy difference  $\hbar\omega_1 - \hbar\omega_2$  is absorbed, or emitted, by the spin system effecting a transition as illustrated in Figure 4.1b. In the Raman process any two phonons can participate provided that their frequency difference is equal to the resonance frequency of the spin system. So, the much more abundant phonons near the peak of the energy distribution of the phonon spectrum, Figure 4.2, are also available. The calculated dependences for  $T_1$  due to this process are, for the Kramers ions,

$$T_1 = b T^{-9} + b_1 H^{-2} T^{-7} \quad (4.4)$$

where  $b$  and  $b_1$  are constants. The dependence on  $H^{-2} T^{-7}$  is only relevant under certain circumstances, as discussed by Orbach, 1961 (18). For non-Kramers ions the dependence is

$$T_1 = b' T^{-7} \quad (4.5)$$

where  $b'$  is a constant.

#### 4.2.3 Resonant two-phonon relaxation or Orbach process

As is mentioned earlier, this two phonon resonance process was suggested by Orbach in 1961 and first verified by Finn et al in 1961. Suppose that the magnetic ion has a set of energy levels such

as that shown in Figure 4.1c, where there are two low lying states  $|a\rangle$ ,  $|b\rangle$  (such as a Kramer's doublet), and an excited state  $|c\rangle$  whose energy separation  $\Delta_c$  is less than the maximum phonon energy, or

$$\Delta_c < \hbar \omega_p \quad (4.6)$$

where  $\omega_p$  is the phonon frequency.

In the Raman process there were no phonons of energy  $\Delta_c$ , so that transitions involving a virtual level  $c$  had to be imagined. It is, here, possible for an ion in, say, state  $|b\rangle$  to absorb a phonon of the appropriate frequency by a direct process, and be excited to the state  $|c\rangle$ . Then, a second phonon is emitted by a spontaneous or induced emission from that state  $|c\rangle$  to fall down to state  $|a\rangle$ . This gives an indirect transfer of ions from state  $|b\rangle$  to  $|a\rangle$ , and in so doing relaxation occurs between state  $|b\rangle$  and  $|a\rangle$ ; this may be faster than the direct transfer between them because of the much higher density of phonons of energy  $\Delta_c$  in the phonon spectrum. Orbach deduced a relaxation rate which in general practice becomes,

$$T_1 = C \exp(-\Delta_c/kT) \quad (4.7)$$

independent of an applied magnetic field except in so far as this may alter the value  $\Delta_c$ . This relation holds for both non-Kramers and Kramers ions provided that we consider a similar treatment for the excited states as for the Kramers doublets in the Raman analysis.

#### 4.2.4 Multiple ground state process

Orbach and Blume (12,13) considered the case where a multi-level Kramers state is lowest in energy. This is illustrated in Figure 4.1d,

where the states  $|c\rangle$  and  $|d\rangle$  have virtually the same energy as the states  $|a\rangle$  and  $|b\rangle$ . Therefore,  $\Delta_c$  is very small and, consequently, taking this into account in the derivation of the Raman process, as discussed by Abragam and Bleaney (15), another type of relaxation dominates with a temperature dependence as ,

$$T_1 = C' T^{-5} \quad (4.8)$$

where  $C'$  is constant.

Walker in 1968 (19) has described a mechanism that also gives a  $T^{-5}$  dependence with  $T_1$ , for non-Kramers doublets, than can operate between states of a multiplet which are not time-conjugates. Recently, an account of the various processes of electron spin relaxation was given by Gill, 1975 (20) concerning the establishment of thermal equilibrium in dielectric crystals containing paramagnetic ions of the transition elements.

#### 4.2.5 Modifications due to lattice imperfections

The theories mentioned above all deal with paramagnetic ions in crystallographically perfect diamagnetic lattice. The assumption of a perfect lattice is unlikely to be true for a doped single crystal because the paramagnetic ions, substituting at lattice points, usually differ in both mass and net electric charge from the ions they replace. They will, therefore, constitute defect sites that cause distortion of the symmetry of the surrounding ligand ions and also modification of the lattice waves. Moreover, any material grown at high temperature (for our  $\text{Gd/CaWO}_4$  the growth temperature is about  $1600^\circ\text{C}$ , using a Czochralski method), will contain a high number of crystallographic imperfections

due to the thermal stresses involved in the growth process. Also, defects of other types can play an important role, for instance, microfracture resulting when the crystal is cooled to the temperature of liquid helium.

As is established, spin-lattice interaction depends upon the extent to which the distances between a paramagnetic centre and the surrounding atoms change under the influence of lattice vibrations. The disturbance of the crystal field at the paramagnetic ion due to the alteration of the normal positions of the ligands will have the effect of introducing terms proportional to the lattice strain at the ligand ion into the expressions of the lattice potential.

An additional effect of lattice defects such as interstitial ions and substitutional ions, which are of different mass from those they replace, is modification of the assumed Debye spectrum of phonon modes. This involves the introduction of extra phonon modes, that may either be localized at the defect site or propagated through the lattice, and also scattering of normal phonon modes at the defect site. The scattering of these waves on crystal defects, though producing small changes in oscillation amplitudes, can however, lead to relative displacements of adjacent atoms much bigger than the displacements produced by Debye waves, as discussed by Kochelaev in 1960 (21). He considers that for two-phonon processes the influence of defects can be unimportant and that the greatest effect occurs in the direct process. He also derives an expression for the transition probability, taking as an example the ion  $\text{Cr}^{3+}$  in octahedral environment; his analysis shows that it is independent of magnetic field and inversely proportional to the distance between the paramagnetic ion and the defect site. This means that the relaxation time depends upon the concentration of the paramagnetic ions

and on the density of defect centres in the crystal.

The effects of localized phonon modes created at defect sites have been considered by Klemens, 1962 (22), Castle et al, 1963 (23), and Montrell and Potts, 1955 (24). Klemens (22) concludes that the only conceivable process involving a local mode is one in which a spin-flip is accompanied by the absorption and subsequent re-emission of a localized phonon.

When the relative spacing of the two spin levels in a magnetic field is perturbed by a change in the crystal field, due to a strain  $\epsilon$ , the perturbation Hamiltonian is of the form

$$H' = A\epsilon + B\epsilon^2 \quad (4.9)$$

where A and B are appropriate coupling parameters. The two processes, direct and Raman, are comparable at a temperature  $T_c$  given by Klemens as,

$$T_c \approx \frac{1}{2} (A/B)^{\frac{1}{3}} \theta_D^{\frac{2}{3}} (E/k)^{\frac{1}{3}} \quad (4.10)$$

where  $\theta_D$  is the normal Debye temperature, E is the spin energy (micro-wave energy), A and B are the constants given in the strained Hamiltonian equation (4.9).

The contribution of the localized modes to the Raman relaxation is given by Klemens as

$$1/T_{Ri} \approx \omega_i \left( \frac{\hbar \omega_i}{Mv} \right)^3 (B/E)^2 e^{-\theta_i/T} \quad (4.11)$$

where  $\theta_i = \hbar \omega_i / k$  and  $E = \Delta E$  is the spin energy,  $\omega_i$  is the angular frequency of the local mode, v is the velocity of sound,  $\left( v = (Ka^3/M)^{\frac{1}{2}} \right)$  where K is the elastic modulus, M and  $a^3$  are the mass and volume of the crystal, respectively). At sufficiently high temperatures  $1/T_{Ri}$  varies

as  $T_i^2$ ; in the same manner as  $1/T_R$  and, thus, makes a comparable contribution to  $1/T_1$  where  $1/T_R$  is given by ,

$$1/T_R = 36 \pi (B/Mv)^2 \omega_D (T/\theta)^7 \int_0^{\theta/T} \frac{x^6 e^x}{(e^x - 1)^2} dx \quad (4.12)$$

In this equation, the integral is used to be put in the form

$$J_n(x) = \int_0^x \frac{x^n e^x}{(e^x - 1)^2} dx \quad (4.13)$$

which has been tabulated (25) and it can be shown that at small values of  $x$ ,  $J_6(x)$  tends to  $x^5$ , and at large values of  $x$  the integral goes to a limiting value of 732.4. Thus,  $1/T_R$  varies as  $T^7$  at temperatures below about  $\theta/10$ , and as  $T^2$  above about  $\theta/2$ , as was obtained previously by Mattuck and Strandberg (26). By comparing equations (4.11) and (4.12), Klemens concluded that these two Raman processes become comparable at temperatures of about  $\theta/20$ , the ordinary Raman process predominates below that temperature and the exponentially increasing local mode Raman process dominates above that temperature.

Klemens' treatment is valid only if the local mode frequency  $\omega_i$  is well separated from the continuum of lattice modes. As  $\omega_i$  approaches  $\omega_D$ , the mode becomes progressively less localized. In the limit as  $\omega_i$  becomes equal to  $\omega_D$ ,  $1/T_{Ri}$  vanishes and the spin-lattice relaxation is given by the normal theory. The relationship between  $\omega_i$ ,  $\omega_D$  and the spatial extent of the local mode is discussed by Montrell and Potts (24).

Castle, Feldman, Klemens and Weeks, 1963 (23) found that the Raman relaxation at defect sites, characterized by a low frequency of local distortion, have a lower temperature dependence than the corresponding Raman relaxation in a perfect lattice. An explicit expression



was derived with the assumption of harmonic response of the local distortion at the defect site. The result was a temperature dependence for  $T_1$  of the form ,

$$T_1 \propto \left[ B \left( \frac{T}{\theta_D} \right)^7 J_6 \left( \frac{\theta_D}{T} \right) + B' \left( \left( \frac{T}{\theta_D} \right)^3 J_2 \left( \frac{\theta_D}{T} \right) - \left( \frac{T}{\theta_D} \right)^3 J_2 \left( \frac{\theta_i}{T} \right) + \frac{T^{11}}{\theta_i^8 \theta^3} J_{10} \left( \frac{\theta_i}{T} \right) \right] \quad (4.14)$$

where  $\theta_i$  and  $\theta_D$  are the Debye temperatures for a defected and perfect crystal respectively,  $J_n(x)$  is defined in equation (4.13) and  $B$  and  $B'$  are constant parameters whose ratio determines which form of Raman relaxation will dominate. Experimentally, these authors measured the spin-lattice relaxation at the defect sites formed by  $E'$  centres in irradiated synthetic quartz at 3 kilo-oersteds over a wide temperature range from 1.3 to 250 K. Their data was interpreted in terms of cross, direct and Raman relaxation processes. The dominant feature of the Raman relaxation was a temperature variation of about  $T^3$  when the characteristic frequency is sufficiently low compared to the Debye frequency.

#### 4.3 Experimental Results

From the foregoing analysis we realize that one of the main experimental techniques for uncovering the underlying mechanism of a relaxation process for a certain magnetic ion is to study the dependence on temperature of the relaxation rate. Another measurable property is the magnetic field dependence. The latter, however, is not always convenient since it involves the use of several microwave spectrometers operating at different frequencies. In this study, we are using the first technique for its relevance and convenience.

The samples used in this work are described earlier in Section 3.2. We were careful to use the same samples as those of Thorp et al (27) for the sake of comparison with their results and to explore the relaxation behaviour over an extended temperature range. The pulse-saturation method used in the previous work was again adopted. To allow measurement of spin-lattice relaxation times to be made over a wide temperature range above 4.2 K, the waveguide housing the specimen was surrounded by an araldite block (type AT1), as suggested by W. Hutton, Figure 4.3. The specific heat of this araldite was given by Parkinson and Quarrington (28), and due to its high thermal capacity at low temperatures it seemed to be a suitable material. The araldite, which was originally in a powdered form, was melted at  $\sim 120^{\circ}\text{C}$  and cured at  $\sim 140^{\circ}\text{C}$  overnight. Then it was machined to fit the waveguide and another piece of araldite was prepared as a plunger; this had a piece of brass attached to its end for short-circuiting the waveguide where the sample was located. With this arrangement the warming-up time was sufficiently slow to permit measurements at intermediate temperatures between 4.2 K and 30 K to be made without any additional temperature stabilization equipment; Copper-copper/constantan thermocouples were used for the temperature measurements.

The amplifier system used to detect the recovery to thermal equilibrium had a dead-time of 10  $\mu\text{sec}$ ; this dead time determined the upper temperature limit for measurements since it was found that  $T_1$  decreased to the same order as the dead-time at about 30 K. An estimate of the total error in measurements of  $T_1$  was between 10 and 15%, the main error resulting from misbalance of the bridge, Mason (29).

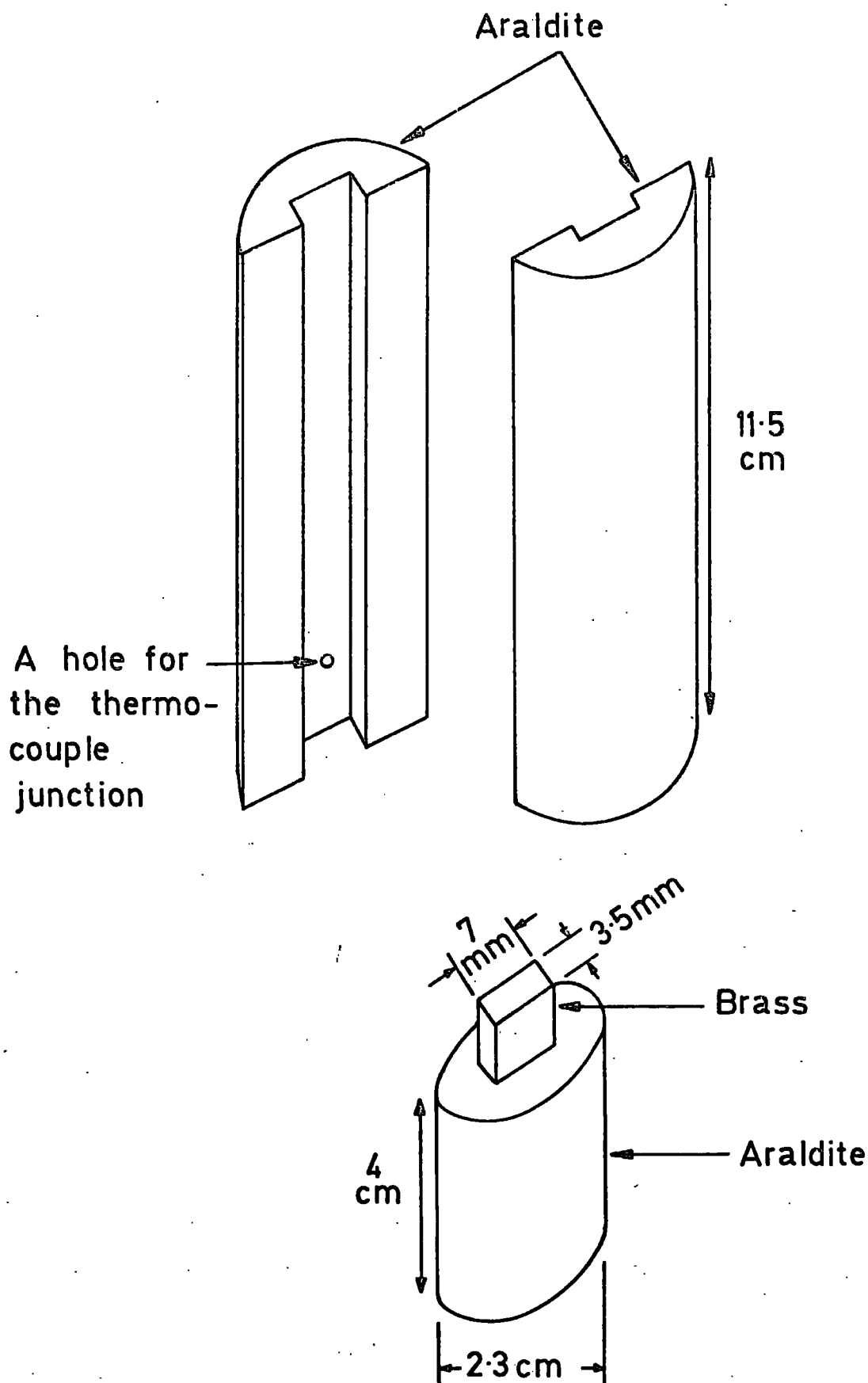


FIG.4-3 The shape of the araldite block fitted to the end of the waveguide.

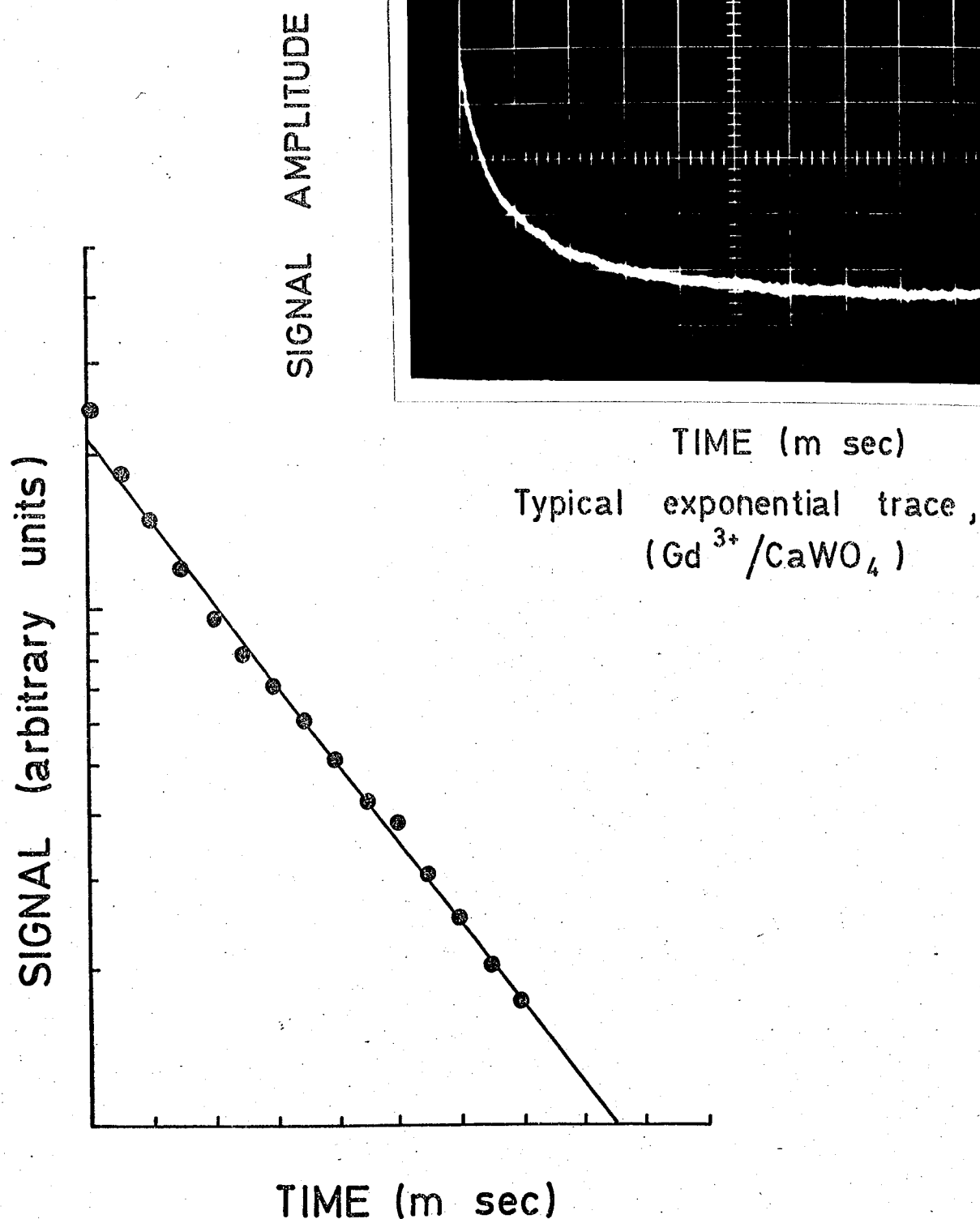


FIG.4.4 A semilogarithmic plot of the exponential recovery trace,  $T = 4.2\text{K}$   
 $\varphi = 8^\circ$ ,  $37.5\text{ GHz}$ .

#### 4.3.1 $T_1$ - temperature dependence measurements

To enable the data to be compared directly with the earlier results of Thorp et al (27) measurements are made with magnetic field perpendicular to the c-axis of the crystal, i.e. in the  $\phi$ -plane. The magnetic field was directed along the magnetic axis ( $\phi = 8^\circ$ ) because at this angle clean single ESR lines were observed with the two samples studied here which had nominal concentrations of 0.005 and 0.05 atomic per cent gadolinium. A typical photograph of the exponential recovery curve is shown in Figure 4.4. The semi-log plot of the recovery curve yielded a straight line, as previously reported (27), indicating that the recovery could adequately be described by a single exponential; this is true for all the recovery traces observed over the whole temperature range for the samples examined. The form of the temperature variation of  $T_1$  for the crystal containing 0.005 at.% Gd is shown in Figure 4.5, which for completeness includes the previous results obtained in the 1.5 K to 8 K region. The figure shows the occurrence of two distinct regimes indicative of a direct and a Raman-type relaxation. At temperatures below about 8 K the variation follows, to within experimental error, a  $T_1 \propto T^{-1}$  law. In this temperature range the magnitudes of  $T_1$  are found to be 5.8 msec at 4.2 K and 2.8 msec at 8 K, which are in close agreement with the previous measurements. The transition temperature between the two relaxation regimes is shown to be at nearly 8 K, and above this temperature the spin-lattice relaxation time varies as  $T_1 \propto T^{-3}$ , giving a value of  $T_1 = 1.6$  msec at 10 K and falling only to 0.07 msec at 28 K.

The corresponding temperature variation for the nominally higher gadolinium concentration sample, i.e. 0.05 at.% Gd, is depicted

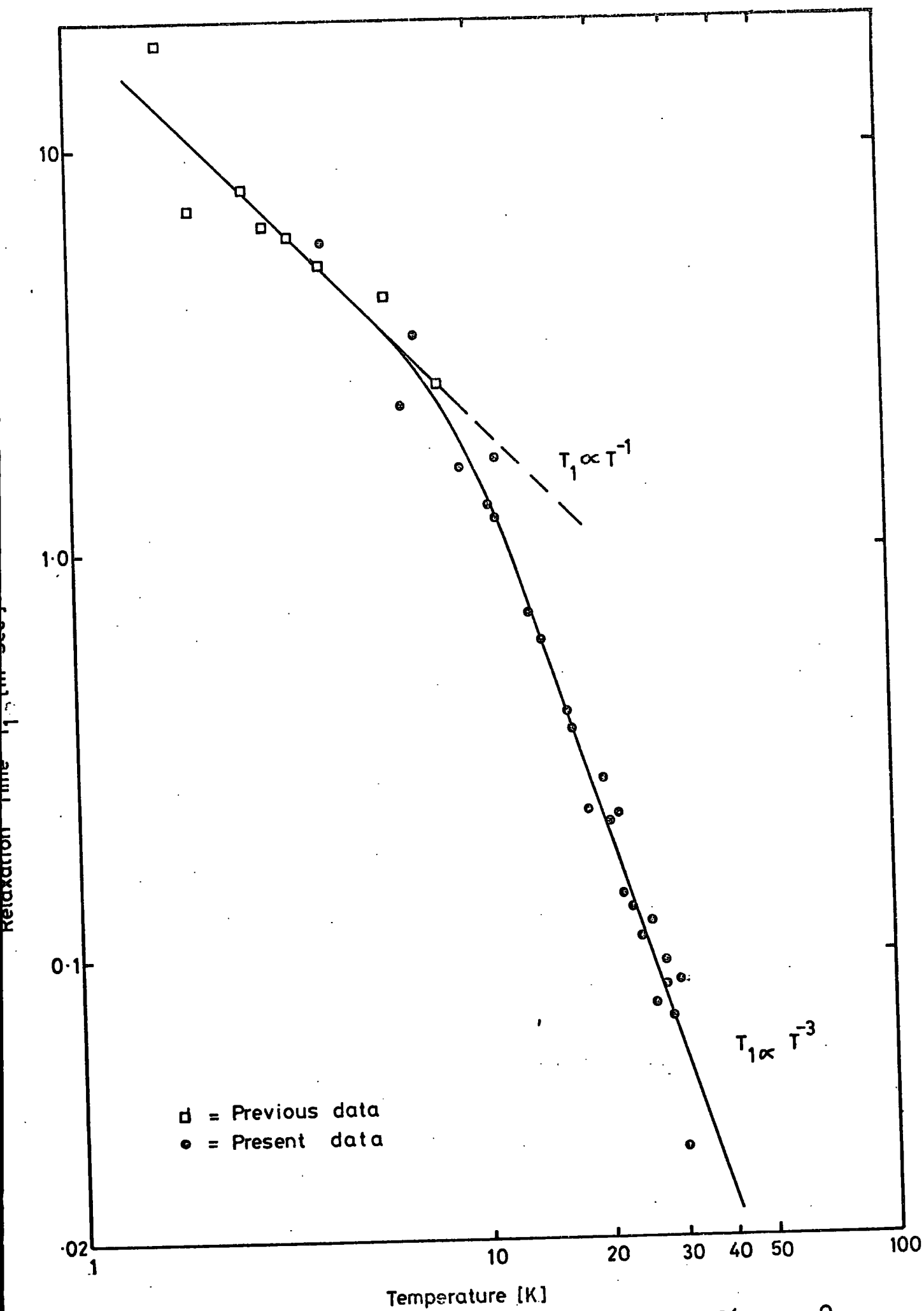


FIG 4.5 Temperature dependence of  $T_1$ ,  $\text{Gd/CaWO}_4$  [0.005%],  $\varphi = 8^\circ$   
Frequency 37.5 GHz.

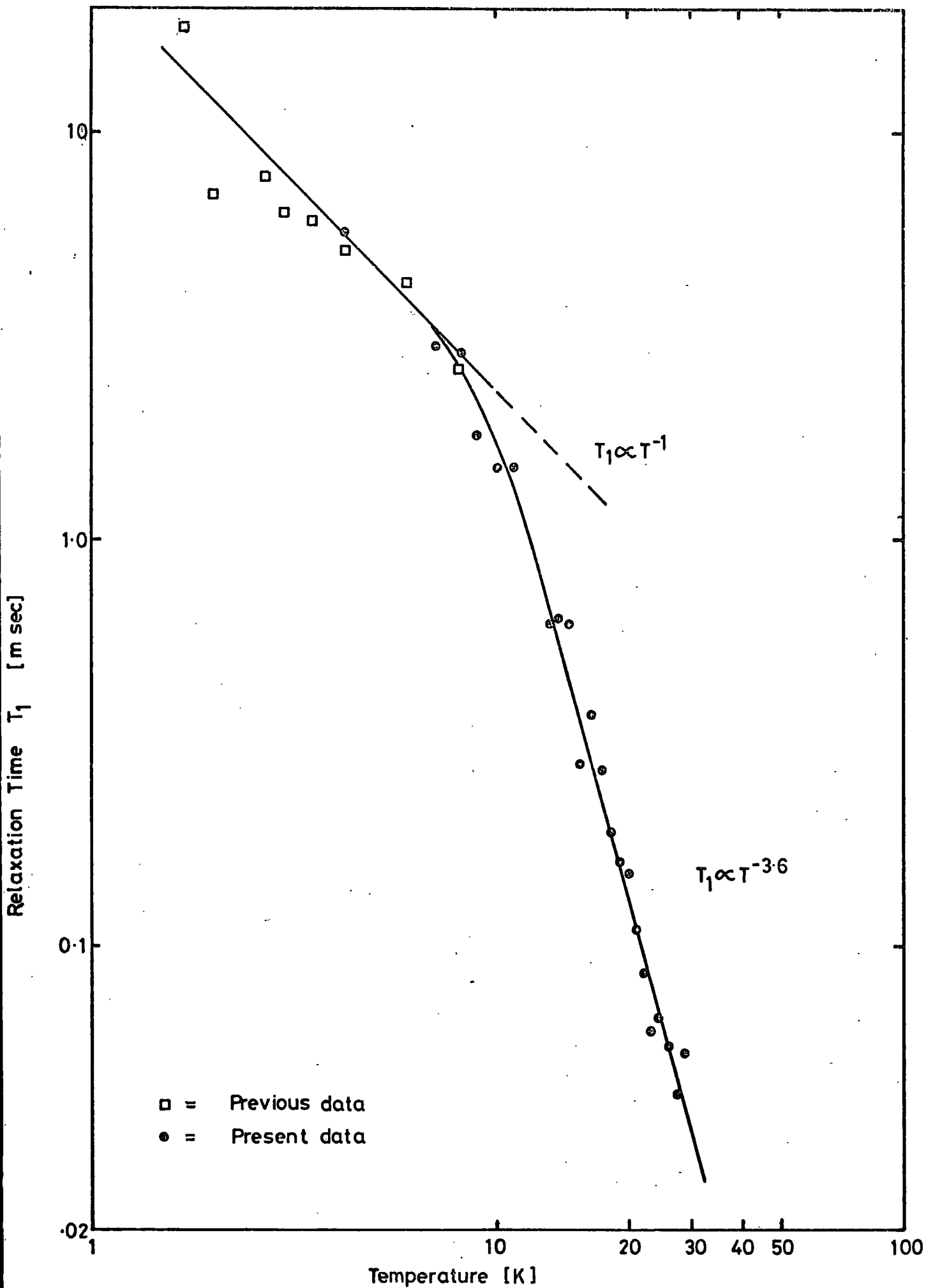


FIG4-6 Temperature dependence of  $T_1$ ;  $\text{Gd/CaWO}_4$  [0.05%],  $\varphi = 8^\circ$   
Frequency 37.5 GHz

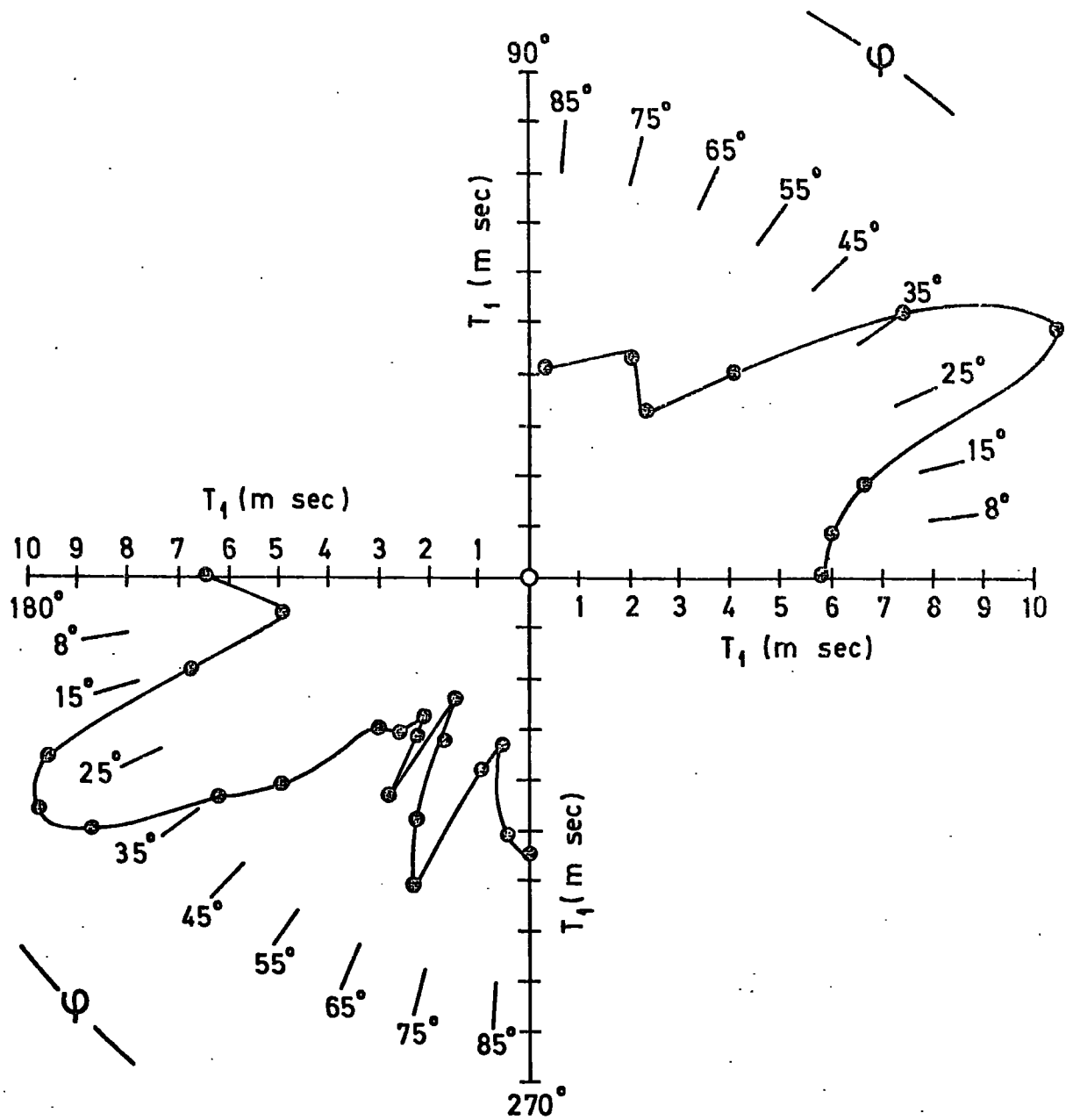


FIG. 4.7 Angular variation of  $T_1$  in the  $\phi$  - plane for  $Gd^{3+}/CaWO_4$  (0.005%), temperature 4.2 K, frequency 37.5 GHz.



in Figure 4.6. A very similar behaviour was obtained as with the first sample, with two distinct variations with temperature. The exponents of  $T_1$  in the lower region of temperature are  $(-1)$ , indicative of a direct process, and  $(-3.6)$  indicative of a Raman-type relaxation in the higher temperature region. These values are in agreement with those obtained from Figure 4.5. The actual magnitudes of  $T_1$  at corresponding temperatures, e.g. 5.8 msec for the 0.005 at.% Gd sample and 5.6 msec for the 0.05 at.% Gd at 4.2 K suggests that at these gadolinium levels  $T_1$  is not strongly dependent on concentration.

#### 4.3.2 $T_1$ - angular dependence measurements

Investigation of the angular variation of  $T_1$  was carried out for the sample 0.005 at.% Gd. Measurements were made in the  $\phi$ -plane at 4.2 K and the results are shown in Figure 4.7. It is found that  $T_1$  is anisotropic in the plane of measurements. In the first quadrant; ( $0 < \phi < 90^\circ$ ), there is a fairly broad but distinct minimum between  $\phi = 45^\circ$  and  $\phi = 65^\circ$ . It is shown that  $T_1$  varies from a maximum of 11.6 msec at  $\phi = 25^\circ$  to a minimum of 4.1 msec at  $\phi = 55^\circ$ ; at this angle  $T_1$  is reduced by a factor of about three. Rotation of the crystal through  $180^\circ$  in order to examine the range  $180^\circ < \phi < 270^\circ$ ; in the third quadrant, revealed a similar variation of  $T_1$  with a minimum near  $\phi = 235^\circ$  and a maximum at  $\phi = 205^\circ$ .

### 4.4 Discussion

#### 4.4.1 The temperature dependence of $T_1$

From the theories of relaxation mentioned in Section 4.1, we may formulate a general equation that gives the dependence of spin-lattice

relaxation time on temperature as ,

$$T_1^{-1} = AT^m + BT^n + C \exp(-\Delta_c/kT) \quad (4.15)$$

where A, B and C are constants. In the first term, in the absence of a bottleneck or cross-relaxation effects,  $m = 1$  indicating the occurrence of a direct process. In the second term; corresponding to the Raman process,  $n = 7$  for a non-Kramers ion or  $n = 9$  for a Kramers ion. The last term represents the Orbach mechanism, where  $\Delta_c$  is the energy splitting of the excited state above the ground level. Usually equation (4.15) is applicable only to salts where the paramagnetic ion concentration is low so that the experimental conditions approximate to the assumptions of a single ion theory where any co-operative mechanisms such as cross-relaxation or exchange interactions between clusters of ions are not involved. As we are dealing with an S-state ion we may expect that the Orbach-Blume mechanism will be effective, giving rise to a dominating  $T^5$  term in equation (4.15) instead of the normal Raman process. There is, in fact, experimental evidence for the  $T^5$  Raman behaviour in several S-state ions. For example, Bierig et al (30) found this kind of temperature dependence for  $Gd^{3+}/CaF_2$ , Chao-Yuan Huang (11) also observed it in  $Eu^{2+}/CaF_2$ ,  $Mn^{2+}/BaF_2$  and  $Mn^{2+}/SrF_2$ .

When considering our results on  $Gd^{3+}/CaWO_4$  we may notice first that the Orbach process is absent. It is known that the Orbach process is only important if the splitting  $\Delta_c$  is less than the Debye energy  $k\theta_D$ , which is that of the highest energy phonon in the lattice phonon spectrum, i.e. if

$$\Delta_c < k\theta_D \quad (4.16)$$

where  $\theta_D$  is the Debye temperature. For the gadolinium-doped crystals

used we may (in the absence of a direct determination), reasonably take  $\theta_D$  as the value for pure  $\text{CaWO}_4$  since the gadolinium concentration is low. Farley (32), using ultrasonic techniques for elastic constant determinations, reported that  $\theta_D = 155 \text{ K}$  for pure  $\text{CaWO}_4$ . From spectroscopic data the value of  $\Delta_c$  is about  $30000 \text{ cm}^{-1}$ , Dieke (33), and so  $k\theta_D$  is much less than  $\Delta_c$  ( $k = 0.695 \text{ cm}^{-1} \text{ K}^{-1}$ ). We thus conclude that the Orbach process is not a possible mechanism. Moreover, if defect centres are present in the crystals the effective Debye temperature may be less than  $\theta_D$  for a perfect lattice; hence the conclusion that the Orbach process is not possible remains valid for imperfect crystals. Reference back to the general equation (4.15), suggests therefore that for  $\text{Gd}^{3+}/\text{CaWO}_4$  a variation of the form

$$T_1^{-1} = AT^m + BT^n \quad (4.17)$$

may apply with  $m = 1$ , and  $n = 5$ . The absence of the Orbach term is confirmed by the experimental data because when plotting  $\log T_1^{-1}$  versus  $T^{-1}$  we do not get a straight line as should be expected if the recovery followed an Orbach mechanism, Figures 4.8 and 4.9. A similar treatment was followed by Scott and Jeffries (34). This absence of an Orbach type contribution was also found in the results obtained with the doped fluorides quoted above.

Our results, however, show that although there is a good fit to a  $T^{-1.0}$  variation at low temperatures, the variation above about 8 K is much less rapid than  $T^{-5}$ . To obtain a formula that fits the experimental results we followed an analysis similar to that used by Scott and Jeffries. Starting with equation (4.17) we can obtain the values of  $m$  and  $n$  from the log-log plots in Figures 4.5 and 4.6. Knowing them, we

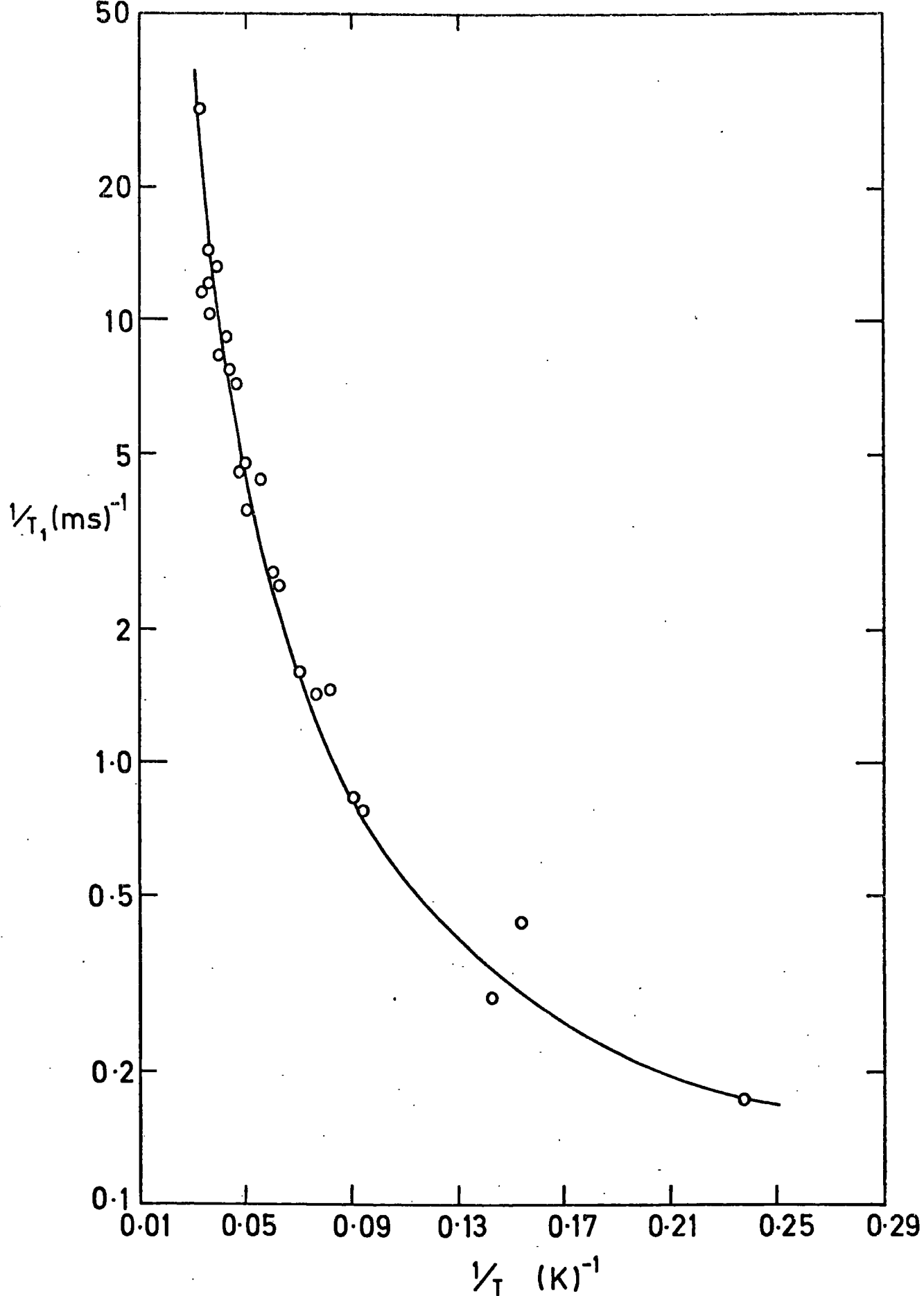


FIG. 4.8 Variation of  $\log. T_1^{-1}$  versus  $T^{-1}$  for sample of 0.005% Gd.

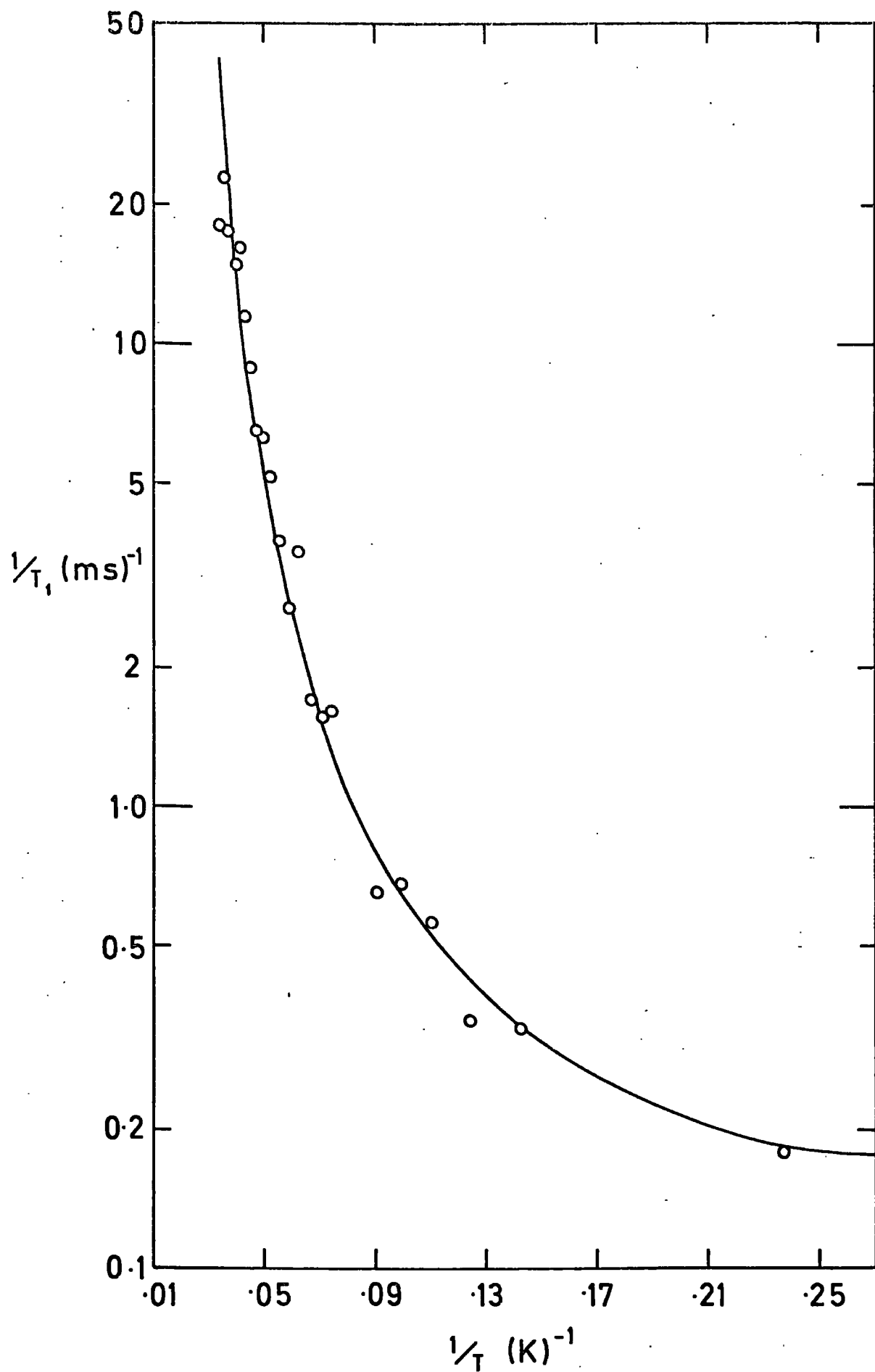


FIG.4.9 Variation of  $\log. T_1^{-1}$  versus  $T^{-1}$  for sample of 0.05% Gd.

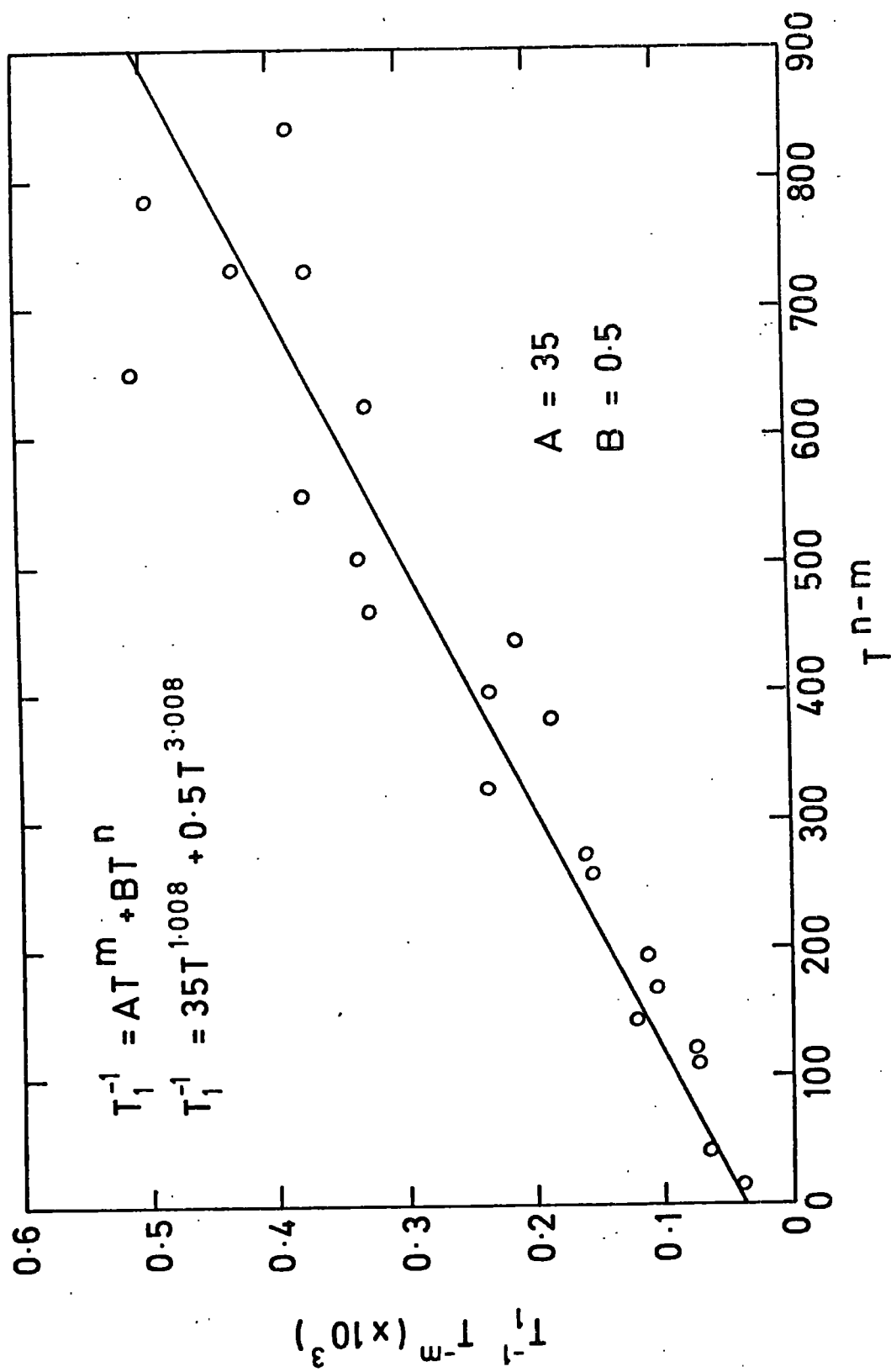


FIG. 4.10  $T_1^{-1}$  versus  $T^{n-m}$  for sample (0.005% Gd)

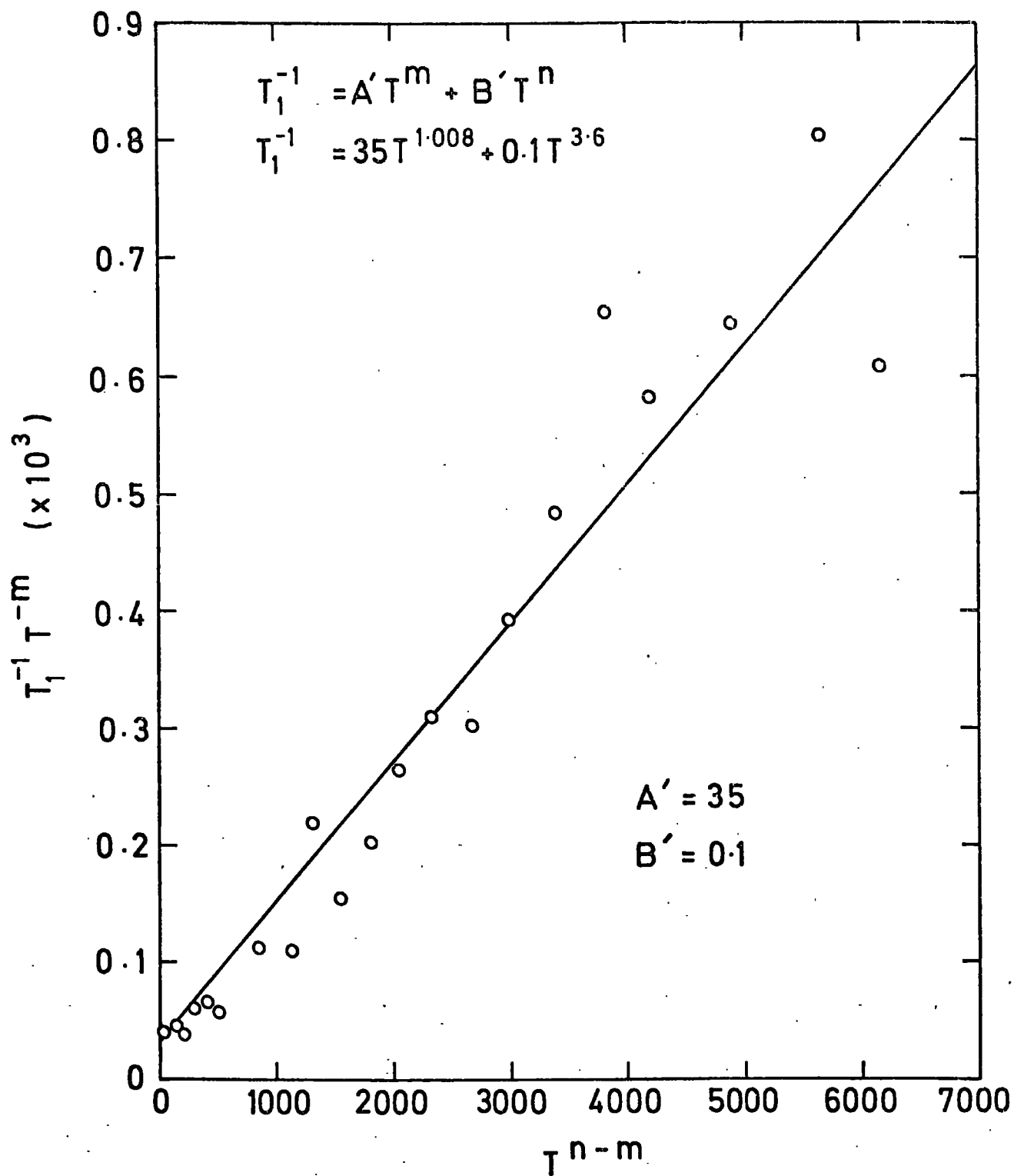


FIG. 4.11  $T_1^{-1} T^{-m}$  versus  $T^{n-m}$  for sample (0.05% Gd)

then plot  $T_1^{-1} T^{-m}$  versus  $T^{n-m}$  as in Figures 4.10 and 4.11. These give straight lines whose slopes and intercepts determine the constants A and B. Thus, the experimental data may be fitted by the expressions

$$T_1^{-1} = 35 T + 0.5 T^3 \quad (4.18)$$

for the 0.005 at.% Gd crystal, and

$$T_1^{-1} = 35 T + 0.1 T^{3.6} \quad (4.19)$$

for the 0.05 at.% crystal so that, on the average, one can take the variation as nearly  $T^3$  in the Raman-type region. Inspection of these equations shows that the contributions of the direct and Raman-type processes become equal at about 9 K, above which temperature the Raman-kind process is dominant as shown in Tables 4.1 and 4.2.

We may evaluate  $T_c$ , the temperature at which the direct and Raman processes are comparable, using Klemens' procedure, equation (4.10), which reduces to

$$T_c \approx \frac{1}{2} \theta_D^{\frac{2}{3}} \quad (4.20)$$

for the constants A and B may be comparable in magnitude and  $(E/k)^{\frac{1}{3}}$  is about unity in the microwave band we used. Next, we should take into account the change in the Debye temperature arising from the difference in masses of the dopant ion,  $Gd^{3+}$ , and the ion it substitutes,  $Ca^{2+}$ . Mason and Thorp (35) in their studies of the influence of the crystalline imperfections on spin-lattice relaxation in ruby, adopted the relation

$$\theta_i = m^{-\frac{1}{2}} \theta_D \quad (4.21)$$

to correlate between the Debye temperature for a defected crystal ( $\theta_i$ )



T (K)	First Term		Second Term		Total		Ratio $T_{1R}/T_{1D}$
	$T_{1D}$ (ms)	$1/T_{1D}$	$T_{1R}$ (ms)	$1/T_{1R}$	$T_1$ (ms)	$1/T_1$	
2	14.21	0.07	248.62	0.004	13.44	0.0074	17.6
3	9.44	0.11	73.43	0.01	8.36	0.12	7.8
3.5	8.08	0.12	46.18	0.02	6.88	0.14	5.7
4.2	6.73	0.15	26.67	0.04	5.37	0.19	4.0
6	4.69	0.21	9.13	0.11	3.10	0.32	1.9
8	3.51	0.28	3.84	0.26	1.83	0.54	1.1
9	3.12	0.32	2.70	0.37	1.45	0.69	0.9
10	2.81	0.36	1.96	0.51	1.16	0.87	0.7
12	2.33	0.43	1.13	0.88	0.76	1.31	0.5
14	2.00	0.50	0.71	1.40	0.53	1.90	0.4
16	1.75	0.57	0.48	2.10	0.38	2.67	0.3
18	1.55	0.64	0.34	2.98	0.28	3.63	0.2
20	1.39	0.72	0.24	4.10	0.21	4.82	0.2
22	1.27	0.79	0.18	5.46	0.16	6.25	0.1
24	1.16	0.86	0.14	7.10	0.13	7.96	0.1
26	1.07	0.93	0.11	9.02	0.10	9.95	0.1
28	0.99	1.01	0.09	11.27	0.08	12.28	0.1
30	0.93	1.08	0.07	13.87	0.07	14.95	0.1

Table 4.1: Evaluation of the fitting equation,

$$T_1^{-1} = 35 T + 0.5 T^3 \text{ for temperatures from } 2 \text{ K up to } 30 \text{ K.}$$

T (K)	First Term		Second Term		Total		Ratio $T_{1R}/T_{1D}$
	$T_{1D}$ (ms)	$1/T_{1D}$	$T_{1R}$ (ms)	$1/T_{1R}$	$T_1$ (ms)	$1/T_1$	
2	14.21	0.07	824.69	0.001	13.97	0.071	58.7
3	9.44	0.11	191.59	0.005	8.99	0.115	20.4
3.5	8.08	0.12	110.00	0.009	7.53	0.129	13.6
4	6.73	0.15	57.06	0.02	6.02	0.17	8.5
6	4.69	0.21	15.80	0.06	3.62	0.27	3.4
8	3.51	0.28	5.61	0.18	2.16	0.46	1.6
9	3.12	0.32	3.67	0.27	1.69	0.59	1.2
10	2.81	0.36	2.51	0.40	1.33	0.76	0.9
12	2.33	0.43	1.30	0.77	0.84	1.20	0.6
14	2.00	0.50	0.75	1.34	0.54	1.84	0.4
16	1.75	0.57	0.46	2.16	0.37	2.73	0.3
18	1.55	0.64	0.30	3.30	0.25	3.94	0.2
20	1.39	0.72	0.21	4.83	0.18	5.54	0.2
22	1.27	0.79	0.15	6.80	0.13	7.59	0.1
24	1.16	0.86	0.11	9.31	0.10	10.17	0.1
26	1.07	0.93	0.08	12.41	0.07	13.34	0.1
28	0.99	1.01	0.06	16.21	0.06	17.22	0.1
30	0.93	1.08	0.05	20.78	0.05	21.86	0.1

Table 4.2: Evaluation of the fitting equation ,

$$T_1^{-1} = 35 T^{1.008} + 0.1 T^{3.6}$$

for temperatures from 2 K to 30 K.

and that of a perfect crystal ( $\theta_D$ ), where  $m$  is the mass ratio of the dopant ion to that which it replaces. Knowing that  $\theta_D = 155$  K and the atomic weights of Gd and Ca are 157.25 and 40.08 respectively, we find that  $\theta_i = 78$  K. Substituting this value,  $\theta_i$  instead of  $\theta_D$  in equation (4.20) we get  $T_C \approx 9$  K which is almost the same as the values given from the experimental data (Figures 4.5 and 4.6) and those given from fitting expressions (Table 4.1 and 4.2).

The explanation of the observed  $T^3$  variation appears to lie in the presence of defects in the crystals. As is mentioned in Section 4.2.5, a  $T^{-3}$  variation with  $T_1$  in the Raman region was predicted by Castle et al (23) and fitted the observed behaviour of irradiation centres in quartz.

Also, a study of the temperature dependence of the relaxation times for ruby single crystals from 1.5 K to 120 K reported by Mason and Thorp (35) has shown that the chromium ions occupy two types of sites within the lattice, one perfect and the other distorted. Although these workers were studying different crystals with a different dopant their suggestion of the type of defect present in the ruby crystals is of much interest because it is very similar to the suggestion which is made in Section 3.7. It seems likely that this sort of defect is a possible reason for the observed  $T^3$  behaviour although detailed analysis is still needed for confirmation.

In order to present some figures for defect densities in  $\text{Gd}^{3+}/\text{CaWO}_4$  we notice that with the entry of  $\text{Gd}^{3+}$  ion into a  $\text{Ca}^{2+}$  site the formation of one calcium vacancy for every two  $\text{Gd}^{3+}$  ions occurs, which amounts to a calcium vacancy density of about  $10^{18} \text{ cm}^{-3}$ . Besides, concentrations of calcium and oxygen vacancies are also formed as Schottky

defects even in pure  $\text{CaWO}_4$  in air at the melting point. These are given by  $\phi_{\text{Ca}} = \phi_0 = 0.054$  atom percent, where  $\phi$  indicates a vacancy and subscripts indicate the crystal lattice site, Nassau (36). For  $\text{CaWO}_4$ , calculations of Schottky defects give the same order of magnitude mentioned above for calcium vacancy density, and hence for oxygen vacancy density. Furthermore, etching studies, Farley (32), showed that the dislocation density in calcium tungstate single crystals, grown by the same Czochralski technique as that used here, was about  $10^5 \text{ cm}^{-3}$ . We also notice that the temperature required for growth of calcium tungstate is about  $1600^\circ\text{C}$ ; that is considerably higher than that required for the fluorides in which (although data was not specifically given in the references quoted) a much lower dislocation density might be expected. Consequently there are substantial grounds for attributing the  $T^3$  variation to defects although their exact nature is not yet fully resolved.

#### 4.4.2 The angular variation of $T_1$

No theoretical treatment is attempted for the observed anisotropy of  $T_1$  in the  $\phi$ -plane. However, an interesting comparison of results comes from previous ultrasonic studies on  $\text{CaWO}_4$  single crystals made recently by Farley, Saunders and Chung in 1975 (37). These authors investigated the elastic properties of scheelite structure molybdates and tungstates and found that in the  $\phi$ -plane of calcium tungstate the Young's modulus was anisotropic. Two features were noted, a maximum at  $\phi = 68.8^\circ$  and a minimum at  $\phi = 23.6^\circ$ , and these were identified with the "axes of acoustic symmetry" which correspond to extrema in the ultrasound velocities and are the acoustic pure mode directions for which the acoustic energy flux direction is collinear with the propagation vector.

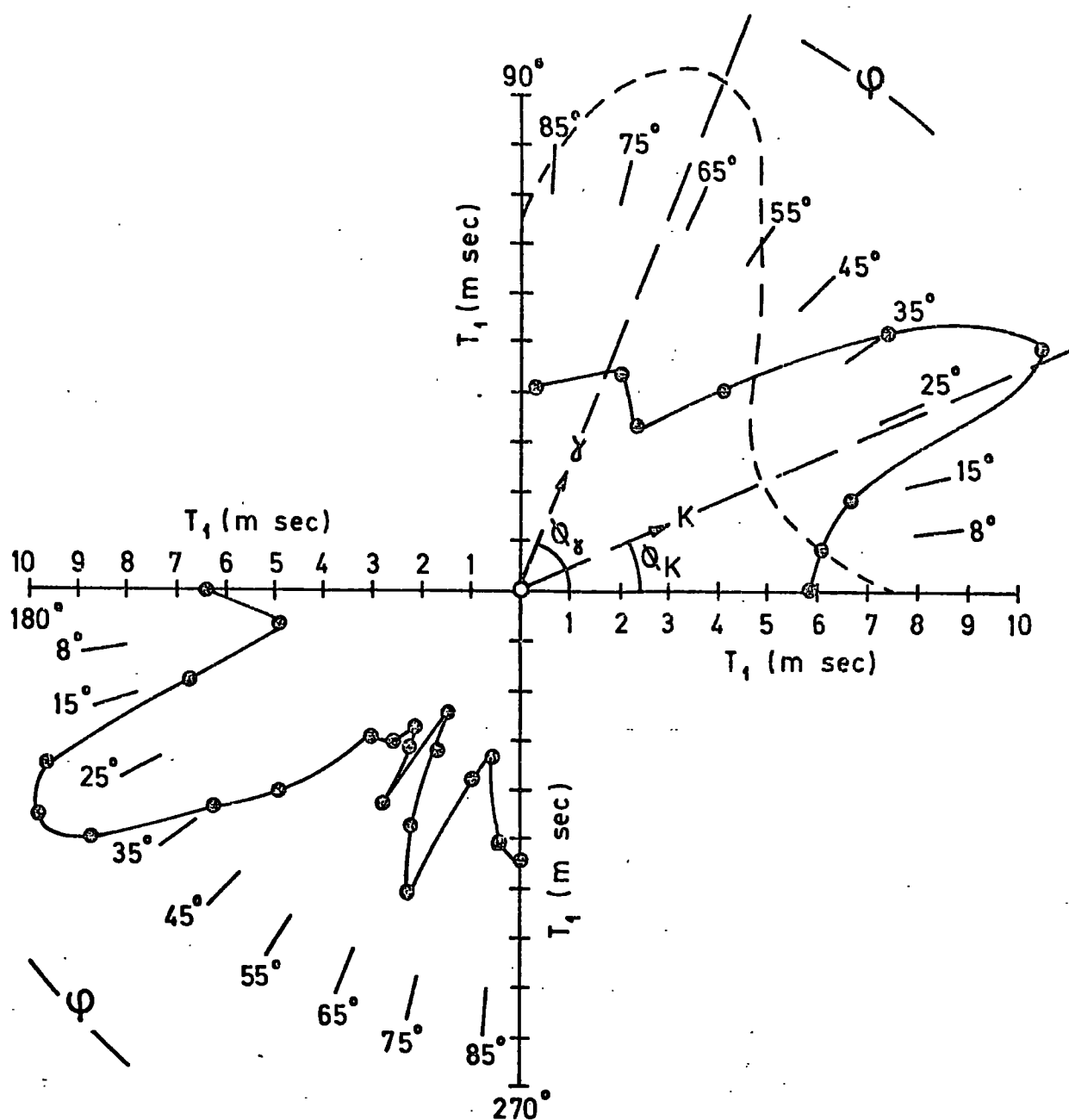


FIG.4.12  $T_1$  - Angular variation in the  $\varphi$  - plane for  $Gd^{3+}/CaWO_4$  (0.005%), temperature 4.2K, frequency 37.5 GHz, compared with ultrasonic measurements of Youngs modulus in the same plane (dotted curve).

The positions of extrema in our  $T_1$  variation show a remarkable coincidence with the "acoustic axes of symmetry" of the crystal. The ultrasonic and relaxation data are compared in Figure 4.12. They show a close fit between the direction of the minimum of  $T_1$  and the acoustic  $\gamma$ -axis, and also of the maximum of  $T_1$  with the acoustic  $k$ -axis. The ratio of Young's modulus along the  $\gamma$  and  $k$  axes was given as 2.1 at 295 K, compared with the ratio of about 2.1 at 4.2 K for the spin-lattice relaxation rates in these directions. It appears that the maximum relaxation rate (i.e. minimum  $T_1$ ) occurs when the ultrasound velocity is greatest and vice versa. The acoustic axes have 4/mmm symmetry in calcium tungstate and this accounts, on the same basis, for the maximum and minimum values of  $T_1$  found between  $\phi = 180^\circ$  and  $\phi = 270^\circ$ .

## CHAPTER 5

### SPIN-LATTICE RELAXATION OF $\text{Fe}^{3+}$ IN IRON DOPED MAGNESIUM OXIDE

The main interest in studying the spin-lattice relaxation of  $\text{Fe}^{3+}$  in magnesium oxide single crystals is that it provides another example of an S-state ion in a well known lattice structure. Although iron doped magnesium oxide has received a great deal of attention from previous workers, most of their ESR studies were at X-band frequencies ( $\sim 9$  GHz). The ESR spectrum of  $\text{Fe}^{3+}/\text{MgO}$  at magnetic fields of 13.5 KG (i.e. Q-band frequencies) was reported by Cheng and Kemp in 1971 (1). They used a method combining magnetic-circular-dichroism (MCD) and electron spin resonance (ESR) for studying the spin-lattice relaxation mechanism. No  $T_1$  values were published in their work. Spin-lattice measurements, however, received less attention and almost nothing was published at higher frequencies. Hence, our measurements of  $T_1$  at Q-band (37.5 GHz) are thought to contribute something to this field.

#### 5.1 Crystal structure, doping and charge compensation

The magnesium oxide structure is that of the well-known sodium chloride; of the type MX, where M denotes the metal ion or atom and X an electronegative element, e.g. oxygen in the oxides, or fluorine or chlorine in the halides, etc. The lattice is face-centred cubic of space group  $O_h^5$  as indicated by Cornwell (2), (the point group  $O_h$  and the assignment of superscript by Schonflies is rather arbitrary). Each magnesium atom has a coordination number of six, the neighbours being at the vertices of a regular octahedron. In this octahedral co-ordination the ionic radii, according to Kelly and Groves (3) for  $\text{Mg}^{2+}$  and  $\text{O}^{2-}$  are 0.65 Å and 1.40 Å respectively. Wyckoff (4) gave the lattice parameter

as  $a_o = 4.2112 \text{ \AA}$ . By doping the single crystals of MgO with iron, the latter is expected to go into the lattice by substitution at the magnesium sites; the predominant valency state is  $\text{Fe}^{3+}$  as concluded by Thorp, Vasquez, Adcock and Hutton (5) in their recent work on FSR linewidths of  $\text{Fe}^{3+}$  in MgO, whose optical measurements also revealed features indicative of  $\text{Fe}^{3+}$ . This, besides the observed ESR spectra at X- and Q-bands (9.1 and 35.5 GHz) gave confirmation of their conclusion. Further support is given by the comparison of the ionic radii of  $\text{Fe}^{3+}$  which at  $0.64 \text{ \AA}$  (3) is almost the same as the corresponding  $\text{Mg}^{2+}$  ion. The extra positive charge on the  $\text{Fe}^{3+}$  ion however requires that there should be some mechanism for charge compensation in the crystal. Actually, three processes for achieving charge neutrality could be effective as discussed by Wertz and Auzins (6). First, compensation might occur with an extra electron on an oxygen ion,  $\text{O}^{-3}$ . However, this was dismissed as representing a very unstable configuration. This leaves us with two reasonable possibilities outside the oxygen octahedron. One is replacement of a  $\text{Mg}^{2+}$  ion by a unipositive ion such as the  $\text{Li}^{+1}$  ion, which was postulated by Prener (7). From the ionic radii point of view, this should fit readily in the crystal (with  $\text{Na}^{+1}$  less likely), while any other unipositive ion is probably too large to fit without undue distortion. The alternative is to have  $\text{Mg}^{2+}$  vacancies distributed at random throughout the crystal. The possibility of interstitial  $\text{O}^{-1}$  ions was rejected, since there is hardly room in the lattice to accommodate them.

## 5.2 Experimental results and discussion

The single crystals of iron-doped magnesium oxide upon which measurements were made were obtained from W & C Spicer Ltd. (Cheltenham), having been grown by electrofusion using pure powdered ferric oxide and pure



powdered magnesia as the starting materials. Since there was no deliberate doping of a univalent element to maintain charge neutrality one may invoke the vacancy compensation mechanism. The iron concentrations in the samples used in this work were 140, 310 and 710 p.p.m.; these had been determined by optical spectrographic analysis (Johnson-Matthey Ltd.) to an accuracy of about 2%. Neither optical examination nor x-ray back reflection photographs, used to orient the samples, revealed any evidence of macroscopic cracking, flaws, strain or mosaic formation. This led us to assume that the samples were of good crystal-line quality.

The pulse saturation technique, as mentioned before, was used for the spin-lattice relaxation measurements at 37.5 GHz. Measurements were carried out for the central  $\frac{1}{2} \longleftrightarrow -\frac{1}{2}$  transition at 4.2 K, except when otherwise mentioned elsewhere.

#### 5.2.1 Observation of two decay rates

The crystals were oriented so that the magnetic field  $H$  was along the  $\langle 100 \rangle$  direction. In most of the semi-logarithmic plots produced from the photographs of the exponential decay curves, the existence of two relaxation rates could be observed as in Figure 5.1. The longer relaxation time was taken as the spin-lattice relaxation time  $T_1$ , whilst the shorter relaxation time could be attributed to some contribution from the energy levels of the system in a cross-relaxation mechanism, as discussed by Manenkov and Prokhorov (8). Previous experimental results on  $\text{Fe}^{3+}/\text{MgO}$  at 10 GHz by Castle and Feldman gave two values for the exponents in the rate equation and were published by Shiren (9). In a preceding publication, Shiren (10) reported measurements of spin-phonon interactions for iron group ions  $\text{Cr}^{3+}$ ,  $\text{Mn}^{2+}$ ,  $\text{Fe}^{3+}$ ,  $\text{Fe}^{2+}$  and  $\text{Ni}^{2+}$  in  $\text{MgO}$ ,

Present results $T_1$ at 37.5 GHz	Computed $T_1$ (9) at 10 GHz	Measured $T_1$ (9) at 10 GHz
0.8 ms	50 ms	714.3 ms
0.3 ms	26 ms	23.8 ms
	7.6 ms	

Table 5.1: Observations of more than one decay constant in the relaxation of  $\text{Fe}^{3+}/\text{MgO}$  at 4.2 K.

utilizing microwave ultrasonic spin resonance techniques. Using his measured spin-phonon coupling constants, Shiren (9) calculated the relaxation times from the theories as proposed by Van Vleck (11) and modified by Mattuck and Strandberg (12). Our results are given in Table 5.1 in which they are compared with Shiren's computed values and the measurements of Castle and Feldman of  $T_1$  for  $\text{Fe}^{3+}/\text{MgO}$ . This table shows the presence of more than one component in the relaxation decay of  $\text{Fe}^{3+}/\text{MgO}$ , in both the experimental and predicted data, although direct comparison of the results is not convenient at this stage because of the difference in the operating frequencies. Shiren's computations were based on deriving the rate equations, as already given by Andrew and Tunstall (13), for the different energy levels available in the system. For ions with  $S = \frac{5}{2}$  and the  $\Delta m = 1$  transitions there are, in general, three relaxation rates in the return to equilibrium from saturation or inversion. Experimentally, the relaxation behaviour of a particular level will frequently be dominated by one of the relaxation rates if it has a large amplitude constant. In our measurements we have taken the final part of the recovery curve, which gives the longest component, to derive the spin-lattice relaxation time  $T_1$ .

#### 5.2.2 Temperature dependence of $T_1$ for $\text{Fe}^{3+}/\text{MgO}$

Measurements of spin-lattice relaxation time  $T_1$  were made in the temperature range from 4.2 K to 27 K for the  $\text{Fe}^{3+}/\text{MgO}$  sample of 310 p.p.m. Fe doping. The magnetic field was directed along the  $\langle 100 \rangle$  direction of the crystal and we monitored the relaxation of the  $\frac{1}{2} \longleftrightarrow -\frac{1}{2}$  transition. The araldite block was again used, as mentioned in the preceding chapter, Section 4.3, as a means of letting the system warm up slowly enough for monitoring the change of spin-lattice relaxation time with temperature.

The variation of  $T_1$  in the range of temperatures studied, is depicted in Figure 5.2. This shows two regimes of dependence on temperature  $T_1$  as  $T^{-1}$  at lower temperatures and  $T^{-4.6}$  above about 20 K. The values of  $T_1$  were derived from the photographs of the exponential decay traces at the corresponding temperature by choosing the longest relaxation time as the spin-lattice relaxation time at that temperature. The observed dependence of  $T_1$  on temperature agrees with the theoretical predictions demonstrating a  $T^{-1}$  behaviour as a direct process at low temperatures and a  $T^{-4.6}$  variation as a Raman process at higher temperatures. As an S-state ion,  $\text{Fe}^{3+}$  should obey a  $T^{-5}$  variation of  $T_1$  with temperature in the Raman region as discussed in Section 4.2.4. Knowledge of the transition temperature  $T_C$ , at which the Raman process begins to dominate over the direct process, can provide information about the Debye temperature of the crystal. This was attempted by carrying out a similar treatment as previously made for  $\text{Gd}^{3+}/\text{CaWO}_4$  in Section 4.4.1. The only difference here is that we start with a known value for  $T_C$  to derive the Debye temperature  $\theta_D$ , whereas in the previous treatment we have done the reverse. Quoting equation (4.20) in Section 4.4.1, this gives the relation of  $T_C$  and  $\theta_i$  as

$$T_C \approx \frac{1}{2} \theta_i^{2/3}$$

From Figure 5.2,  $T_C = 20$  K, hence

$$\theta_i = 253 \text{ K}.$$

Also, as we are dealing with  $\text{Fe}^{3+}$  ions which substitute for Mg ions in the MgO single crystal we may use the relation

$$\theta_i = m^{-1/2} \theta_D$$

where  $m$  is the ratio of the atomic masses of iron to magnesium ions.

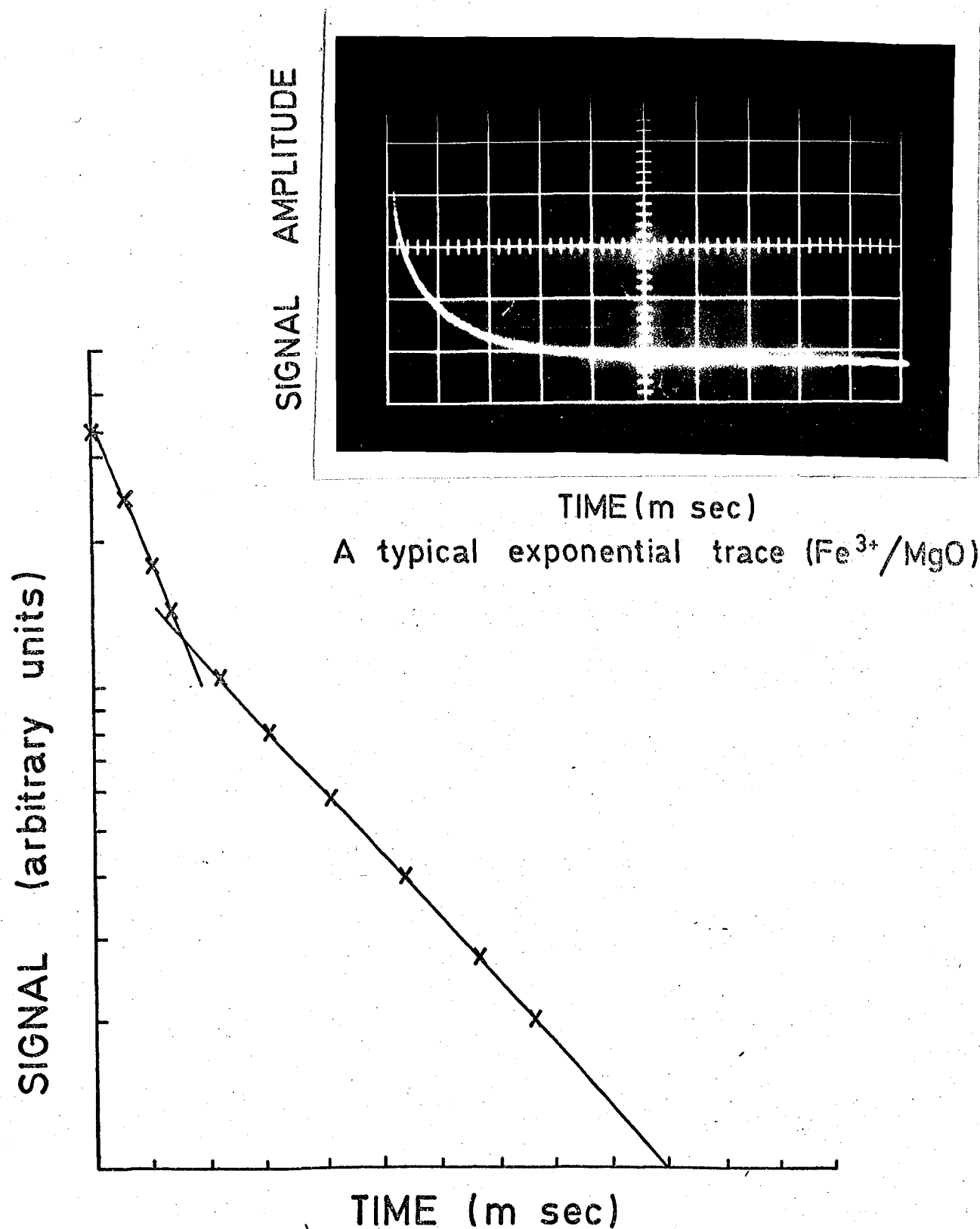


FIG. 5.1 A semilogarithmic plot of the exponential recovery trace at 4.2 K & 37.5 GHz.

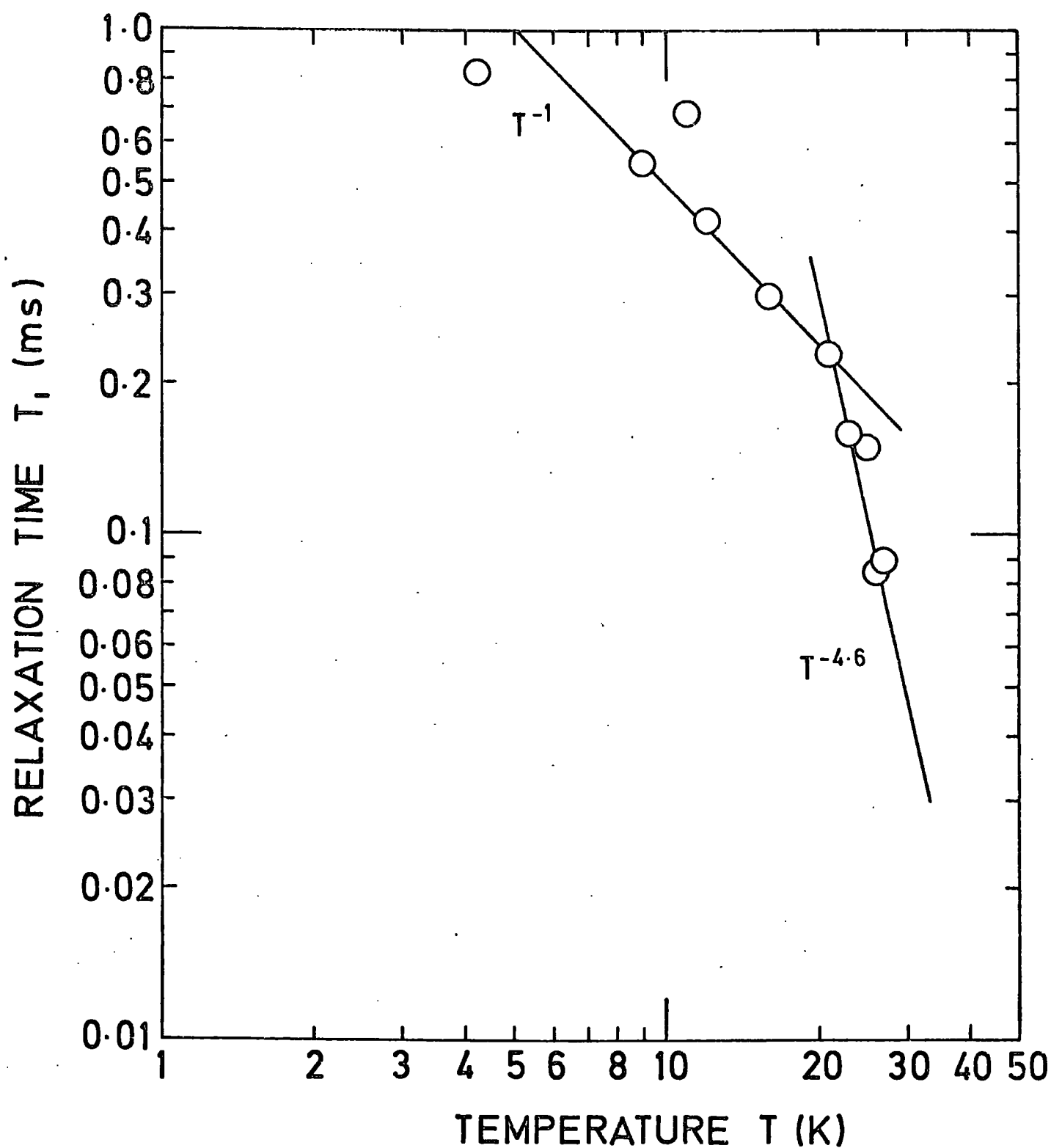


FIG. 5-2 Temperature dependance of  $T_1$ ;  $\text{Fe}^{3+}/\text{MgO}$ , 310 ppm Fe, at 37.5 GHz.

Therefore ,

$$\theta_i = \left( \frac{55.847}{24.305} \right)^{-\frac{1}{2}} \theta_D$$

or ,

$$\theta_D = 383 \text{ K} .$$

For comparison, we find from the physical tables (14) that the Debye temperature for MgO has been given as 946 K. This was reported by Barron et al, 1959 (15), when studying the heat capacity of crystalline magnesium oxide. It was found that their published value was the Debye temperature at 0 K ( $\theta_0$ ) and from their plotting of  $\theta_D$  versus temperature in the range  $20 < T < 300$  K we found that  $\theta_D$  at 77 K is nearly 750 K. This shows that our estimated  $\theta_D$  is far below that published by Barron et al. Reasons for the discrepancy in the results may be (a) the differences in the experimental techniques, (b) the preparation of the samples examined. This latter condition may include the particle size of MgO, the surface roughness and other possible factors such as contamination of the surfaces by adsorbed gases.

This value of  $T_C$  is in exact agreement with that reported by Pace, Sampson and Thorp, 1961 (16) in their studies on synthetic sapphire ( $\text{Fe}^{3+}/\text{Al}_2\text{O}_3$ ) at 34.6 GHz. Using a pulse saturation method, they found that the main features of the variation of the relaxation times show a  $T^{-1}$  dependence on temperature up to 10 K and a transition to a region of  $T^{-5}$  occurs at about 20 K.

Kask et al, 1963 (17) studied the paramagnetic relaxation of the  $\text{Fe}^{3+}$  ion in corundum ( $\text{Al}_2\text{O}_3$ ) in the 3-cm range by utilizing the pulse saturation method. The temperature dependence of  $T_1$  was determined in the interval 2 - 80 K. It was shown that  $T_1$  varies approximately as

$T^{-1}$  in the region from 2 to 5 K. In the interval 5 - 15 K,  $T_1$  varied anomalously slowly and in the 20 - 80 K range  $T_1$  varied as  $T^{-6}$ .

### 5.2.3 Concentration dependence of $T_1$

Measurements of  $T_1$  for the  $\text{Fe}^{3+}/\text{MgO}$  samples available gave the values presented in Table 5.2. Again, we emphasize that the spin-lattice relaxation time  $T_1$  was chosen as the longer time in the semi-logarithmic plots of the recovery traces photographs. These were taken at 4.2 K with the magnetic field  $H$  along the  $\langle 100 \rangle$  direction.

It has long been observed that at sufficiently low temperatures and sufficiently high concentrations of paramagnetic impurities the transfer of energy from a spin system to the lattice may be dominated by concentration-dependent relaxation processes. One explanation was suggested by Van Vleck, 1960 (18), i.e. that the spins in the crystal cross relax to some paramagnetic sites which relax rapidly to the lattice. The rapidly relaxing sites may, for example, consist of spins of a paramagnetic species having exceedingly short spin-lattice relaxation times, spins located in distorted crystal fields, or exchange-coupled clusters of two or more ions which relax rapidly to the lattice as a result of phonon modulation of the exchange coupling. In studying the spin-lattice relaxation of  $\text{Cr}^{3+}$  ions in ruby crystals, Standley and Vaughan, 1965 (19) suggested that the observed concentration-dependence is possibly due to impurity ions that constitute the fast relaxing centres. Solomon in 1966 (20) studied the concentration-dependence of spin-lattice relaxation times for  $\text{Mn}^{2+}$  and  $\text{Fe}^{3+}$  in MgO at 9.6 GHz utilizing the technique of saturation recovery. He found that  $T_1$  is roughly proportional to the inverse of concentration. Similarly, we apply this law to our results and it gives the values presented in the last column in Table 5.2. The agreement between the



Concentration (ppm)	Measured $T_1$ (m sec)	Predicted $T_1$ (m sec)
140	1.0	1.0
310	0.8	0.5
710	0.1	0.2

Table 5.2: Concentration dependence of  $T_1$

experimental and predicted values of  $T_1$  is good and it is tempting to conclude that for  $\text{Fe}^{3+}/\text{MgO}$  the spin-lattice relaxation time obeys (concentration) $^{-1}$  law.

#### 5.2.4 The angular variation of $T_1$

The variation of relaxation time  $T_1$  with crystal orientation for the  $\frac{1}{2} \longleftrightarrow -\frac{1}{2}$  transition for  $\text{Fe}^{3+}/\text{MgO}$  has been experimentally investigated. Three samples of iron concentrations 140, 310, 710 p.p.m. were examined at liquid helium temperature (4.2 K). The spin-lattice relaxation times were measured in the angular range from  $\theta = 0^\circ$  to  $\theta = 90^\circ$ , where  $\theta$  is the angle between the magnetic field  $H$  and the  $\langle 100 \rangle$  direction of the crystal. The angular dependence behaviour of these three samples is depicted in Figure 5.3. The sample of 310 p.p.m. Fe showed two apparent minima at angles  $\theta$  of about  $30^\circ$  and  $75^\circ$ , having values of  $T_1$  as 0.44 m sec and 0.49 m sec, respectively. This behaviour was not evident for the other two samples; 140 p.p.m. Fe and 710 p.p.m. Fe. However, we noticed that the 310 p.p.m. Fe sample did not show 'extra' lines in the ESR spectrum as did the 140 and 710 p.p.m. Fe samples, which might indicate that they are not exactly similar and differences in behaviour might arise. The decrease in  $T_1$  values at certain angles could be explained by the cross-relaxation between two, or more, transitions. It is interesting to know that, from Thorp et al's (5) studies on linewidths of  $\text{Fe}^{3+}/\text{MgO}$ , at these angles of minimum  $T_1$  values the  $-\frac{3}{2} \longleftrightarrow -\frac{1}{2}$  and  $\frac{1}{2} \longleftrightarrow \frac{3}{2}$  transitions are expected to overlap with the main transition ( $\frac{1}{2} \longleftrightarrow -\frac{1}{2}$ ).

Donoho, 1964 (21) worked out the theoretical investigation which predicted the form of the angular dependence for  $\text{Cr}^{3+}$  in ruby. No such theoretical treatment was attempted for  $\text{Fe}^{3+}/\text{MgO}$ . But, in general,

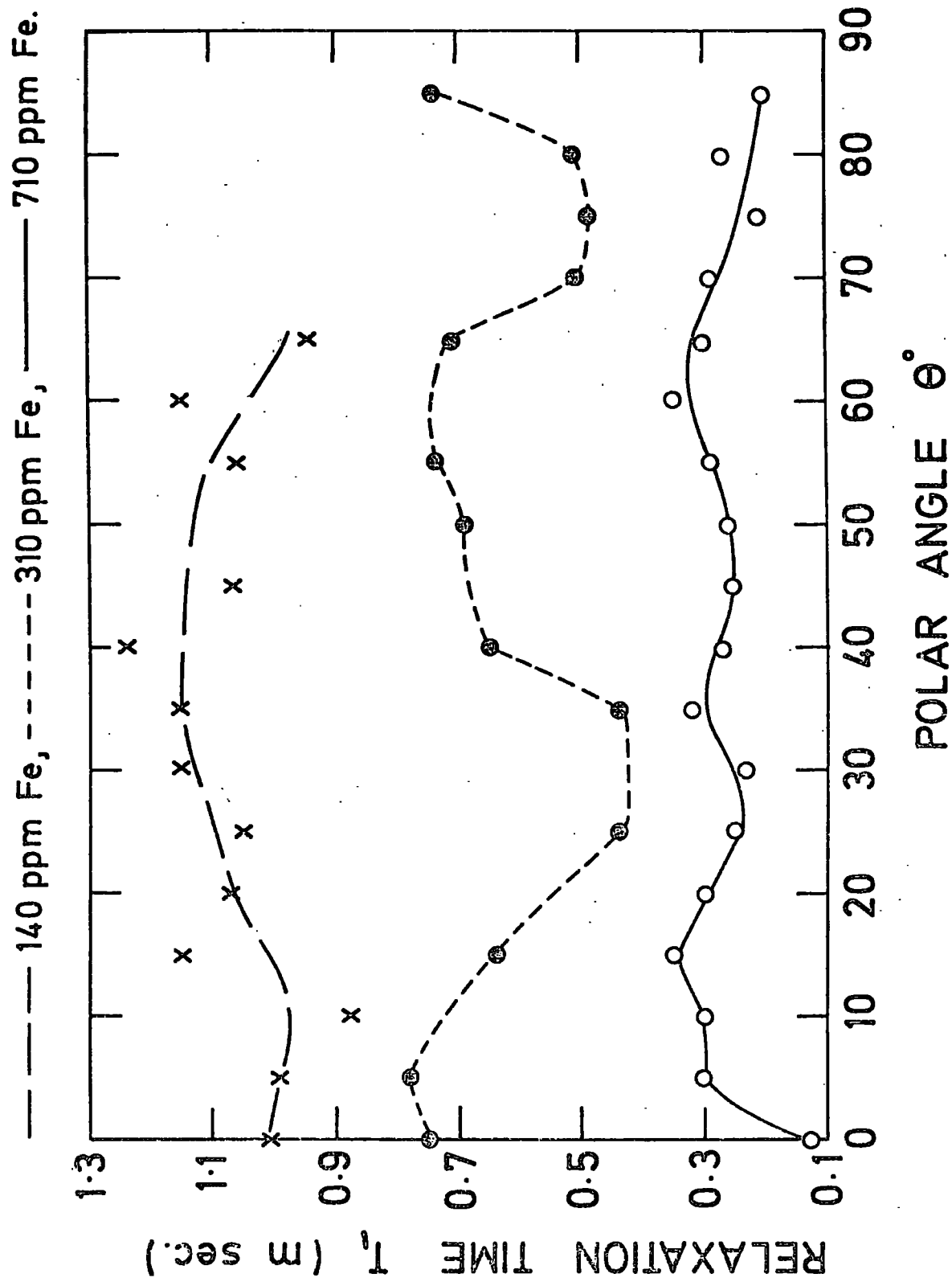


FIG. 5.3 Angular variation of  $T_1$ ;  $\text{Fe}^{3+}/\text{MgO}$ ,  $1/2 \leftrightarrow -1/2$  transition at 4.2K and 37.5 GHz.

we may conclude that the angular dependence of the relaxation time is a consequence of the variation in admixture between states as the angle  $\theta$  changes; this is in agreement with Standley and Vaughan (19).

#### 5.2.5 Frequency dependence of $T_1$

Since the measurements of  $T_1$  reported here were made at one frequency of 37.5 GHz, they provide by themselves no information on the frequency dependence of the relaxation time. However, Shiren (10) has reported computed values of  $T_1$  at 10 GHz, also, in the same publication, Castle and Feldman have published measured values for  $T_1$  at 10 GHz. On reviewing the laws of dependence of  $T_1$  on frequency  $f$ , two particular cases arise, as discussed by Thorp, Sturgess and Brown, 1972 (22), viz. (a) the behaviour of the ion represented by an isolated Kramers doublet showing a  $T_1 \propto f^{-4}$  dependence, and (b) the non-Kramers ion which gives a  $T_1 \propto f^{-2}$  dependence. Applying these two laws to our results we find that the  $T_1 \propto f^{-4}$  law is better obeyed, Table 5.3. For comparison of results we refer to Davis and Wagner, 1964 (23) who showed that potassium cobalticyanide containing  $\text{Fe}^{3+}$  obeyed equation  $T_1 = a H^{-4} T^{-1}$  very closely, displaying a  $T_1 \propto H^{-4}$  dependence (or  $T_1 \propto (\text{frequency})^{-4}$ ) for the direct process at helium temperatures from 4 GHz to 12 GHz. This, in fact, agrees with the predictions of Van Vleck, 1940 (11) for the spin-lattice relaxation time dependence on magnetic field at low temperatures in the direct region of relaxation, for an isolated Kramers doublet. Van Vleck concluded that regarding the dependence on field strength his calculations also apply to  $\text{Fe}^{3+}$  (in iron alum) as well as  $\text{Cr}^{3+}$  (in chrome alum).

#### 5.3 Conclusion

The observation of two decay rates in the recovery curves may

	(m sec)		
Castle & Feldman, $T_1$ at 10 GHz	714.3	23.8	
Shiren, $T_1$ at 10 GHz	50	26	7.6
$f^{-2}$ law for Castle & Feldman values	50.8	1.7	
$f^{-2}$ law for Shiren values	3.6	1.8	0.5
$f^{-4}$ law for Castle & Feldman values	3.6	0.1	
$f^{-4}$ law for Shiren values	0.3	0.1	0.04
Present measurements at 37.5 GHz	0.8	0.3	

Table 5.3: Application of  $f^{-2}$  and  $f^{-4}$  laws of dependence of  $T_1$  on frequency.

indicate that there is a contribution from the other energy levels of the  $\text{Fe}^{3+}$  system. However, this could not be due to a fast relaxing centre, as in the case of exchange interaction, because the two measured rates are comparable in magnitude. We may conclude that  $\text{Fe}^{3+}$  ions in MgO crystals behave as expected from the theory for an S-state ion regarding the  $T_1$ -temperature dependence, since it has shown an approximate  $T^{-5}$  dependence. With the iron concentrations available we have seen that  $T_1$  varies approximately as the inverse of the concentration; a behaviour which was reported previously for several materials. The angular variation of  $T_1$  revealed some features of cross-relaxation of certain transitions with the main transition under experiment. This manifested itself in the decrease of  $T_1$  at specific angles. Finally, comparison of our measurements of  $T_1$  at 37.5 GHz with published results at 10 GHz revealed that the dependence of  $T_1$  on frequency obeys a  $T_1 \propto (\text{frequency})^{-4}$  behaviour which is expected for Kramers' ions according to the present theories.

## CHAPTER 6

### CAVITY GROWTH IN NEUTRON IRRADIATED MAGNESIUM OXIDE.

With the knowledge acquired about the ESR behaviour of  $\text{Fe}^{3+}$  in MgO single crystals we were able to contribute to the study of cavity growth in neutron irradiated magnesium oxide. This was achieved by the investigation of the ESR spectra after annealing the samples in the temperature range from 1475 to 1775°C and a subsequent study followed (in collaboration with G J Russell) using transmission electron microscopy (TEM). Since we will be dealing with a rather new topic, we think it may be reasonable to begin with some introduction to the nucleation and growth of cavities.

#### 6.1 Introduction

The growth of cuboidal cavities is a feature of irradiation damage occurring in ionic single crystals. To nucleate these defects and to sustain their growth it is necessary to create a sufficient number of vacancies with a mobility high enough to allow agglomeration. For this to occur in magnesium oxide, Morgan and Bowen, 1967 (1) have shown that it is necessary to irradiate to a dose exceeding  $10^{20}$  nvt (in this notation  $n$  is the number of neutrons per unit volume,  $v$  the velocity of neutrons and  $t$  is the time of exposure) and subsequently to anneal in argon at a temperature greater than 1500°C for one hour. In addition to the production of vacancies, exposure to such irradiation results in the transmutation of magnesium and oxygen nuclei thereby producing mainly inert gas atoms of neon and helium, as discussed by Wilks, 1966 (2). Morgan and Bowen demonstrated that the cavities in annealed material contained these gases at low pressure.

In the case of the alkali halides it has been shown that impurity atoms often play an important role in radiation damage processes. The MgO studied by Morgan and Bowen was known to contain a relatively large impurity concentration of about 500 ppm which was chiefly Fe, Al, Ca and Si. Thus it is expected that at least some of these impurities may be involved in the cavity growth process. However, to date, no evidence for the correlation between impurity content and cavity growth has been reported and the aim of this study was to investigate if any such relationship existed. Transmission electron microscopy on its own was inadequate to identify impurities so a complementary technique was necessary. Such a technique is that of electron spin resonance which is not only capable of detecting very low levels of certain impurities, but is also useful for monitoring changes in local environments. ESR has already been used extensively in the study of neutron irradiation damage in MgO and of the effect of annealing at temperatures below that necessary to nucleated cavities, as indicated by Henderson et al, 1971 (3). Thus it was intended in this work to extend the use of this technique to the study of samples containing cavities and to correlate the results with TEM of the same samples.

## 6.2 Experimental

The single crystals of MgO used for this study were obtained from Semi-Elements Inc., Saxonburgh, Pa. Cleaved specimens having dimensions of about  $10 \times 4 \times 0.5 \text{ mm}^3$  were given a heat treatment for 18 hours at  $1300^\circ\text{C}$  in an ambient of hydrogen before being irradiated to a dose of  $3.66 \times 10^{20}$  nvt in the Harwell Dido reactor. The irradiation temperature was about  $150^\circ\text{C}$ . Post-irradiation annealing treatments, each of one hour duration, were carried out over a range of temperatures at  $50^\circ\text{C}$  intervals



between 1475 and 1775°C in an atmosphere of argon. The heating up and cooling periods were short compared with one hour annealing time; to achieve the latter, the samples were air-cooled.

ESR spectra in the region of magnetic field corresponding to the g-value of the free electron were obtained for each of the annealed samples. All measurements were made at Q-band (35 GHz) and liquid nitrogen temperature (77 K). The magnetic field direction was in a {100} plane of each specimen. Calibration of this magnetic field was made using a trace of D.P.P.H., the g-value of which was taken to be 2.0037, supplementing the electromagnet calibration obtained employing the proton/lithium resonance technique.

After examination by ESR the samples were cleaved and the flakes so produced were further reduced in thickness by chemical polishing using phosphoric acid at about 150°C (see for instance Washburn et al (4)). The thinned samples were examined in a JEM 120 electron microscope by G J Russell (5) who produced a number of micrographs recorded from different areas for each annealed specimen to determine the size distribution of the cavities. The sample orientation was close to a <100> direction in all cases.

## 6.3 Results

### 6.3.1 Transmission Electron Microscopy

Examination by TEM showed that the sample annealed at 1475°C contained interstitial dislocation loops and tangles as seen in Figure 6.1. This damage is similar to that described and discussed by Groves and Kelly, 1963 (6) and by Bowen and Clarke, 1964 (7). In all the samples annealed above 1500°C cuboidal cavities as seen in Figures 6.2a and 6.2b were present. These figures, which were recorded from the sample annealed

at 1675°C, show that the cavities range in size from about 50 to 300 Å and are bounded by {100} faces. The dislocations which were still present in those samples annealed at temperatures greater than 1500°C were often associated with cavities. This observation is in agreement with that of Morgan and Bowen (1), but we would further point out that dislocations frequently appeared to be pinned by the cavities as at A in Figure 6.2a. This pinning was such that the orientation of the dislocations close to the cavities was near to a  $\langle 110 \rangle$  direction, as at A in Figure 6.2b.

The histograms in Figure 6.3 show the size distribution of the cavities as a function of annealing temperature. They were derived from at least ten micrographs taken from different areas for each annealed sample. The main observation to be made from these size distributions is that the mean cavity size increases dramatically on annealing at a temperature exceeding some value between 1575 and 1625°C. Annealing at higher temperatures than this does not appear to produce any further increase in cavity size or significant change in the size distribution.

The total cavity volume per unit crystal volume and the concentration of cavities for each annealed sample have also been estimated and are given in Table 6.1. For the purpose of these calculations a mean specimen thickness for the total area from which the size distributions were obtained was taken to be 1000 Å, a typical sample thickness for transmission microscopy. Accepting the crudeness of this approximation, Table 6.1 shows that the large increase in cavity size which occurs at 1625°C (see Figure 6.3) is accompanied by a large increase in the ratio of the total cavity volume to crystal volume. The cavity concentration remains more or less unchanged.

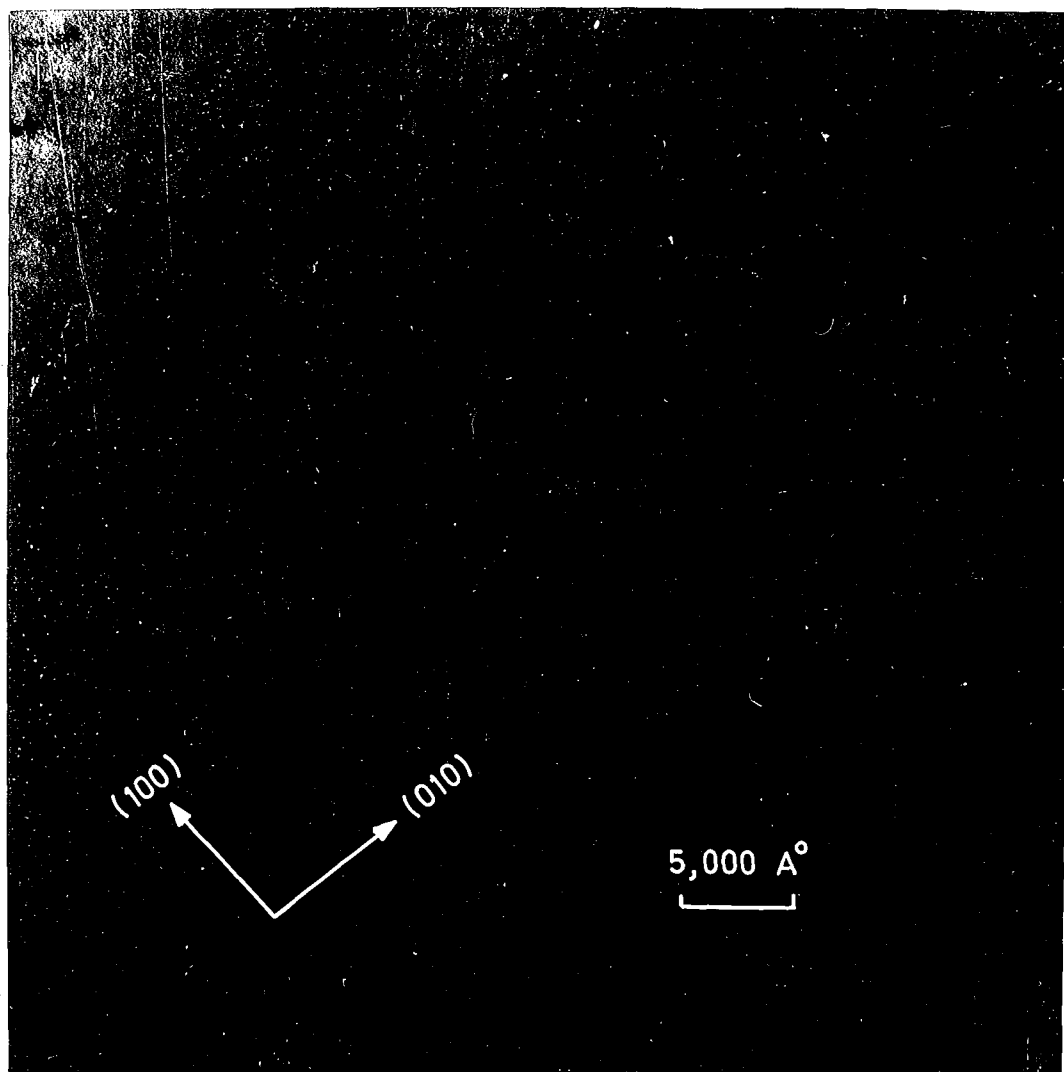
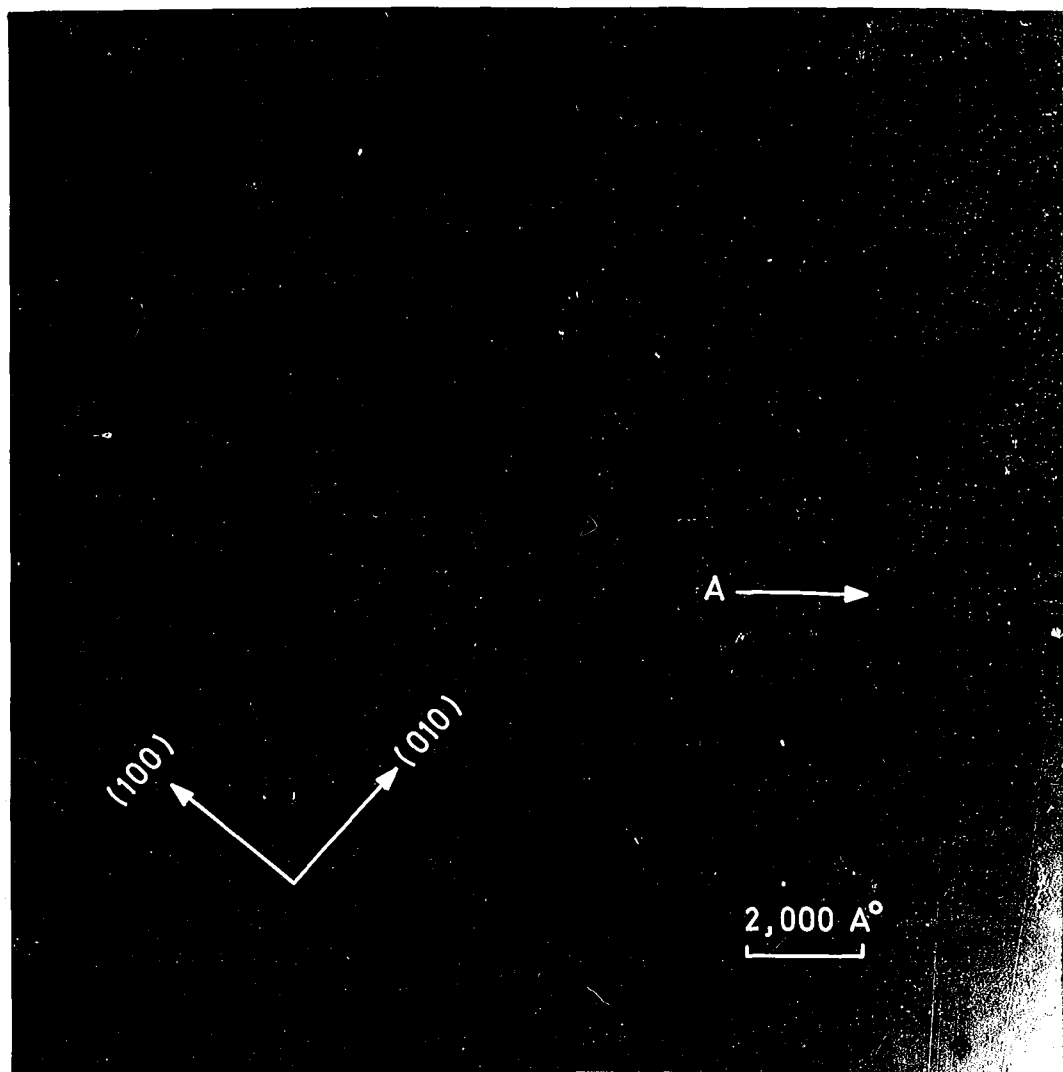


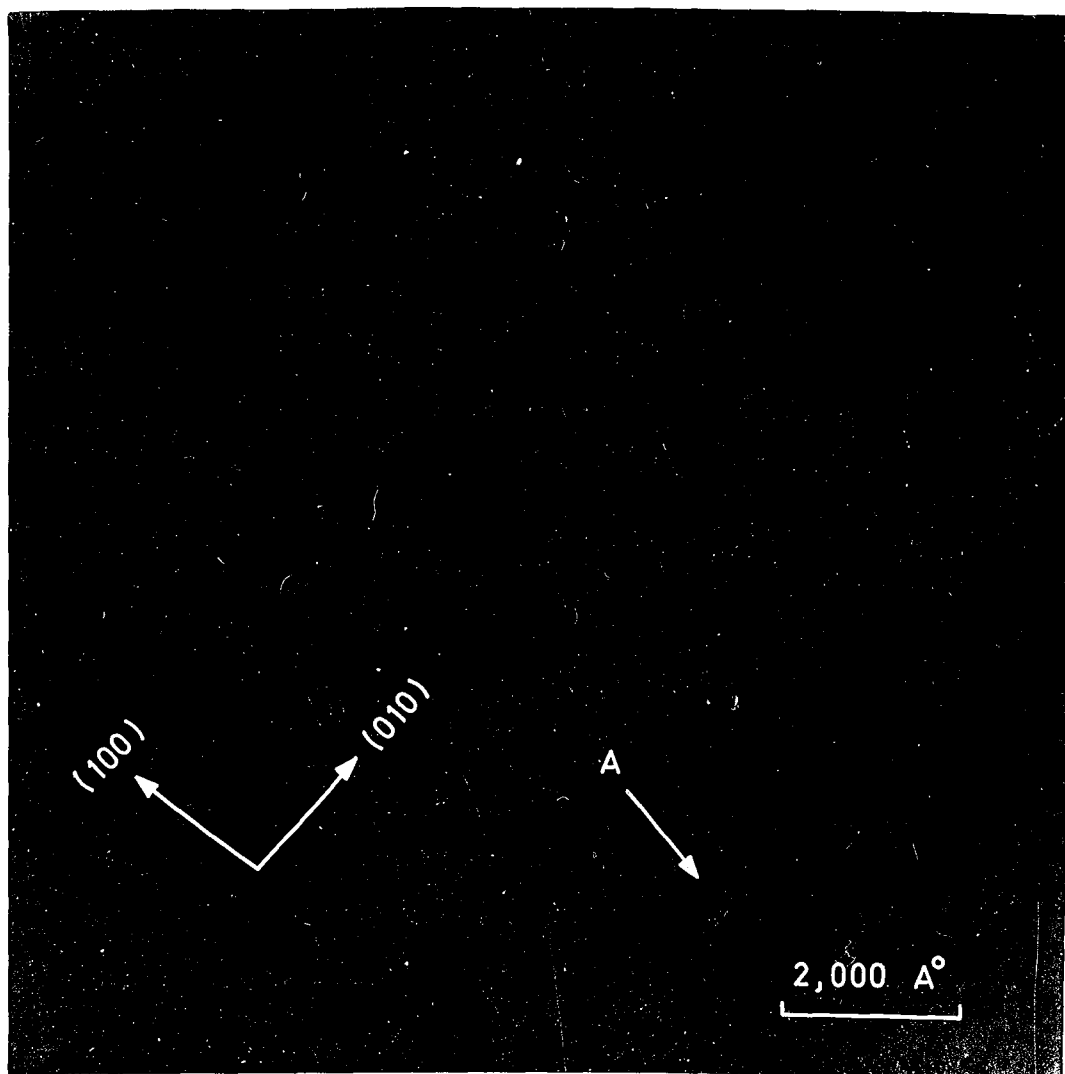
Fig. 6.1: Interstitial dislocation loops and  
tangles in the sample annealed at  
 $1475^{\circ}\text{C}$  for one hour



(a)

Fig. 6.2: The pinning of dislocations at cavities in the sample annealed at  $1675^{\circ}\text{C}$ .

In (a) both sections of the dislocation at 'A' are approximately in the plane of the foil.



(b)

Fig. 6.2: The pinning of dislocations at cavities in the sample annealed at  $1675^{\circ}\text{C}$ .  
In (b) one section of the dislocation at 'A' is almost perpendicular to the plane of the foil.

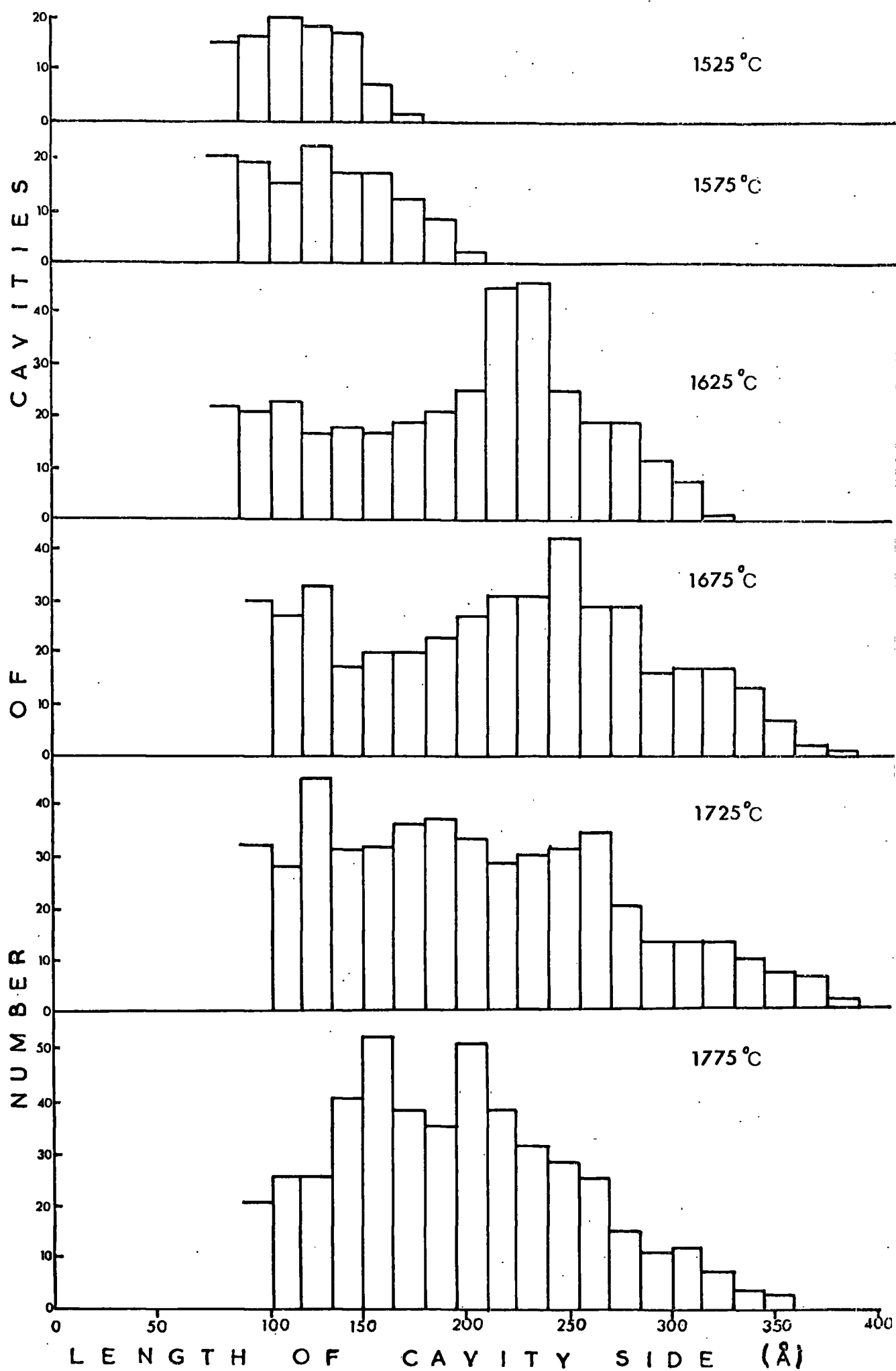


FIGURE 6.3 VARIATION OF CAVITY SIZE WITH ANNEALING TEMPERATURE

Temperature of Anneal ( $^{\circ}\text{C}$ )	Ratio of cavity volume /crystal volume ( $\times 10^4$ )	Number of cavities per cc ( $\times 10^{-14}$ )
1525	1.8	0.95
1575	1.4	0.51
1625	13.5	1.38
1675	11.2	0.83
1725	11.9	1.00
1775	16.2	1.64

Table 6.1

The variation of cavities volume and concentration  
with the annealing temperature.

### 6.3.2 Electron Spin Resonance

The main results of the ESR studies are illustrated by the spectra obtained from the specimens annealed at 1475°C, 1575°C and 1625°C respectively. Although detailed analyses of the particular specimens used were not available, data on other MgO crystals made by the same supplier (Semi-Elements Inc.) has been given by Martin, 1968 (8) whose results showed that the major paramagnetic impurity was iron at about 100 wt. ppm; it is also generally accepted from analytical evidence on other MgO crystals that both manganese and chromium are often present at low trace levels.

Figure 6.4 shows the spectrum obtained with the magnetic field parallel to  $\langle 100 \rangle$  for the specimen annealed at 1475°C which contained interstitial loops but no cavities, (c.f. Figure 6.1). The prominent features are (a) six lines marked A, (b) a line B having  $g = 1.9785$  and (c) a line C having  $g = 2.0034$ . Features A and B were identified by comparison with Henderson and Wertz's data, 1968 (9) as arising from the  $+\frac{1}{2} \rightarrow -\frac{1}{2}$  transition of  $Mn^{2+}$  and from  $Cr^{3+}$  respectively. The origin of line C is in some doubt. Further measurements showed that it was isotropic, indicating that it could not be ascribed to an interstitial atom with an associated vacancy; although the  $g$ -value is reasonably close to that of the  $+\frac{1}{2} \rightarrow -\frac{1}{2}$  transition of  $Fe^{3+}$  in octahedral symmetry, this interpretation is precluded because the  $\pm\frac{3}{2} \leftrightarrow \pm\frac{1}{2}$  transitions are absent; and finally the  $g$ -value does not fit with any of those of the impurities listed in the review by Henderson and Wertz. Evidence given later suggests that line C may arise from an electron trapped in a vacancy to form a centre persistent even at the annealing temperatures used.

In the spectra obtained from specimens annealed at both 1525°C and 1575°C, i.e. just above the temperature necessary to nucleate cavities, new features were observed. These are shown in Figure 6.5 which refers



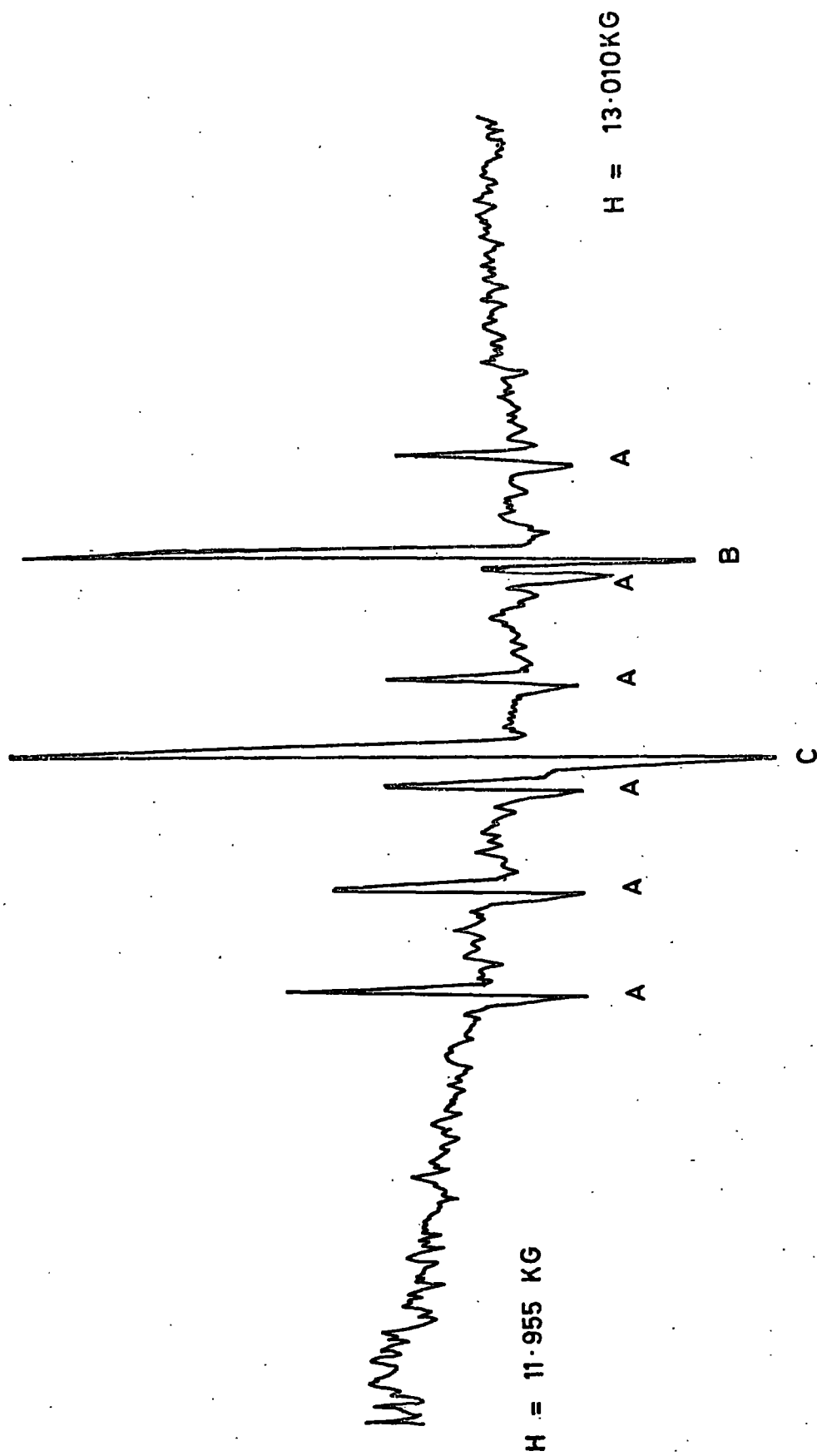


FIG 6.4 E.S.R Spectrum of the Sample Annealed at  $1475^{\circ}\text{C}$

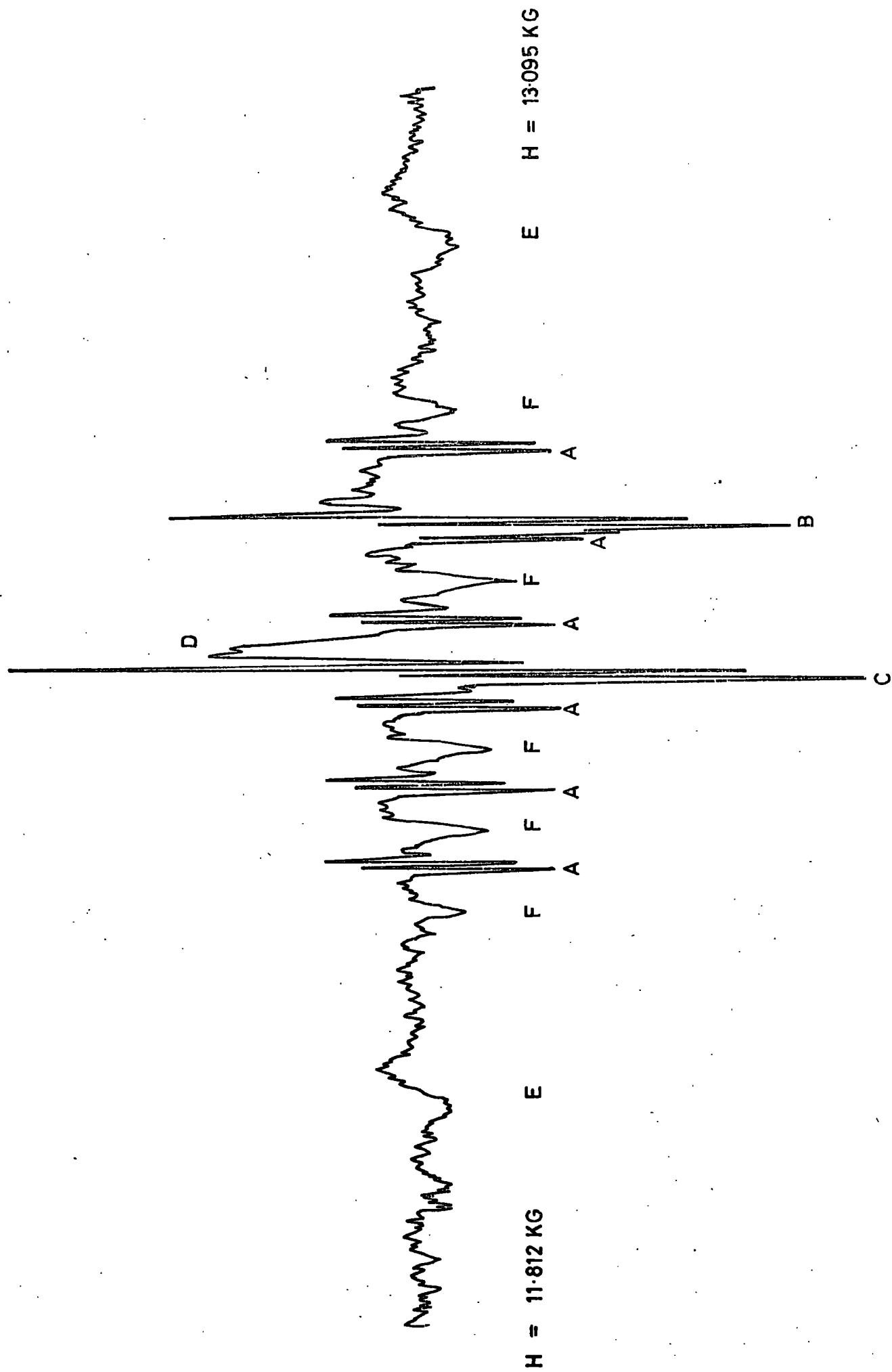


FIG 6.5 E.S.R. Spectrum of the Sample Annealed at 1575 °C

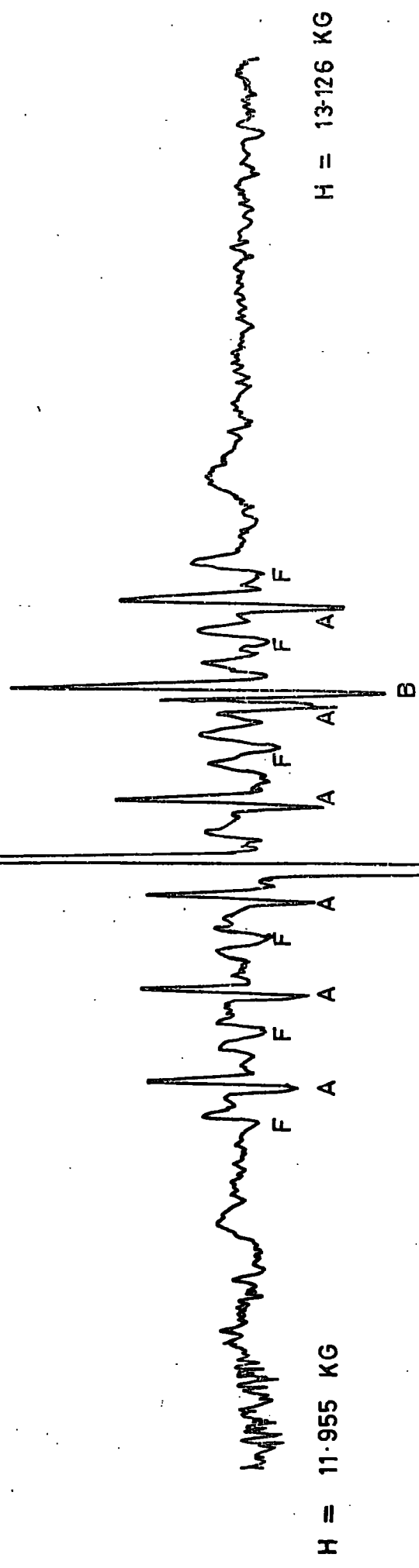


FIG 6.6 E.S.R. Spectrum of the Sample Annealed at  $1025^{\circ}\text{C}$

to a specimen annealed at 1575°C. The most important change is the occurrence of the new lines marked D and E; the g-value of 2.0031 for the D transition, together with the observed anisotropy of E lines, fit well with reported data on  $\text{Fe}^{3+}$  (9,10) and enable them to be identified as the  $-\frac{1}{2} \leftrightarrow \frac{1}{2}$  and  $\pm \frac{3}{2} \leftrightarrow \pm \frac{1}{2}$  transitions respectively of  $\text{Fe}^{3+}$  in octahedral symmetry, i.e.  $\text{Fe}^{3+}$  ions occupying magnesium sites. The other differences appear to be associated with localised detailed changes in the manganese environment; they include additional transitions close to each of the six A lines and also transitions F situated midway between the A lines. The transitions F are of low intensity and have the same separation as the A lines.

The spectra of specimens annealed above 1575°C (e.g. Figure 6.6) differ from those just described in two major respects. In the first place there is no indication of the D and E lines corresponding to  $\text{Fe}^{3+}$  in octahedral symmetry; secondly, the additional lines in Figure 6.5 which were attributed to  $\text{Mn}^{2+}$  are much less pronounced. Comparison of all the spectra shows that the intensity ratio of the  $\text{Mn}^{2+}$  hyperfine and  $\text{Cr}^{3+}$  lines remained approximately constant throughout all the annealing treatments and consequently the hyperfine components of  $\text{Mn}^{2+}$  could be used as an intensity reference, c.f. (11). On this basis it appears that in Figure 6.6 the intensity of line C has increased by approximately two times, indicating that annealing at 1625°C produces a two-fold increase in the number of centres responsible for line C.

#### 6.4 Discussion

An important conclusion of Morgan and Bowen (1) from their studies of neutron irradiated and annealed MgO was that to nucleate cavities it was necessary to anneal samples irradiated to a dose in excess of

$10^{20}$  nvt at a temperature greater than  $1500^{\circ}\text{C}$  in an ambient of argon. This minimum critical temperature was attributed to the activation energy associated with vacancy mobility. In addition, the results of the annealing studies described here concerning the nucleation and growth of cavities would suggest that another critical temperature for the growth exists in the temperature range of  $1575$  to  $1625^{\circ}\text{C}$ . While annealing above some temperatures within this range does not produce any significant change in the concentration of cavities, the ratio of total cavity volume to unit volume of crystal increases by an order of magnitude. This must similarly be accounted for by the movement of vacancies and consequently Russell et al (12) proposed that, following the nucleation of cavities, some mechanism exists which impedes further growth of these defects until another critical temperature (for an hour annealing period) is exceeded. An indication of the nature of this mechanism can be inferred from the results of our ESR measurements as will be discussed later.

One feature of cavities which was noted by Morgan and Bowen (1) was that they were often located at cusps in dislocation lines. In the present annealing studies we have found that these cusps correspond to two sections of dislocation each pinned to a corner of a cavity and lying close to a  $\langle 110 \rangle$  direction in the immediate proximity of the cavity as in Figures 6.2a and 6.2b. The association of cavities with dislocations is interpreted as follows. When an interstitial loop, which is still present in a sample at an annealing temperature greater than  $1500^{\circ}\text{C}$ , moves through the crystal it is probable that the interaction with the cavities present will result in partial annihilation of the loop by vacancies from the cavities. The movement of the parts of the loop near cavities will consequently be impeded. It is further suggested that the observed  $\langle 110 \rangle$  orientation of dislocations in the region of cavities

is related to a favourable configuration for the above annihilation process to occur. This is attributed to the fact that in the NaCl structure (which also applies to MgO), the uninterrupted rows of anions and of cations in  $\langle 110 \rangle$  directions make diffusion of vacancies of either type more likely in these directions than in others.

The ESR results show that the nucleation of cavities, in the samples annealed at  $1525^{\circ}\text{C}$  and  $1575^{\circ}\text{C}$ , is accompanied by the appearance of  $\text{Fe}^{3+}$  in octahedral symmetry. As mentioned earlier, analysis of material made by the same supplier has shown that iron was present in the specimens (8). Due to the pre-irradiation heat treatment in hydrogen it is most likely that any iron present will be in the divalent state, c.f. (13); this view is supported by the absence of  $\text{Fe}^{3+}$  lines in specimens annealed at temperatures below  $1500^{\circ}\text{C}$  (Figure 6.4).

As the post-irradiation annealing took place in an inert atmosphere the cation vacancies necessary for the conversion of  $\text{Fe}^{2+}$  into  $\text{Fe}^{3+}$  on increasing the annealing temperature from  $1475^{\circ}\text{C}$  to  $1525^{\circ}\text{C}$  must have come from within the crystal. An adequate supply of vacancies is known to be produced when the vacancy clusters, which are about  $7 \text{ \AA}$  in diameter and which are present in similarly treated specimens, suddenly collapse on annealing at about  $1500^{\circ}\text{C}$ , Martin, 1966 (14). The disappearance of the  $\text{Fe}^{3+}$  lines at temperatures above  $1625^{\circ}\text{C}$  could be explained either by a reduction of  $\text{Fe}^{3+}$  into  $\text{Fe}^{2+}$  by the outward diffusion of cation vacancies or by the trapping of vacancies near the  $\text{Fe}^{3+}$  sites, creating an  $\text{Fe}^{3+}$  vacancy complex, as reported by Henderson et al, 1971 (15), whose ESR would probably fall in the low magnetic field region outside the present range of measurement. Since the subsequent growth of the cavities indicates that a large number of vacancies are retained in the crystal the outward diffusion explanation appears unlikely and the trapping

mechanism more probable.

In view of the ESR evidence we envisage the cavity nucleation and growth proceeding by two stages as follows. On annealing just above  $1500^{\circ}\text{C}$  a critical vacancy mobility is exceeded and small cavities are nucleated in the manner described by Morgan and Bowen (1). Simultaneously there is a conversion of iron to  $\text{Fe}^{3+}$  in octahedral symmetry at magnesium sites; this conversion uses vacancies released when clusters collapse at about  $1500^{\circ}\text{C}$  which then form charge compensating centres for the  $\text{Fe}^{3+}$  ions. After nucleation negligible cavity growth occurs until an annealing temperature of  $1625^{\circ}\text{C}$  (for one hour) is reached, see Figure 6.3. This behaviour is attributed to mobile vacancies being trapped near the  $\text{Fe}^{3+}$  sites in preference to condensation at cavities. A calculation, based on the observed cavity growth between the annealing temperatures of  $1575^{\circ}\text{C}$  and  $1625^{\circ}\text{C}$  and an iron impurity level of 100 wt. ppm, shows that the number of vacancies required to associate with all the  $\text{Fe}^{3+}$  is some two orders of magnitude less than the number required to account for the cavity growth. When this stage is completed, cavity growth can proceed. It is suggested that the presence of iron is not expected to alter the magnitude of ultimate growth significantly. However, the extent to which growth is impeded, and hence the annealing temperature necessary for the last growth stage, would be expected to increase with iron concentration. Further evidence which indicates that cavity growth is incomplete when annealing at  $1500^{\circ}\text{C}$  is provided by the measurements of Bowen (16), who recorded the density variation with annealing temperature for similarly treated  $\text{MgO}$ . His results suggest that cavity formation is a two stage process, as our studies using different techniques (TEM and ESR) have confirmed to be the case. In addition, the high precision X-ray measurements of Briggs and Bowen,

1968 (17) showed that complete recovery of the lattice parameter to the unirradiated value did not occur until the annealing temperature reached about 1750°C. However, interpolation of their data would suggest that most of the recovery had occurred at about 1650°C. So, allowing for the fact that their material was irradiated to more than twice the dose of that used in this study, it is concluded that there is a reasonable correlation between the minimum temperature at which we have found it necessary to anneal to produce most of the cavity growth and that reported by Friggs and Bowen to obtain almost complete recovery of the lattice parameter. To our knowledge this influence of an impurity on the movement of vacancies and cavity growth has not previously been reported. Here it appears that iron plays a significant role. It is possible that other impurities may act in a similar way, but this remains to be established.



REFERENCES - CHAPTER 1

1. C F Hempstead and K D Bowers (1959) Phys. Rev. 118 131
2. H E D Scovil, G Feher and H Seidel (1957) Phys. Rev. Lett.  
105 762
3. L F Johnson, G D Boyd, K Nassau and R R Soden (1962)  
Phys. Rev. 126 1406
4. J M Farley (1973) Ph.D. Thesis University of Durham
5. H P Buckley (1973) Ph.D. Thesis University of Durham
6. G Brown, C J Kirkby and J S Thorp (1974) J. Mat. Sci.  
9 65
7. J S Thorp, G Brown and H P Buckley (1974) J. Mat. Sci.  
9 1337
8. J S Thorp, H P Buckley and G Brown (1974) J. Mat. Sci.  
Lett. 9 864
9. A V Komandin, R D Shapovalova and N P Mikhailova (1960)  
Russian J. Phys. Chem. 34 979
10. W S Brower and P H Fang (1969) J. Appl. Phys. 40 4988
11. R A Vasquez (1975) M.Sc. Thesis University of Durham
12. J S Thorp, R A Vasquez, C Adcock and W Hutton (1976)  
J. Mat. Sci. 11 89
13. G J Russell, E A E Ammar and J S Thorp (1976) (to be  
published)
14. I Waller (1932) Z. Phys. 79 370
15. N Bloembergen, S Shapiro, P S Pershan and J O Artman (1959)  
Phys. Rev. 114 445
16. W J C Grant (1964) Phys. Rev. 134 A1554
17. K J Standley and R A Vaughan (1969) 'Electron spin  
relaxation phenomena in solids' Adam Hilger Ltd. London

Chapter 1 (Continued)

18. P S Pershan (1960) Phys. Rev. 117 109
19. W B Mims and J D McGee (1960) Phys. Rev. 119 1233
20. U Kh Kopvillem (1961) Sov. Phys. Solid State 3 865
21. A H Eschenfelder and R T Weidner (1953) Phys. Rev. 92 869
22. S Feng and N Bloembergen (1963) Phys. Rev. 130 531
23. C F Davis, N W P Strandberg and R L Kyhl (1958) Phys.  
Rev. 111 1268
24. J G Castle, P F Chester and P E Wagner (1960) Phys. Rev.  
119 953
25. G Brown and J S Thorp (1967) Brit. J. Appl. Phys. 18 1
26. J Herve and J Pescia (1960) C. R. Acad. Sci. 251 665
27. W I Dobrov and M E Browne (1963) 'Paramagnetic Resonance'  
(Academic Press) 2 447
28. C J Gorter (1947) 'Paramagnetic resonance' Elsevier  
Pub. Co.
29. A H Cooke (1950) Rep. Prog. Phys. 13 276
30. K D Bowers and W B Mims (1959) Phys. Rev. 115 285
31. J E Pace, D F Sampson and J S Thorp (1960) Proc. Phys. Soc.  
76 697
32. A E Siegman (1964) 'Microwave solid-state masers' McGraw-Hill Co.  
New York
33. C J Kirkby (1967) Ph.D. Thesis University of Durham
34. G Brown (1967) Ph.D. Thesis University of Durham
35. C G Montgomery (1948) 'Technique of microwave measurements'  
McGraw-Hill New York

REFERENCES - CHAPTER 2

1. A V Komandin, R D Shapovalova and N P Mikhailova (1960)  
Russian J. Phys. Chem. 34 979
2. W S Brower and P H Fang (1969) J. Appl. Phys. 40 4988  
ibid. (1967) 38 2391
3. A Zalkin and D H Templeton (1964) J. Chem. Phys. 40 501
4. J Czochralski (1918) Z. Phys. Chem. 92 219
5. Marconi Instruments Ltd. Handbook No. OM 1245 (1960)
6. A H Scott and H L Curtis (1939) J. Res. Nat. Bur. Stand. 22 747
7. G Brown, C J Kirkby and J S Thorp (1974) J. Mat. Sci. 9 65
8. J S Thorp, H P Buckley and G Brown (1974) ibid. 9 864

REFERENCES - CHAPTER 3

1. R W G Wyckoff 'Crystal Structures' (Interscience New York 1948)
2. C F Hempstead and K D Bowers (1960) Phys. Rev. 118 131
3. A Arbel and R J Stokes (1965) J. Appl. Phys. 36 1460
4. A Zalkin and D H Templeton (1964) J. Chem. Phys. 40 501
5. H P Buckley (1973) Ph.D. Thesis University of Durham
6. J M Farley (1973) Ph.D. Thesis University of Durham
7. J Czochralski (1918) Z. Phys. Chem. 92 219
8. K Nassau and A M Broyer (1962) J. Appl. Phys. 33 3064
9. R W Kedzie and M Kestigian (1963) Appl. Phys. Letters 3 86
10. B Bleaney and K W H Stevens (1953) Rep. Prog. Phys. 16 108
11. V M Vinokurov and V G Stepanov (1967) Sov. Phys. Sol. State  
9 844
12. I N Kurkin and L Ya Shekun (1965) Sov. Phys. Sol. State 6 1560
13. J H Van Vleck and W G Penney (1934) Phil. Mag. 17 961
14. A Abragam and M H L Pryce (1951) Proc. Roy. Soc. A205 135
15. J S M Harvey and H Kiefte (1971) Canad. J. Phys. 49 995
16. V F Dernov-Pegarev, M M Zaripov, M I Samoilovich and V G Stepanov  
(1966) Sov. Phys. Sol. State 8 197
17. J S Thorp, G Brown and H P Buckley (1974) J. Mat. Sci. 9 1337
18. M L Randolph (1960) Rev. Sci. Inst. 31 949
19. R Yu Abdulsabirov, A A Antipin, I N Kurkin, E A Tsvetkov,  
Yu K Chirkin and V I Shlenkin (1972) Sov. Phys. Sol. State  
14 255
20. W B Mims and R Gillen (1967) J. Chem. Phys. 47 3518

Chapter 3 (Continued)

21. V Volterra, J Bronstein and M Rockni (1966) Appl. Phys. Letters  
8 212
22. C G B Garrett and F R Merritt (1964) Appl. Phys. Letters 4 31
23. U Ranon and V Volterra (1964) Phys. Rev. 134 A1483
24. P A Forrester and C F Hempstead (1962) Phys. Rev. 126 923
25. J M Farley, G A Saunders and D Y Chung (1975) J. Phys. C:  
Sol. St. Phys. 8 780
26. J S Thorp, H P Buckley and G Brown (1974) J. Mat. Sci. Letters  
9 864

REFERENCES - CHAPTER 4

1. I Waller (1932) Z. Phys. 79 370
2. C J Gorter (1936) Physica 3 503
3. R de L Kronig (1939) Physica 6 33
4. J H Van Vleck (1939) J. Chem. Phys. 7 72
5. J H Van Vleck (1940) Phys. Rev. 57 426; erratum ibid (1940) 1052
6. D H Paxman (1961) Proc. Phys. Soc. London 78 180
7. G M Zverev (1961) Sov. Phys. JETP 13 1175
8. R Orbach (1961) Proc. Roy. Soc. 264A 458
9. C P B Finn, R Orbach and W P Wolf (1961) Proc. Phys. Soc. London 77 261
10. A A Manenkov, and A M Prokhorov (1962) Sov. Phys. JETP 15 951
11. Chao-Yuan Huang (1965) Phys. Rev. 139 A241
12. R Orbach and M Blume (1962) Phys. Rev. Letters 8 478
13. M Blume and R Orbach (1962) Phys. Rev. 127 1587
14. A M Leushin (1963) Sov. Phys. Sol. St. 5 440
15. A Abragam and B Bleaney (1970) 'Electron paramagnetic resonance of transition ions' Clarendon Press Oxford
16. C P Poole and H A Farach (1971) 'Relaxation in magnetic resonance' Academic Press New York
17. K J Standley and R A Vaughan (1969) 'Electron spin relaxation phenomena in solids' Hilger London
18. R Orbach (1961) Proc. Roy. Soc. 264A 485
19. M B Walker (1968) Can. J. Phys. 46 1347
20. J C Gill (1975) Rep. Prog. Phys. 38 91
21. B I Kochelaev (1960) Sov. Phys. Doklady 5 349

Chapter 4 (Continued)

22. P G Klemens (1962) Phys. Rev. 125 1795
23. J G Castle Jr., D W Feldman, P G Klemens and R A Weeks (1963)  
Phys. Rev. 130 577
24. E W Montrell and R B Potts (1955) Phys. Rev. 100 525
25. W M Rogers and R L Powell (1958) Tables of Transport Integrals,  
National Bureau of Standards, Circular No.535 (U.S. Government  
Printing Office Washington D.C.)
26. R Mattuck and M W P Strandberg (1960) Phys. Rev. 119 1204
27. J S Thorp, H P Buckley and G Brown (1974) J. Mat. Sci. Letters  
9 864
28. D H Parkinson and J E Quarrington (1954) Brit. J. Appl. Phys.  
5 219
29. D R Mason (1966) Ph.D. Thesis University of Durham
30. R W Bierig, M J Weber and S I Warshaw (1964) Phys. Rev. 134  
A1504
31. J B Horak and A W Nolle (1967) Phys. Rev. 153 372
32. J M Farley (1973) Ph.D. Thesis University of Durham
33. G H Dieke (1969) 'Spectra and energy levels of rare earth ions  
in crystals' Wiley New York
34. P L Scott and C D Jefferies (1962) Phys. Rev. 127 32
35. D R Mason and J S Thorp (1967) Phys. Rev. 157 191
36. K Nassau (1963) J. Phys. Chem. Sol. 24 1511
37. J M Farley, G A Saunders and C Y Chung (1975) J. Phys. C :  
Sol. St. Phys. 8 780

REFERENCES - CHAPTER 5

1. J C Cheng and J C Kemp (1971) Phys. Rev. B4 2841
2. J F Cornwell (1969) 'Group theory and electronic energy bands in solids' North-Holland
3. A Kelly and G W Groves (1970) 'Crystallography and crystal defects' Longman Group Ltd. London
4. R W G Wyckoff (1965) 'Crystal structures' Vol.I Interscience New York
5. J S Thorp, R A Vasquez, C Adcock and W Hutton (1976) J. Mat. Sci. 11 89
6. J E Wertz and P Auzins (1957) Phys. Rev. 106 484
7. J S Prener (1953) J. Chem. Phys. 21 160
8. A A Manenkov and A M Prokhorov (1962) Sov. Phys. JETP 15 54
9. N S Shiren (1962) Proc. XI Colloque Ampere pp.114
10. N S Shiren (1962) Bull. Am. Phys. Soc. 7 29
11. J H Van Vleck (1940) Phys. Rev. 57 426
12. R D Mattuck and M W P Strandberg (1960) Phys. Rev. 119 1204
13. E R Andrew and D P Tunstall (1961) Proc. Phys. Soc. 78 1
14. American Institute of Physics Handbook, 3rd ed. (1972) McGraw-Hill New York
15. T H K Barron, W T Berg and J A Morrison (1959) Proc. Roy. Soc. London Ser.A 250 70
16. J H Pace, D F Sampson and J S Thorp (1961) Proc. Phys. Soc. 77 257
17. N E Kask, L S Kornienko and A I Smirnov (1963) Sov. Phys. Sol. St. 5 1212
18. J H Van Vleck (1960) Quantum Electronics (Columbia University Press New York) p.392



Chapter 5 (Continued)

19. K J Standley and R A Vaughan (1965) Phys. Rev. 139 A1275
20. P R Solomon (1966) Phys. Rev. 152 452
21. P L Donoho (1964) Phys. Rev. 133 A1080
22. J S Thorp, G L Sturgess and G Brown (1972) J. Mat. Sci. 7 215
23. D A Davis and P E Wagner (1964) Phys. Rev. Lett. 12 141

REFERENCES - CHAPTER 6

1. C S Morgan and D H Bowen (1967) Phil. Mag. 16 165
2. R S Wilks (1966) J. Nucl. Mater. 19 351
3. B Henderson, D H Bowen, A Briggs and R D King (1971) J. Phys.  
C: Sol. St. Phys. 4 1496
4. J Washburn, G W Groves, A Kelly and G K Williamson (1960)  
Phil. Mag. 5 991
5. G J Russell (1976) Ph.D. Thesis University of Durham
6. G W Groves and A Kelly (1963) Phil. Mag. 8 1437
7. D H Bowen and F J P Clarke (1964) Phil. Mag. 9 413
8. D G Martin (1968) J. Phys. C: Sol. St. Phys. 1 333
9. B Henderson and J E Wertz (1968) Adv. Phys. 17 749
10. J S Thorp, R A Vasquez, C Adcock and W Hutton (1976)  
J. Mat. Sci. 11 89
11. R D King and B Henderson (1967) Proc. of Brit. Ceramic Soc.  
9 63
12. G J Russell, E A E Ammar and J S Thorp (1976) (to be published)
13. R W Davidge (1967) J. Mat. Sci. 2 339
14. D G Martin (1966) A E R E Rep. No. R5269 243
15. B Henderson, J E Wertz, T P P Hall and R D Dowsing (1971)  
J. Phys. C: Sol. St. Phys. 4 107
16. D H Bowen (1966) A E R E Rep. No. R5269 461
17. A Briggs and D H Bowen (1968) Mass Transport in Oxides,  
Nat. Bur. Stand. Special Pub. (Washington U S Govt. Printing  
Office) 296 103

APPENDIX

PUBLICATIONS

1. 'The dielectric constants of  $\text{CaWO}_4$ ,  $\text{Nd/CaWO}_4$  and  $\text{Gd/CaWO}_4$ '  
J S Thorp and E A E Ammar (1975) J. Mat. Sci. 10 918
2. 'Spin-lattice relaxation in gadolinium-doped calcium tungstate'  
J S Thorp and E A E Ammar (1976) J. Mat. Sci. 11 1215
3. 'Cavity growth in neutron-irradiated magnesium oxide'  
G J Russell, E A E Ammar and J S Thorp (1976)  
J. Mat. Sci. (to be published)
4. 'Q-band ESR spectra of gamma-irradiated Pyrex' G Brown,  
E A E Ammar and J S Thorp (1976) J. Mat. Sci.  
(to be published)

